STARS

Electronic Theses and Dissertations, 2004-2019

2007

Understanding The Low Temperature Electrical Propertiesof Nanocrystalline Sno2 For Gas Sensor Applications

Christina Drake
University of Central Florida

Showcase of Text, Archives, Research & Scholarship

UNDERSTANDING THE LOW TEMPERATURE ELECTRICAL PROPERTIES
OF NANOCRYSTALLINE SnO$_2$ FOR GAS SENSOR APPLICATIONS

by

CHRISTINA HARTSELL DRAKE
B. S. University of Florida, 2003

A dissertation submitted in partial fulfillment of the requirements
for the degree of Doctor of Philosophy in Materials Science and Engineering
in the Department of Mechanical, Materials, and Aerospace Engineering
in the College of Engineering and Computer Science
at the University of Central Florida
Orlando, Florida

Spring Term
2007

Major Professor: Sudipta Seal

ABSTRACT

Nanocrystalline metal/metal oxide is an important class of transparent and electronic materials due to its potential use in many applications, including gas sensors. At the nanoscale, many of the phenomena observed that give nanocrystalline semiconducting oxide enhanced performance as a gas sensor material over other conventional engineering materials is still poorly understood. This study is aimed at understanding the low temperature electrical and chemical properties of nanocrystalline SnO_2 that makes it suitable for room temperature gas detectors. Studies were carried out in order to understand how various synthesis methods affect the surfaces on the nano-oxides, interactions of a target gas (in this study hydrogen) with different surface species, and changes in the electrical properties as a function of dopants and grain size.

A correlation between the surface reactions and the electrical response of doped nanocrystalline metal-oxide-semiconductors exposed to a reducing gas is established using Fourier Transform Infrared (FTIR) Spectroscopy attached to a specially built custom designed catalytic cell. First principle calculations of oxygen vacancy concentrations from absorbance spectra are presented. FTIR is used for effectively screening of these nanostructures for gas sensing applications. The effect of processing temperature on the microstructural evolution and on the electronic properties of nanocrystalline trivalent doped–SnO_2 is also presented. This study includes the effect of dopants (In and Ce) on the growth of nano-SnO_2, as well as their effects on the electronic properties and gas sensor behavior of the nanomaterial at room temperature.

Band bending affects are also investigated for this system and are related to enhanced low temperature gas sensing. The role and importance of oxygen vacancies in the electronic and chemical behavior of surface modified nanocrystalline SnO_2 are explored in this study.

A generalized explanation for the low temperature gas sensor behavior of nanocrystalline oxide is presented that can be generalized to other nano-oxide systems and be useful in specific engineering of other nanomaterials. Deeper understanding of how nano-oxides react chemically and electronically would be extremely beneficial to issues present in current low cost, low temperature sensor technology. Ability to exactly monitor and then engineer the chemistry of nanostructures in the space charge region as well as the surface is also of great significance. Knowledge of the mechanisms responsible for enhanced sensor response in this material system could viably be applied to other material systems for sensor applications.

This is dedicated to my husband, whose faith in God
and constant support has been monumental in my life.

TABLE OF CONTENTS

LIST OF FIGURES

LIST OF TABLES

LIST OF ACRONYMS

<u>DR-FTIR</u>: Diffuse Reflectance Fourier Transform Infrared Spectroscopy

<u>FTIR</u>: Fourier Transform Infrared Spectroscopy

<u>HRTEM</u>: High Resolution Transmission Electron Spectroscopy

<u>PTFE</u>: Polytetraflouroethylene

<u>SAED</u>: Selected Area Electron Diffraction

<u>UV-vis</u>: Ultraviolet-visible Spectroscopy

<u>XPS</u>: X-ray Photoelectron Spectroscopy

<u>XRD</u>: X-ray Diffraction

CHAPTER ONE: INTRODUCTION

1.1 Motivation

Gas sensors play an important part of many different types of applications around the world. The ultimate goal of any gas sensor device is to be able to detect a target gas accurately in the presence of other gases. This includes detection at even very low concentrations, and also as soon as the target gas is actually present. Gas sensors are commonly used in industrial applications where many gas storage containers are in use or where synthesis may involve the evolution of gas. In many industrial applications, gas sensors are used to help determine gas leaks in order to prevent any harm to human health as well as to protect from any explosions that such leaks may cause.

Hydrogen as a source of fuel has become increasingly desirable in recent years. Depletion of fossil fuels coupled with environmental concerns has lead to an increase in research for alternative energy sources. Using hydrogen as a fuel source would mean only water as a by product and better conversion of the fuel to energy. With regards to the space program, hydrogen fuel is the best option, at present, for fueling the launch of their space vehicles. Hydrogen fuel is lightweight and also avoids polluting emissions. A major issue concerning the use of hydrogen is its volatile nature. In the presence of oxygen with a 2-3 volume % leak, this gas is highly explosive, making safety a major concern. The major mode for transporting hydrogen gas to the launch pad in the space

program is through pipelines. Due to the very small size of the hydrogen molecules, pipeline leaks are always a concern.

In 1999, Cable News Network (CNN) reported that the space-shuttle Columbia was leaking hydrogen from one of the shuttle's main engines during its climb to orbit. While the shuttle still made it into orbit, the leak could have caused an early engine shutdown [1]. This raises concerns, especially when one considers that the 1986 Challenger explosion may have been linked to hydrogen leaks. Another incident, with a hydrogen leak again being the culprit, was the cancellation of the Atlantis launch in 2002. This leak was brought to light by an observer assigned to watch the launch pad from afar using video cameras [2]. Human error could have possibly missed this leak. This is one reason a low temperature hydrogen sensor is attractive and necessary in order to increase safety with the use of hydrogen fuel. If a low temperature, highly sensitive hydrogen gas sensor existed which could be packaged into a small device, several of these sensors could be placed in different areas of concern; wherever gas leaks are a possibility. This would bring about the widespread use of hydrogen as a fuel more rapidly beyond even just the space program.

Currently, many gas sensors that are available leave much to be desired. Some of the current gas sensor issues are selectivity to the target gas, use of the sensor at lower operating temperatures, the response time to the target gas, and recovery time of the sensor material after removal of the target gas. In a recent survey of literature, most of the hydrogen sensors based on SnO_2 operated at higher temperatures, with the highest

sensitivities achieved at 250°C, Figure 1. [3] This indicates that for maximum sensitivity to hydrogen gas to occur, a gas sensor device would require a source of power in order to maintain this operating temperature. Widespread use of gas sensors becomes more attractive when smaller packaging can be achieved, a possibility with a low temperature gas sensor not requiring additional power.
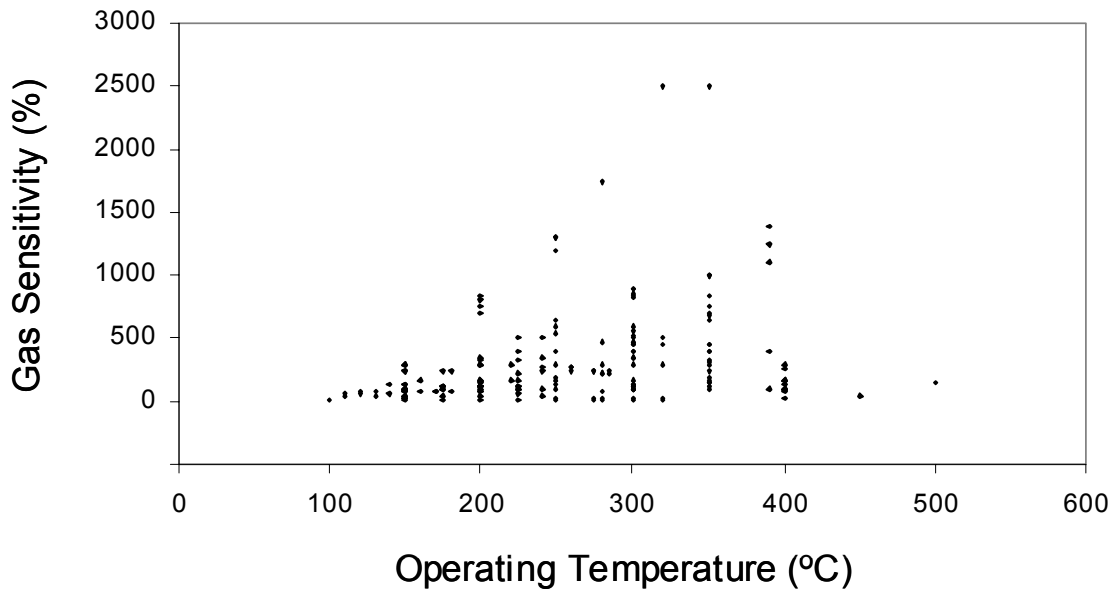
Figure 1: *Variation in the gas sensitivity of sol-gel derived nanocrystalline SnO$_2$ thin film as a function of operating temperature [3]*

1.2 Nanotechnology's role in gas sensor development

Use of nanotechnology in engineering materials for sensor applications may improve the working detection limit of gas sensors to lower temperatures. This will be achieved predominantly by alterations of the space charge layers for each grain and enhancing other electronic properties of the material. The large surface to volume ratio of nanomaterials can be used as an advantage to aid in gas sensor development. The surface reaction which identifies hydrogen on the gas sensor is improved when the number of defect sites for reaction is increased. The large surface area to volume ratio of nanocrystalline structures increases the opportunity for this surface reaction to occur [4]. This in turn will increase the sensitivity of the gas sensor. Engineering materials with select chemistry to modify and manipulate the structure is the key to the improvement in gas sensor sensitivity and selectivity.

Nanomaterials have been spotlighted for gas sensor applications due to their enhanced abilities over their conventional engineering material counterparts. The surface of nanomaterials can comprise much of the actual material making them ideal for gas sensors. [5] Ability to synthesize one dimensional nanostructures with extremely high aspect ratios makes them attractive in gas sensor fabrication as well. The space charge layer control of nanostructures makes them particularly interesting since conduction can change drastically with expansion and contraction of the layer in the presence of different gases. [6, 7] Another interesting aspect of nanomaterials that make them a

candidate for room temperature gas sensing is the fact that changes in the band gap have been reported at extremely small sizes. [8] In spite of these observations at the nano-scale, many of the mechanisms responsible for conduction at the nano-scale are still poorly understood.

Room temperature gas sensing may be achieved by modifying several different material parameters with modifications available when dealing with materials at the nanoscale. First, achieving a high non-equilibrium amount of oxygen vacancies in the oxide sensor material will help in achieving this goal. A high non-equilibrium amount of oxygen vacancies would serve to aid in more effective movement of charge across the sensor material. The term non-equilibrium is used here because thermodynamics at room temperature does not predict the amount of vacancies required for this at low operating temperatures. The oxygen vacancies also need to not be "pinned" to any impurities and also need as little resistance as possible at the grain boundaries when the appropriate reducing gas is present. Second, increasing the number of surface sites for gas interaction will help in achieving this goal; so that even low concentrations of gas can be detected at room temperature. Use of nanomaterials is significant for this due to their high surface to volume ratio. This can be increased by changing the shape of the nanoparticle from spherical to one dimensional, by creating rods or hollow tubes [9]. The third change that can be made to the sensor material is modification of the space charge layer. This is done in order to get the maximum signal change in the presence of the target gas. Modification of the space charge layer can be done by 1) reducing the crystallite size, 2) changing the defect chemistry within the space charge layer and

surface of the material, and 3) changes in particle shape may play a factor. Another interesting aspect of nanomaterials that make them a candidate for room temperature gas sensor applications is the fact that changes in the band gap have been reported at extremely small sizes. [8] The possibility to modify this band gap may be another way to improve room temperature gas sensing by changing the potential barrier energy required for charged species to conduct.

Another enhanced feature of nanocrystallites is their conduction of electrons from the surface reaction. These conduction electrons have to overcome a potential barrier induced by the space charge layer. The magnitude of this space charge layer is dependant on the crystallite size (D) as well as the space-charge layer thickness (L), and is discussed in further detail in a later section. It has been shown that when D < 2L, the sensitivity of a gas sensor is enhanced drastically [10]. This D < 2L limit can be reached when employing nanostructures.

CHAPTER TWO: NANOCRYSTALLINE In-SnO$_2$

2.1 Nanocrystalline SnO$_2$

SnO$_2$ is a transparent, wide band gap semiconductor with its band gap typically reported at 3.6 eV or higher at 300K. [11-16] SnO$_2$ is a material of great interest due to the ability to tailor its electrical and microstructural properties, making it useful in applications such as varistors, catalysts, thick film resistors, and electrochemical devices such as gas sensors. [17-20] Much of the ability to tailor SnO$_2$'s properties comes from the multi-valence ability of the tin atom which allows for changes in the chemical behavior. These changes in the chemical behavior of SnO$_2$ can help tune this material to specific applications.

The rutile crystal structure of SnO$_2$, Cassiterite, has a tetragonal unit cell with a space-group symmetry of P42/mnm. The lattice constants for Cassiterite are a = b = 4.731 A $^\circ$ and c = 3.189 A$^\circ$. In the SnO$_2$ matrix, tin atoms are sixfold coordinated to threefold coordinated oxygen atoms. A representation of the unit cell can also be found in Figure 2. The Cassiterite form of SnO$_2$ is the most useful form of the material due to its enhanced electronic and chemical properties, though other structures of SnO$_2$ do exist.
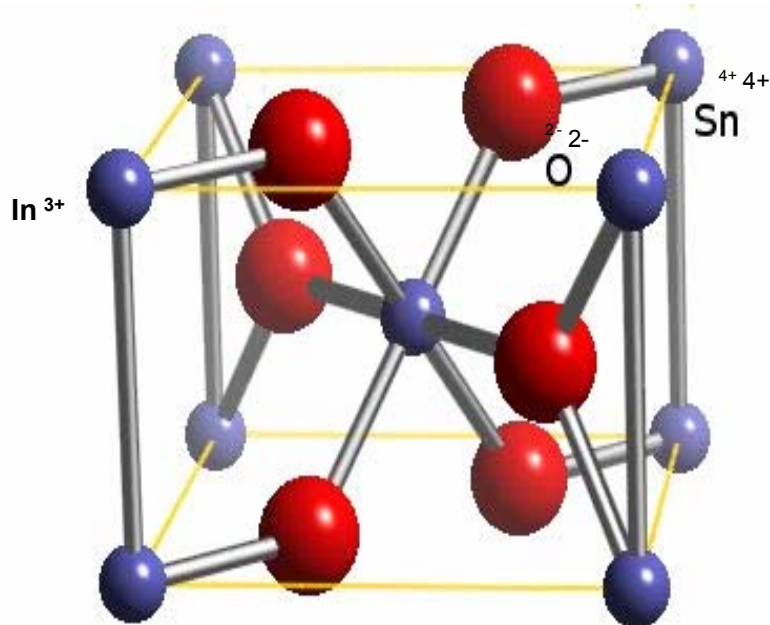
Figure 2: *SnO₂ Cassiterite Structure*

Perhaps one of the most useful aspects of SnO_2 in many of its applications are the changes that can occur in its surface composition, from stoichiometric surfaces with Sn^{+4} to reduced surfaces with Sn^{+2}. Changes to a reduced surface structure have a dramatic effect on the surface electronic structure of the material. Reduction of the surface will lead to formation of Sn 5s derived surface states that lie deep within the band gap and also cause a lowering of the work function. [21] This is one reason SnO_2 is an excellent candidate for gas sensor applications.

Another interesting aspect of the SnO$_2$ surface is with respect to the oxygen atoms that reside there. One theoretical study has shown that energetically favorable reconstructions of the SnO$_2$ (110) and (101) surfaces result in surface oxygen deficiency. [22-24] This in itself is interesting since many times the surface of a material will act as a sink for vacancies. Reconstruction of the SnO$_2$ surface is possible and gives rise to a host of different surface situations available to this one material system. This is another reason why SnO$_2$ is widely considered and desirable for gas sensor applications.

2.2 Electronic Behavior at the Nanoscale

In most traditional semiconductors, the degree of electrical conduction is similar to the material's degree of thermal conductivity. Typically, a semiconductor's electrical conductivity is determined by the number of charge carriers, the charge carried by the charge carriers, and the ability of the charge carriers to move. As the temperature is increased, it becomes easier for semiconductors to conduct or move charges. This is different from metals where increasing the temperature decreases the conductivity due to increased scattering of the charge carriers. At a certain temperature, semiconductors undergo a *semiconductor-to–metal* transition where the conductivity rises abruptly. This is usually a result of overlapping electron orbitals forming wide, unfilled d or f electron energy bands. [25] This means that when the semiconductor is at lower temperatures,

conduction of the charge carriers is typically low unless the semiconductor is heavily doped.

At the nanoscale, the electronic behavior of a material becomes dominated by mechanisms that are not factors when dealing with conventional semiconductors synthesized on the micron scale. Such factors as space charge (or depletion) layer, band bending, and quantum confinement appear as dominant factors at the nanoscale. The fact that grain boundaries comprise a large percentage of the material begins to control what happens electronically when materials are synthesized at the nanoscale as well. Though the space charge layer exists on all semiconductor materials, even at the micron scale (since they do possess a surface), because of the size of the space charge layer in comparison to the bulk of the material, it is not the dominating mechanism in these larger grained materials.

When a charge develops on the surface of a material, repulsing majority carriers, a space charge region can develop. This typically happens upon adsorption of surface species. In the case of oxides, oxygen is often the likely culprit. The uncompensated charged ions that form are referred to as space charge and the region where they are developed is referred to as the space charge region or layer. [26] Positive and negative space charge layers can form above and below the surface of the material. For nanocrystalline SnO_2 in the presence of hydrogen gas, a reduced space charge region is created which allows for better charge movement as seen in Figure 3. This is because in ambient atmosphere, oxygen atoms are present which can adsorb onto the

surface of the material, increasing the amount of space charge region present at the surface of SnO_2. The height and width of the potential barrier between the grains is controlled by the concentration and nature of the adsorbed oxygen species.
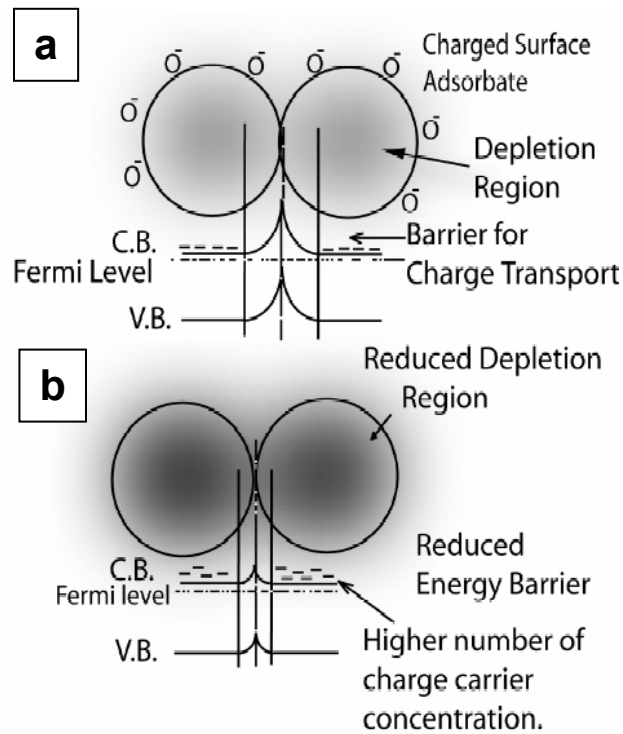
Figure 3: *Space Charge Layer Changes upon a) absorption of oxygen and b) in the presence of a reducing gas*

Some interesting consequences occur from these charges that develop on the surface of the nanomaterial. In order for the nanomaterial to be in thermal equilibrium with the "new" surface that has developed upon adsorption of species, the Fermi energy has to

be constant throughout the system. [26] To compensate for the differences in Fermi level between the positive and negative charges that have developed on the nanomaterial surface, band bending must also occur, Figure 4. Band bending refers to the local change in energy of the electrons at a semiconductor junction due to space charge effects. In Figure 4, surface adsorption of molecules (X^{ad}) leads to bending of the bands (qV_s). This leads to a change in the work function, $\Delta\Phi$.
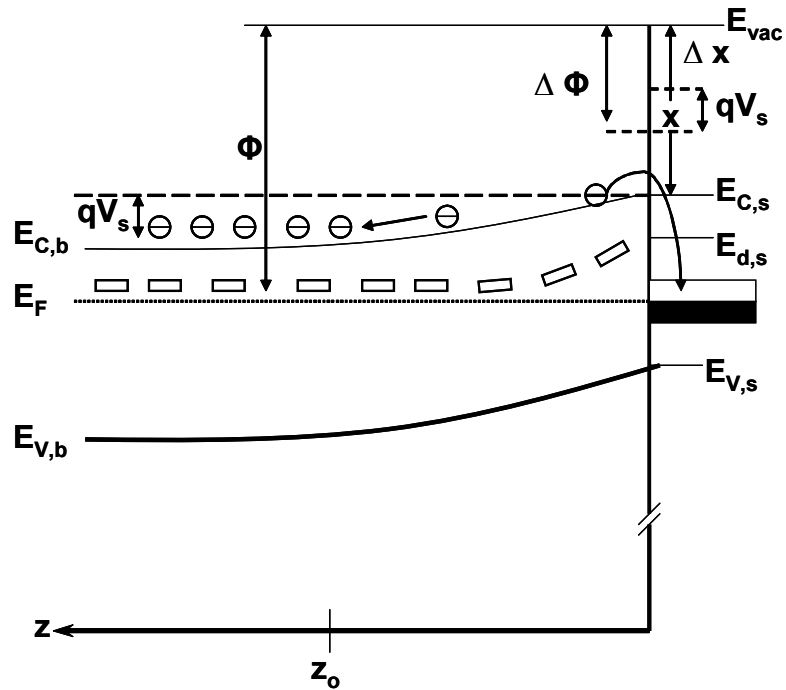
Figure 4: *Band Bending in a n-type semiconductor.*

How can we use the principles of band bending and space charge effects to an advantage in gas sensor applications? First understanding what affects the two is required. The depth of the space charge region can be described by the following equation:

$$d_{SCR} = L_{Db} \bullet \left(\frac{2\Delta E_c (x = 0)}{kT} \right)^{1/2} \quad \text{...............................(2.1)}$$

The depth of the space charge region, d_{SCR}, can be determined with knowledge of the Debye length of the material, L_{DB}, and the amount of band bending, ΔEc. The Debye length, which is a material parameter, will be a constant for a specific semiconducting system and is described by:

$$L_{Db} = \left(\frac{\varepsilon \varepsilon_o \bullet kT}{e^2 \bullet N_D} \right)^{1/2} \quad \text{..(2.2)}$$

In Equation (2.2), N_D is the number of donors in the material system. This is largely affected by doping. The Debye length describes the diffusion length of electrons as well as their penetration depth into the space charge region. [26] To take advantage of these electronic changes that occur at the nanoscale, changes in doping (to make changes in the value of N_D) and control of material surface species (in order to affect the surface

charges created upon adsorption) need to be considered. In this manner, the electronic properties can be engineered to better reflect the requirements of the application at hand.

2.3 Indium Doping of SnO$_2$

The most attractive feature of SnO$_2$ is perhaps the ability to make the crystal structure oxygen deficient, SnO$_{2-x}$, giving it the chemistry possible to change resistance based on adsorbed surface species. [27] This can often be done by changes to synthesis conditions of the material. Doping with trivalent atoms creates even more of the desired oxygen vacancies by substitution of the dopant on a tin lattice site, which in equilibrium expects a +4 charge, Figure 5. [3] This occurs because a +3 atom on a +4 site makes the tin site feel a negative charge. To compensate, an oxygen vacancy will form which feels a positive charge on the oxygen vacant site. Charge modification can be shown using *Kroger-Vink* notations as:

$$O_0^x \rightarrow \frac{1}{2}O_{2(g)} + V_o^{00} + 2e \quad \ldots\ldots\ldots\ldots\ldots(2.3)$$

$$2In^{3+} + 2Sn_{Sn}^x + O_O^x \rightarrow 2In_{Sn} + V_O^{00} + Sn_{Surface} \quad \ldots\ldots\ldots\ldots (2.4)$$
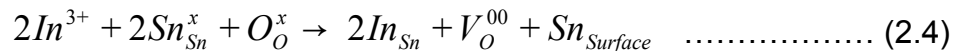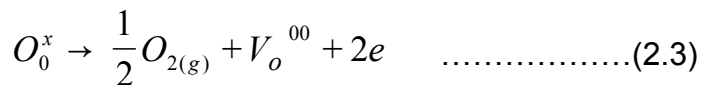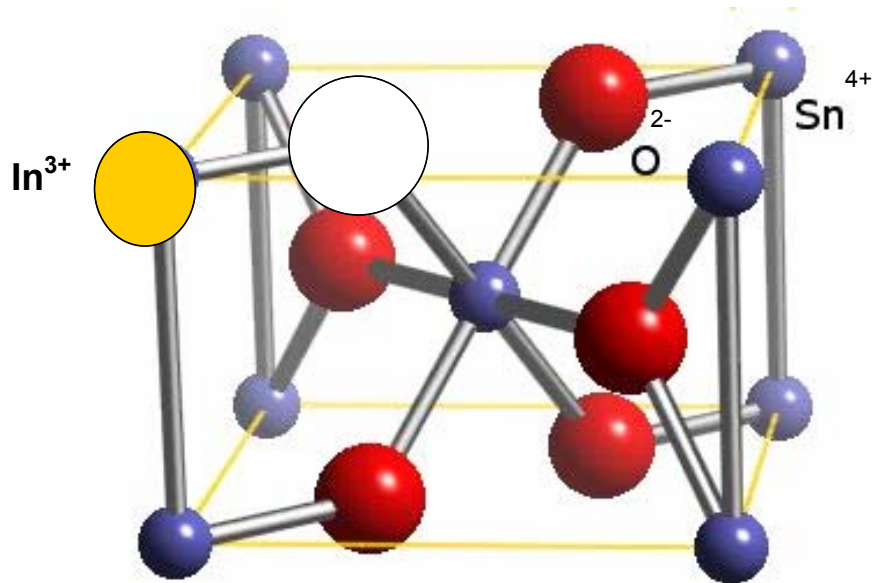
Figure 5: *Doping of SnO$_2$ with In^{3+} causing creation of a vacant oxygen site*

This charge compensation will do multiple things within the SnO$_2$ structure which will enhance its gas detection abilities, as well as, electronic abilities. First, there is possible modification of the magnitude of the space charge layer achieved by changing the free carrier density in the space charge region of the structure. Study of the major free carrier as well as their concentration in the space charge layer upon different doping amounts will give insight to the change in conduction of nanocrystalline materials. Second, an increase in surface oxygen vacant sites may help the surface dissociation reactions of gases to have immediate access to a surface site for electron injection. In most engineering materials, surfaces act as sinks for vacancies. For SnO$_2$, high surface

oxygen vacancy concentrations have been reported, especially at the nano-scale. [21, 28] This is possibly a phenomenon related to either the very small crystallite size of the nanomaterials or the special synthesis conditions to achieve these nano-oxides in the first place. Third, trivalent doping increases the number of intermediate energy levels created in the forbidden energy region of SnO_2. This increases the conduction ability of the semiconductor by reducing activation energy for conduction. [29] Due to these possible modifications, doping is a very important aspect in gas sensor development and needs to be considered.

2.4 Synthesis of nanocrystalline In-SnO$_2$

Sol-gel method was used to synthesize nanocrystalline 1%, 3%, 6.5%, and 9% mole In-SnO_2. For the sol-gel method a homogeneous solution is first prepared. The solution is then gradually dried until it becomes an amorphous solid known as the gel. The gel is then calcined at high temperatures in order to crystallize the amorphous solid and to also get rid of any unwanted organic chemicals post synthesis. [30]

For the synthesis of nanocrystalline In-SnO_2, a solution of tin isopropoxide and indium isopropoxide in isopropanol and toluene are first prepared. The solution was allowed to stir covered with paraffin tape for one hour at room temperature. Dip coating for the thin films is then performed on cut silicon (100) wafers with an oxidized layer. Heating of the substrates then occurs at 150°C for 15 minutes. Upon cooling, substrates are again

dipped into the solution and dried again at 150°C for 15 minutes. With the remaining solution, a small amount of polymer, hydroxypropyl cellulose (HPC), is added to control the grain size during the gelling reaction. The solution is then left exposed to air at room temperature, stirring, until the gelling is completed. The gel is then dried at 150°C for one hour. Substrates and powders are then calcined at 400° C, 500° C, 600° C, 800° C, and 1000° C for one hour in air. The subsequent drying and pyrolysis treatments of the coated polymer nanostructures then results in the decomposition of the polymer structure leaving behind In- SnO_2 nanocrystallites.

Following are the anticipated sol-gel reactions during the drying and pyrolysis procedures [4]:

1. $Sn(OC_3H_7)_4 + 4H_2O \rightarrow Sn(OH)_4 + 4C_3H_7OH$ (at 25° C)
2. $Sn(OH)_4 \rightarrow SnO_2$ (amorphous) + $2H_2O$ (at 150° C)
3. SnO_2 (amorphous) $\rightarrow SnO_2$ (crystalline) (at 400° C)

Indium doped SnO_2 samples with ceria also doped into the system at 3.5 mole % were also prepared by the sol-gel method. The sol gel procedure was as followed above with the exception of the beginning step. Initially for these samples, cerium nitrate was dried in air and then tin isopropoxide and indium isopropoxide were mixed with the dried cerium nitrate. The rest of the synthesis procedures for this material were as previously mentioned.

One dimensional nanorods of SnO_2 were also synthesized for gas sensor testing by a hydrothermal technique first proposed by Chen et al. [31].   A solution of 0.5M $SnCl_4(5H_2O)$ was stirred with 5M NaOH at room temperature. After complete mixing, the solution was then mixed with an ethanol and water mixture. The complete mixture was then poured into a Teflon lined Digestion Bomb (to 50% capacity) and heated at 200°C for 24 hours. After naturally cooling the entire Digestion Bomb to room temperature, the remaining product was washed in distilled water several times, allowing the product to settle out each time. The anticipated reactions for the formation of the one dimensional nanostructures are as follows:

1) $SnCl_4 + 4NaOH \rightarrow Sn(OH)_4 + 4NaCl$

2) $Sn(OH)4 \rightarrow SnO_2 + 2H_2O$ (200°C, under pressure)
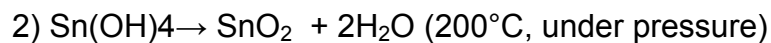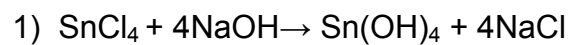
CHAPTER THREE: STRUCTURAL AND CHEMICAL CHARACTERIZATION

3.1 Structural Characterization

X-ray Diffraction (XRD) is a technique used to gain crystallographic information about materials. This technique also has the ability to give information about such structural properties as grain size, strain, and preferred orientation, to list a few. This technique is considered non destructive and can be used in most environments [32]. Typically, the diffracted intensity is measured as a function of 2Θ and the orientation of the sample. The output from this technique is a diffraction pattern which acts as a fingerprint for specific atomic arrangements pertaining to a specific crystal structure. Positive phase identification can be obtained from XRD.

High Resolution Transmission Electron Microscopy (TEM) is widely known for its high lateral spatial resolution. In TEM, a highly focused electron beam is focused onto a sample for transmission through the sample. Below the sample is a detector which collects the transmitted signal. Magnification of this spatial information can be as much as a factor of 10^6, and is achieved by the small wavelength of the incident electrons. [32] This makes TEM an excellent and necessary technique to employ when studying nanomaterials.

Structure studies were carried out using X-ray Diffraction (Rigaku Model) with a Cu-K$_{\alpha 1}$ radiation and the optimized operating conditions of 30mA and 35kV. The scan rate was set at 2.5 degree per minute with a step size of 0.05 degrees. XRD data showed that the tetragonal form of SnO_2 has formed by 500°C, Figure 6. Dominant peaks at (110), (101), and (211) confirms the cassiterite structure of nanocrystalline SnO_2 that is preferred for gas sensing applications. The (110) is the dominant crystal structure of the low-index crystal faces for this material due to its stability. This is the desired structure of SnO_2 for sensing applications since its prevalent (110) growth plane is extremely stable and can reject oxygen with little distortion. [33] Growth of this plane helps in achieving high oxygen vacancy concentrations at low temperatures. At 800°C, evidence appears of a separate, but not well formed In_2O_3 phase known as bixbyite, Figure 6. XRD was also performed on undoped SnO_2, Figure 6.
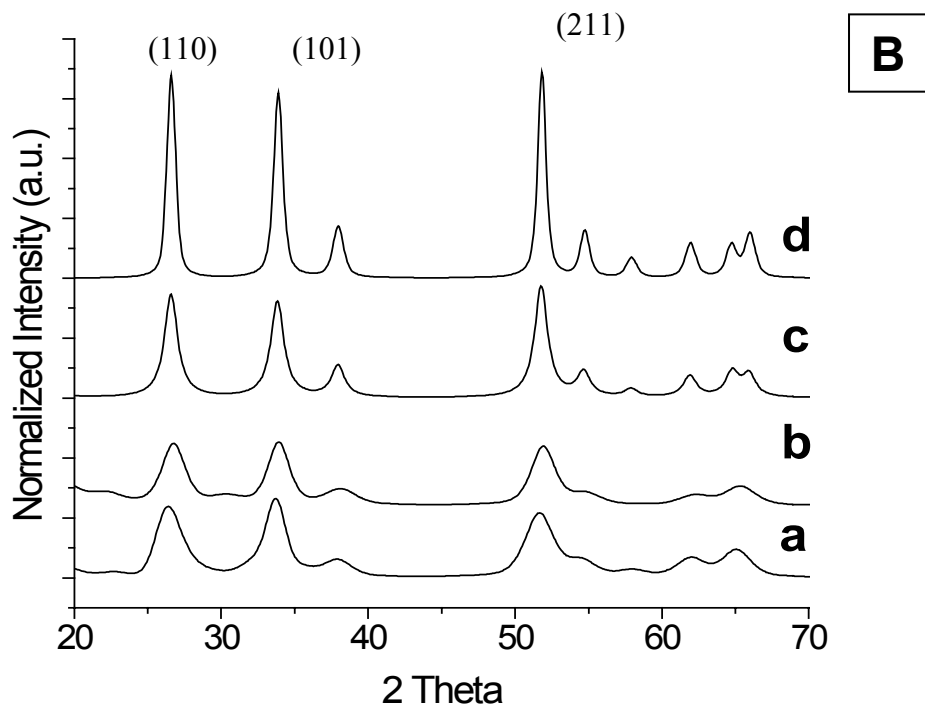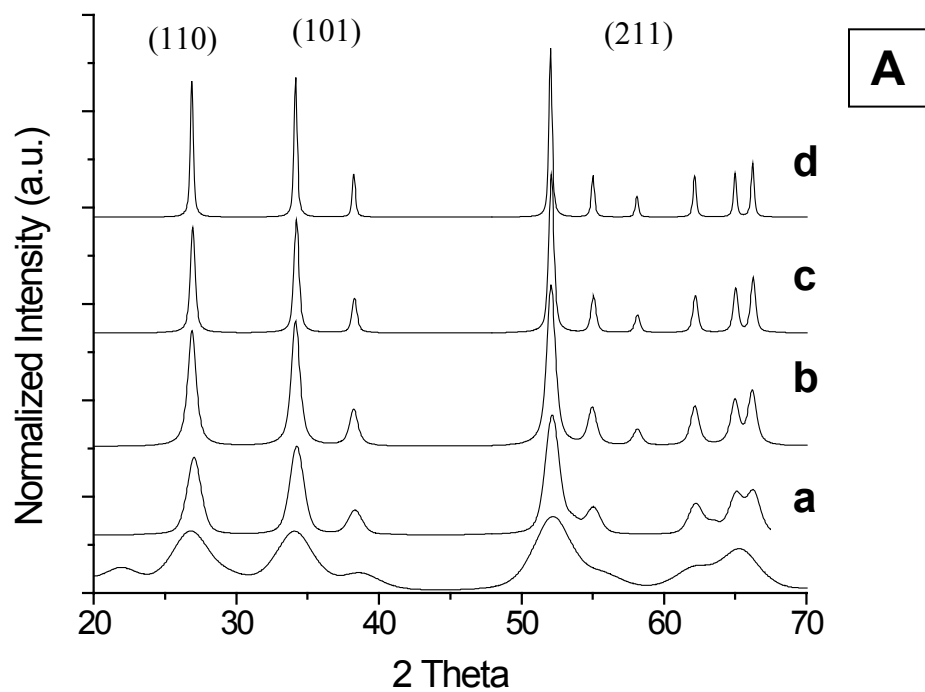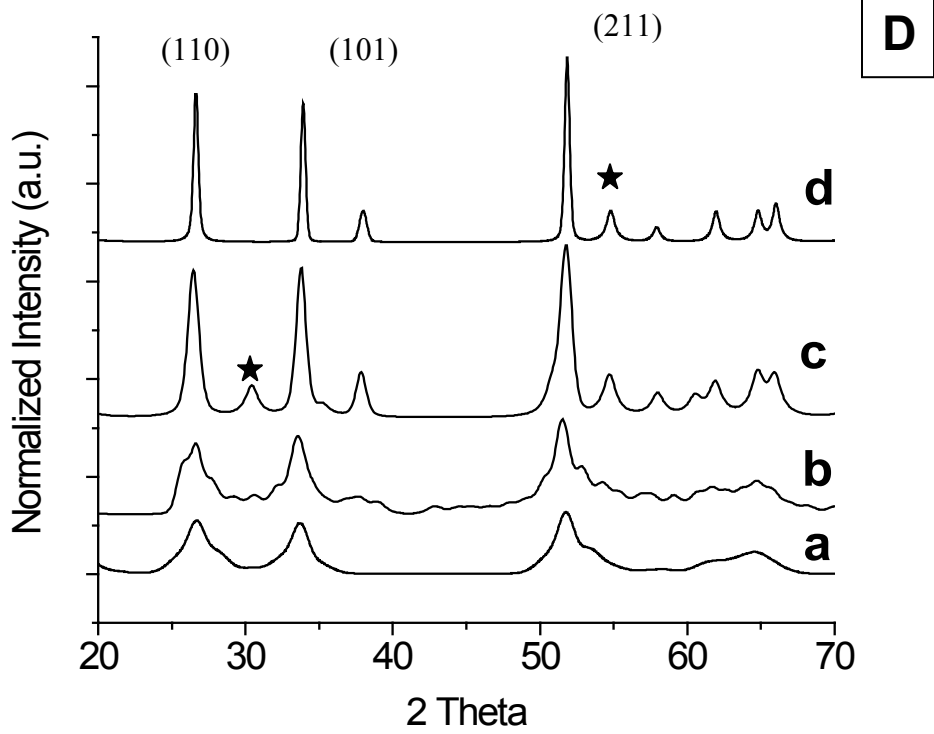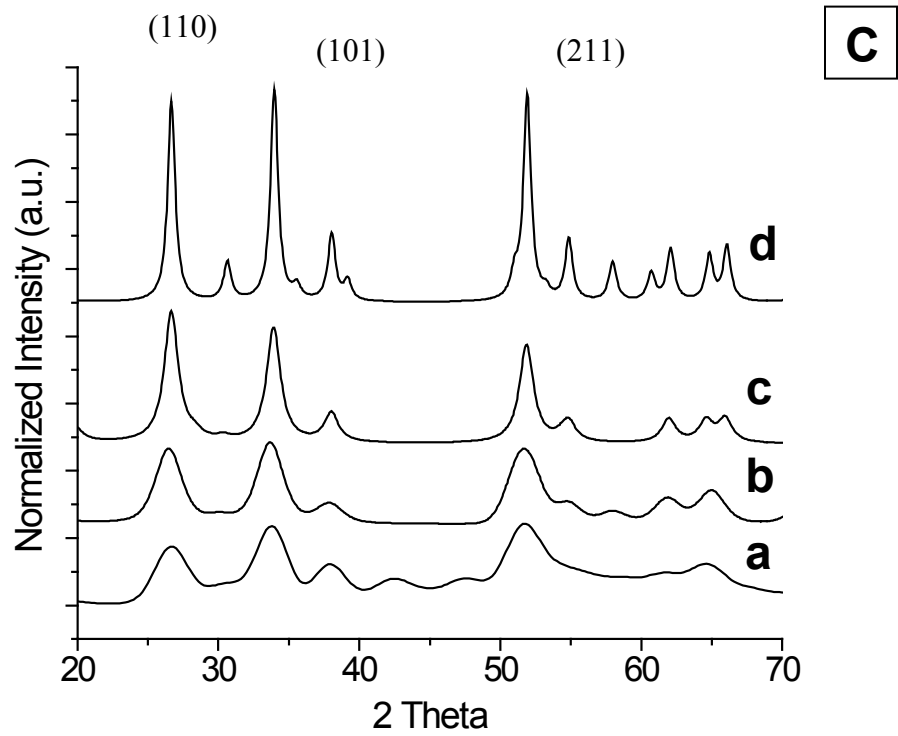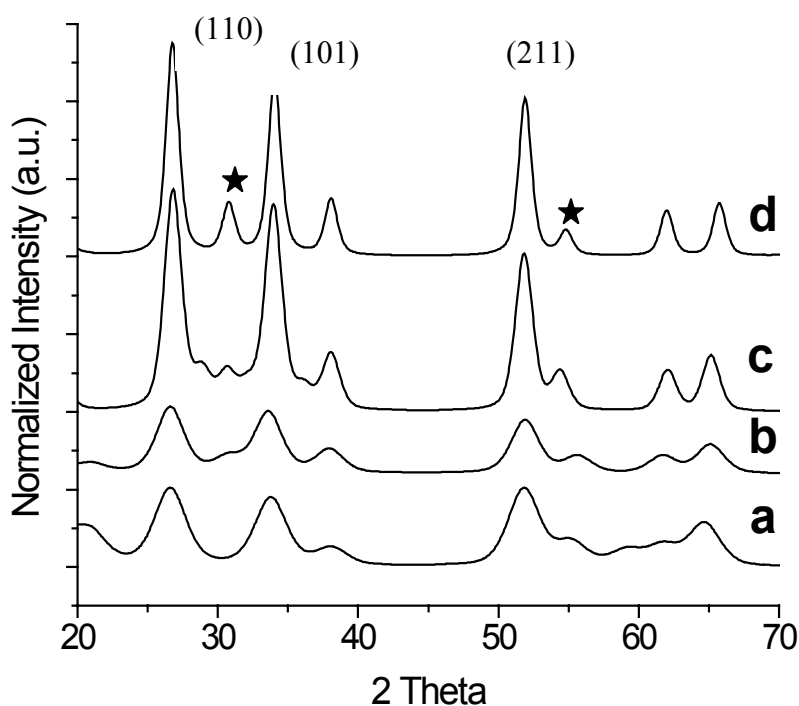
Figure 6: *X-ray Diffraction of A) SnO₂, B) 1% In doped SnO₂, C) 3% In doped SnO₂, D) 6.5% In doped SnO₂, and E) 9% In doped SnO₂ calcined at a)500°C, b)600°C, c)800°C, and d)1000°C. In₂O₃ peaks indicated by ★*

From XRD experiments, a few extra peaks not associated with the cassiterite structure appear to be beginnings of a not fully formed In_2O_3 (bixbyite) structure at calcination temperatures above 800° C, Figure 6. These peaks do not appear for the undoped SnO_2 particles, Figure 6. This would indicate an amorphous In_2O_3 structure on the surface of the SnO_2 particles that segregates at higher calcining temperatures. At lower calcining temperatures, complete doping of the indium into the structure seems likely. A similar effect has been reported by Carreno and coworkers [34] for rare earth (Ce, Y,

and La) doped SnO_2 nanoparticles. The rare earth dopants are segregated to the particle surface at temperatures above 900°C.

Dopant segregation to the particle surface is likely detrimental to the cause of enhancing the performance of gas sensor materials. Since nanomaterials have such large surface areas compared to conventional engineering materials, any modifications to the surface cannot be considered minor. Any interaction with the surface by a gas or molecule will be affected by any changes made to the surface of the material. This will become evident in the later chapters when room temperature gas sensing is being tested.

XRD was also performed on the Ce, In doped nanocrystalline SnO_2 samples, Figure 7. It can be seen from the figure that at low calcination temperatures, only peaks for SnO_2 are present. At the higher calcining temperatures (800°C and 1000°C), ceria peaks become evident, indicating that it has formed a separate phase. Even the sample calcined at 600°C shows signs of the beginnings of a separate ceria phase. This separate ceria phase is likely on the surface of the SnO_2 particles. This effect was reported on by Carreno et al at temperatures above 900°C, for Ce doped into SnO_2 nanoparticles. [34] The segregation of the Ce atoms over the In atoms is likely due to the size difference between the two atoms. Indium is much closer in size to a tin atom and will more easily substitute and dope into the SnO_2 crystal lattice compared to the much larger cerium atom.
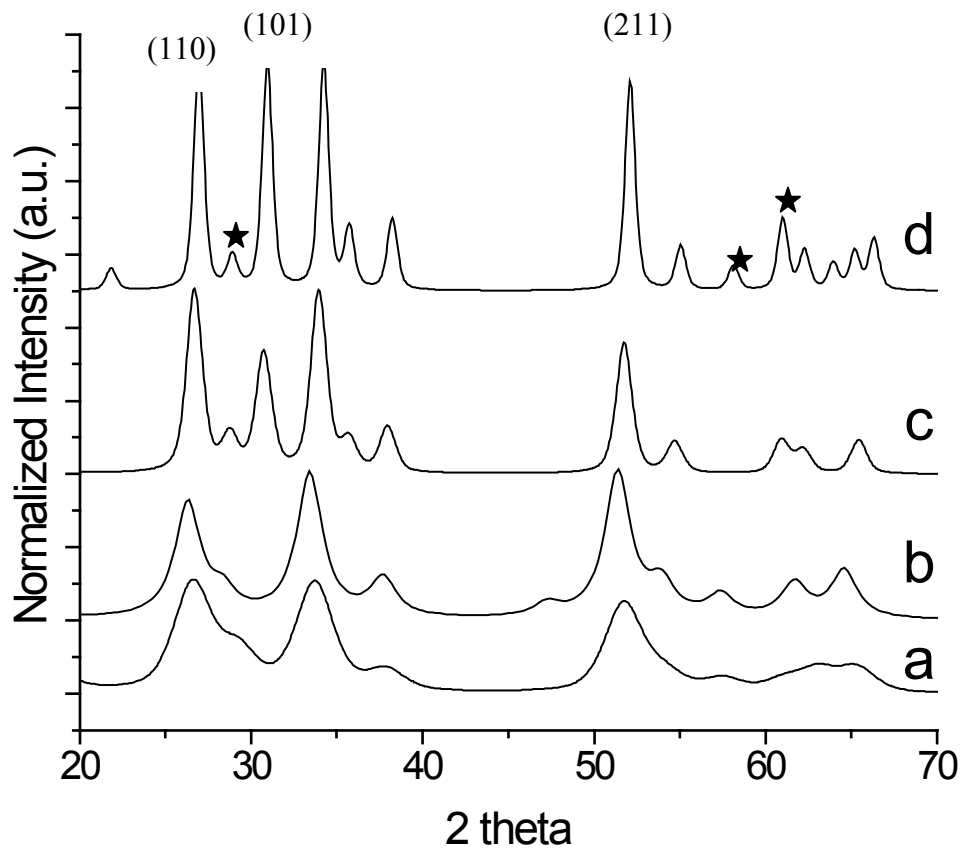
Figure 7: *XRD of Ce, In-SnO₂ calcined at a) 500°C, b) 600°C, c) 800°C, and d) 1000°C. Ceria peaks indicated by* ★

The average crystallite sizes at different calcining temperatures were determined using the SnO₂ (110) diffraction peak and the Scherrer equation:

$$D = \lambda K \big/ \beta \cos\theta \quad \dots\dots\dots\dots\dots\dots\dots\dots\dots\dots\dots(3.1)$$

Where λ is the wavelength (Cu-K$_{\alpha 1}$ radiation), θ is the diffraction angle, K is a constant, and β is the full width at half maximum. All of the indium doped SnO$_2$ samples were nanocrystalline in nature after calcination at or above 500°C, Table 1. For one hour calcinations in air at 500°C, 600°C, 800°C, and 1000°C, the crystallite sizes are 4nm, 5nm, 8nm, and 13nm, respectively for samples doped with 6.5% Indium. These were confirmed to be close to the actual particle size using High Resolution Transmission Electron Microscopy (HRTEM). Necks seem to have formed between grains at 800°C and 1000°C, possibly due to In$_2$O$_3$ growth at the grain boundaries, Figure 8.

Table 1: Crystallite size changes based on Indium doping and calcination temperature

Calcining T		1%In	3%In	6.5%In	9%In
500°C	Crystallite Size (nm)	4	3	3	3
600°C		5	4	4	4.1
800°C		8.2	8	6	10
1000°C		13	14	19	17.3

The surface morphology of the SnO_2 nanoparticles was determined by High Resolution Transmission Electron Microscopy (HRTEM) [Philips (Tecnai series)] operated at a 300 kV accelerating voltage. Figure 8 shows the HRTEM images of the In doped SnO_2 nanoparticles calcined at 500°C, 600°C, 800°C, and 1000°C. Comparison between the particle sizes observed by TEM and those calculated using XRD; it was observed that each individual grain was a single crystal at the lower calcination temperatures. This helps in reducing the barriers for conduction of the free carriers between the grains. Due to this very reason, the space charge variations can be considered the dominating conduction mechanism. The Selected Area Electron Diffraction (SAED) pattern shown in Figure 8b confirms the growth of the In-SnO_2 particles in the (110) plane of the cassiterite structure.
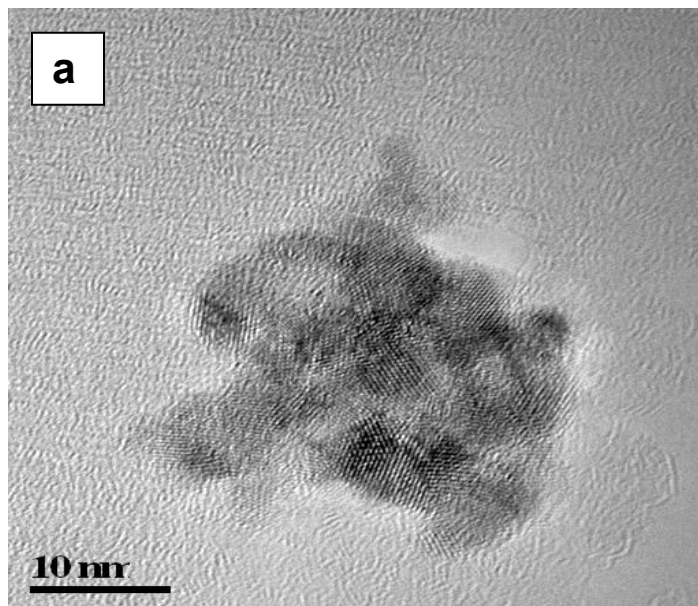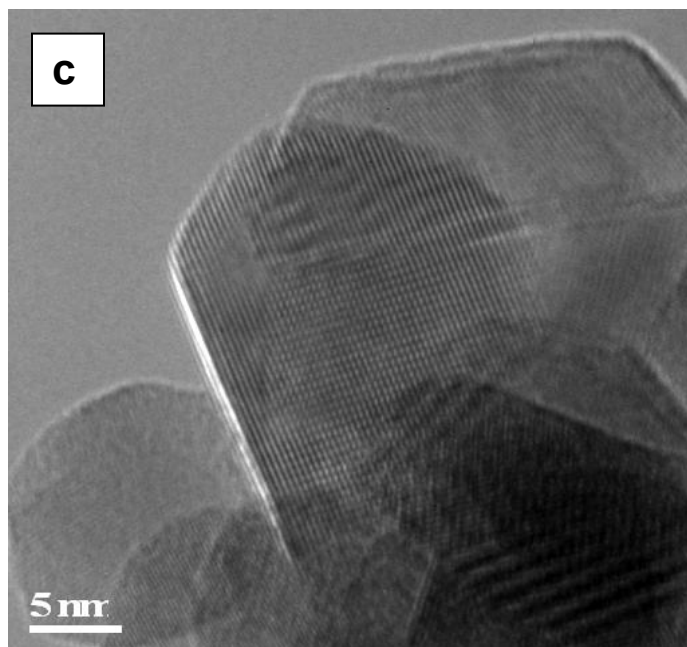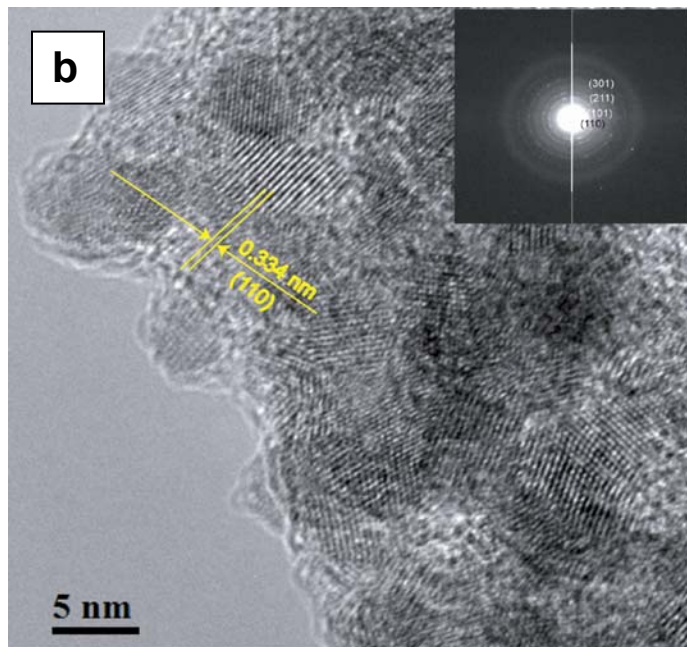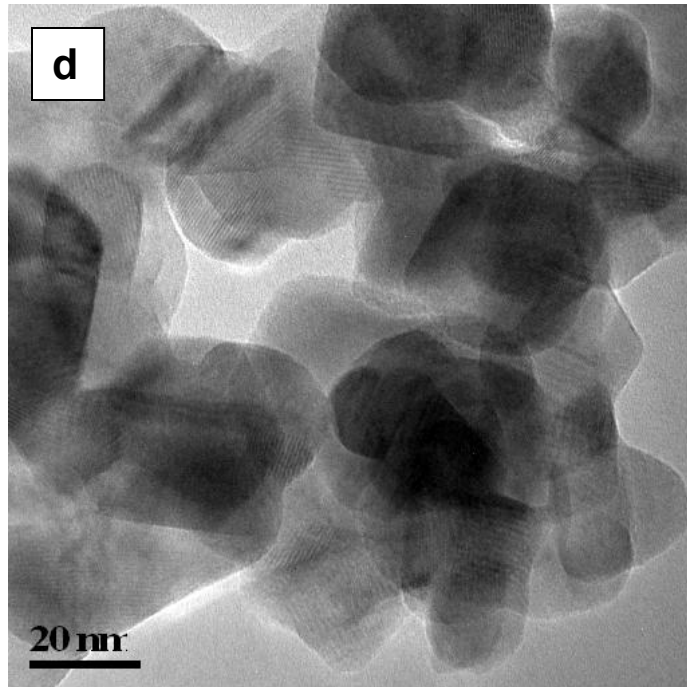
Figure 8: *HRTEM of doped SnO$_2$ samples calcined at a) 500°C, b) 600°C, c) 800°C, and d) 1000°C*

HRTEM was used to analyze the effective grain size, Figure 9. The lattice constants *a* and *c* were analyzed from the selected area electron diffraction to gain understanding of doping on the microstructural evolution of the material. The normal lattice constants of the SnO$_2$ cassiterite structure are *a*=*b*=4.731 Å and *c*=3.189 Å. It can be observed that for the undoped SnO$_2$, the lattice parameter *a* remains fairly constant. For the 6.5% In doped SnO$_2$, the lattice constant *a* decreases with increasing calcination temperature. For undoped SnO$_2$, the lattice constant *c* again remains fairly constant. The values of *a* and *c* are low compared to published values for SnO$_2$ and may be due to an oxygen

29

deficient structure. It can be observed that the largest lattice constants belong to the 6.5% In-SnO$_2$ samples calcined at 600°C, taking into account both the *a* and *c* lattice constants. This seems to indicate that the enlarged cell structure is due to a maximum accommodation of indium atoms into the SnO$_2$ lattice. The decreasing lattice constants with increasing calcination temperature suggest that a lower amount of indium is doped into the structure at these calcination temperatures. This also indicates that the oxygen vacant sites are left behind and that bulk diffusion of oxygen into the crystal lattice to compensate these vacant sites is not occurring. This may be occurring due to the fact that as the indium atoms segregate to the surface and begin to form In$_2$O$_3$, oxygen does not diffuse down into the bulk structure at short calcination times.
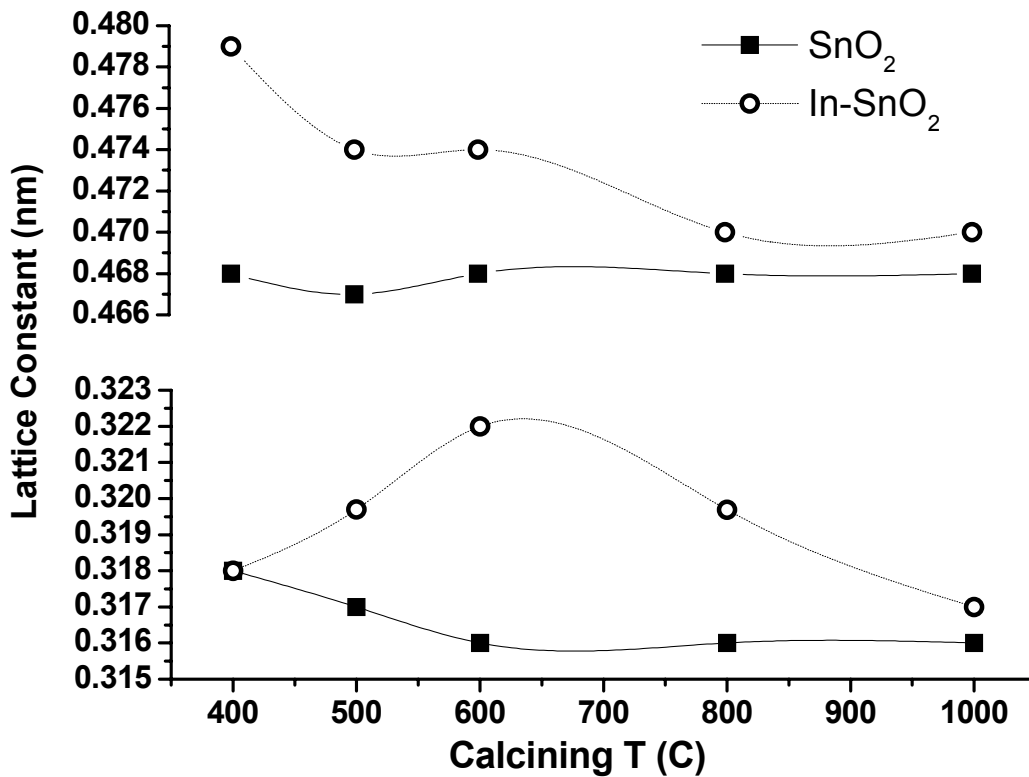
Figure 9: *Changes in Lattice Parameter of SnO$_2$ with and without doping*

Vegard's law is an approximate empirical rule which holds that a linear relation exists, at constant temperature, between the crystal lattice constant of an alloy and the concentrations of the constituent elements. Using Vegard's law for comparing the changes in lattice parameters, the amount of indium doped into the SnO_2 structure was analyzed. The expansion of the SnO_2 crystal structure was analyzed by comparison of the lattice parameters for the different calcining temperatures. At higher calcinations temperatures, approximately 2% of indium is doping into the SnO_2 structure, while at lower calcination temperatures it appears that close to 3% of the indium is doping (fully) into the structure. Thermodynamically, 2.5% doping with indium is possible in SnO_2 at equilibrium. [35] But if one is to consider in increase in the amount of oxygen vacant sites that may be created with an increase in doping with indium, these changes in the lattice parameters are likely a trade off between the incorporation of indium atoms to the contraction that would occur upon introduction of an oxygen vacancy. Comparison with XRD seems to confirm this trade off. Because of this, it is possible that this nanocrystalline SnO_2 system is able to accommodate dopings above what is predicted for the system.
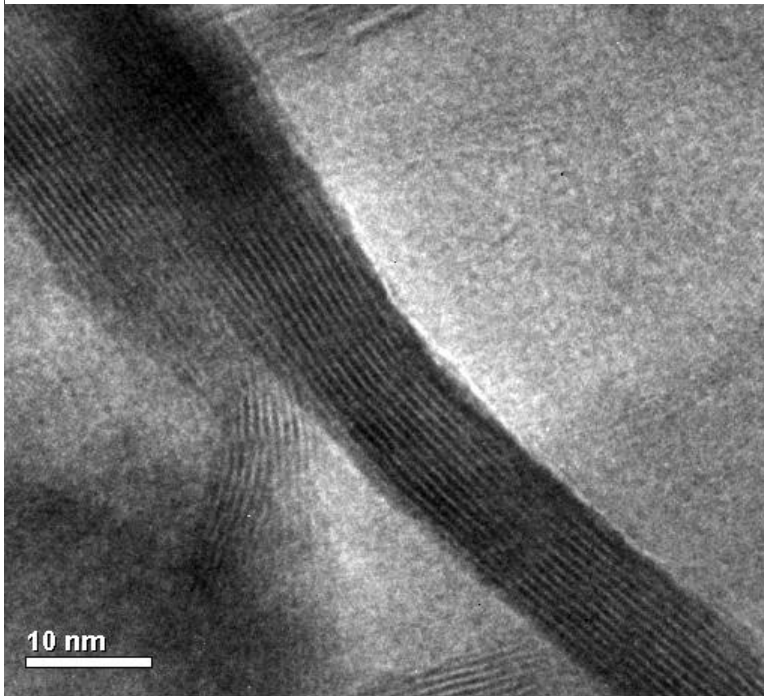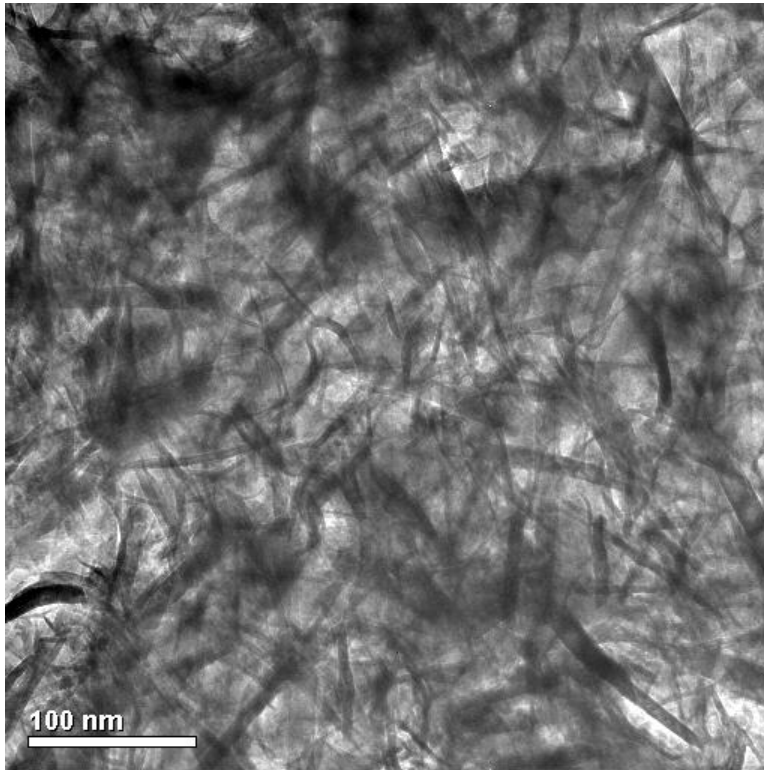
Figure 10: *TEM of 1D SnO₂ nanorods*

HRTEM was also performed on the one dimensional SnO_2 nanorods synthesized by a hydrothermal method. Figure 10 shows the TEM micrographs of the one dimensional nanorods. From Figure 10, it can be identified that the SnO_2 nanorods are approximately 10-20 nm in diameter, and approximately 100-150 nm in length. It can also be noted that the nanorods appear to be single crystalline in nature.

3.2 Surface Characterization

X-ray Photoelectron Spectroscopy (XPS) is a technique where monoenergetic X-rays bombard a sample and cause electrons to be ejected. A detector then measures the energy of the ejected electrons. [32] With this technique, one can identify the elements present in the sample. This is achieved by measuring the binding energy of an electron from the kinetic energy of the photoelectron. This comes from the Einstein photoelectric law [29]:

$$KE = hv - BE \text{...(3.2)}$$

In Equation (3.2), KE stands for the kinetic energy, hv is the energy of the photon, and BE is the binding energy of the particular atom to the atom concerned. With XPS, it is

also possible to identify the chemical state of elements present from small variations in the kinetic energies.

The surface chemistry was studied on the 6.5% nanocrystalline In-SnO$_2$ using X-ray Photoelectron Spectroscopy (XPS). Findings show a change in the surface chemistry with a change in calcination temperature. The change with calcination temperatures, and correspondingly particle size, in the Oxygen 1s peak is shown in Figure 11. The peaks with strong shoulders to the left (red peaks) indicate a large presence of surface oxygen vacancies. The left shoulder indicates a surface ratio of one tin atom to one oxygen, as opposed to the stoichiometric one tin to two oxygen. These were more evident in the smaller size SnO$_2$ nanocrystallites. This indicates that at very small crystallite sizes, a more oxygen deficient structure is present. With increasing calcination temperature, it appears that the nanocrystalline material has the energy available to become more stoichiometric.
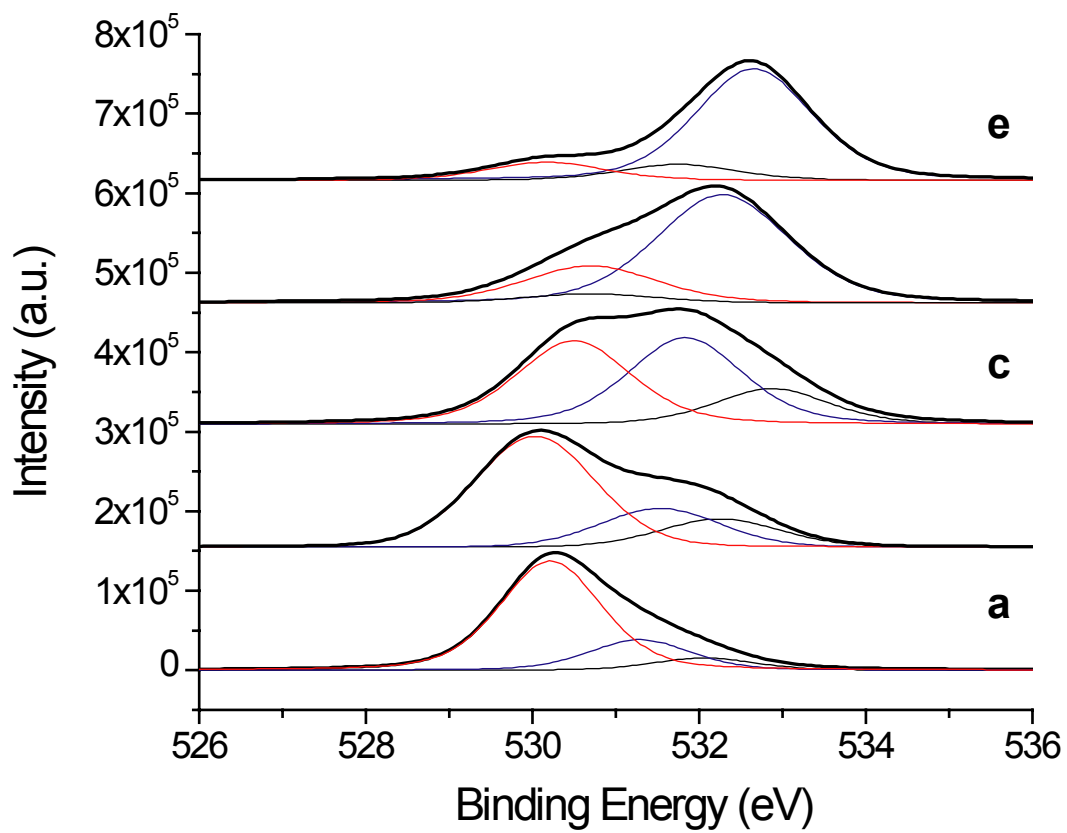
Figure 11: *O1s peak from XPS of In-SnO$_2$ calcined at a) 400°C, b) 500°C, c) 600°C, d) 800°C, and e) 1000°C*

CHAPTER FOUR: FOURIER TRANSFORM INFRARED SPECTROSCOPY

4.1 Background

Fourier Transform Infrared Spectroscopy (FTIR) is used with the basic goal of determining changes in the intensity of infrared light as it interacts with a material as a function of wavelength. This technique is able to give information on the chemical bonding in a material and is also non-destructive. [32] The basic function of the technique is that light is dispersed from a broadband infrared source and then measures its intensity at each frequency. An example of the FTIR set up used for these experiments is shown in Figure 12.

In FTIR analysis there are 3 commonly examined pieces of data. Those are the peak position, the peak width, and the peak intensity. The peak position is probably the most commonly used for identification of materials. These peaks are unique since at characteristic frequencies, certain functional groups will display their own set of peaks. This is because infrared techniques measure the vibrational energies of the molecules. In order for a molecule or functional group to be IR active, the dipole moment of the molecule must change.
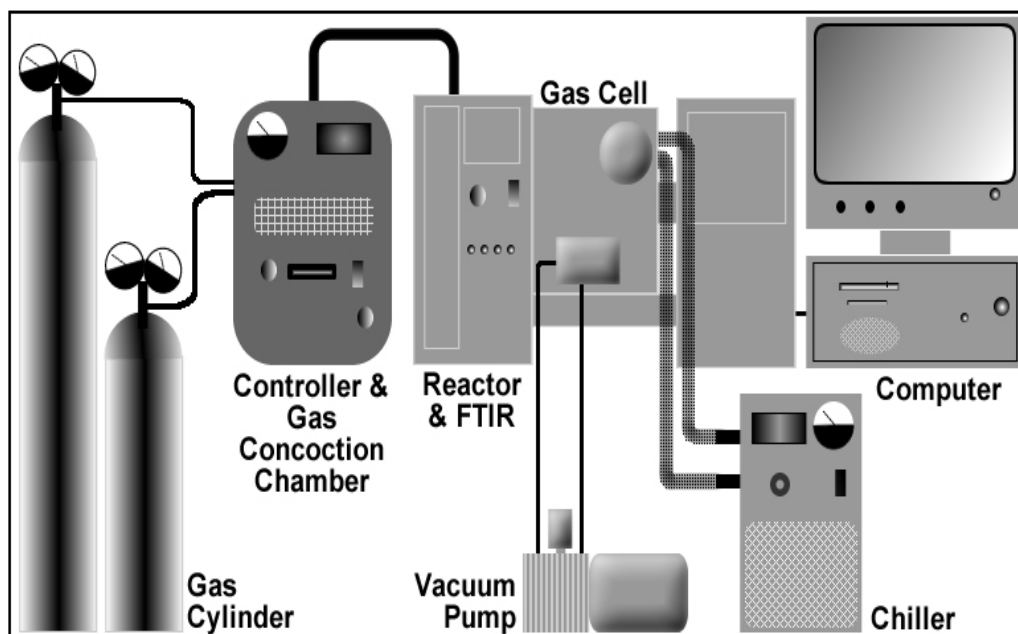
Figure 12: *FTIR set up*

When the desired sample for testing is opaque, transmission experiments are not practical. To overcome this problem, reflection experiments in the FTIR become more appropriate. Special accessories are usually required to achieve this. In order to use FTIR on our powder samples, an accessory known as the Praying Mantis was used, Figure 13. The Harrick Praying Mantis allowed for diffuse reflectance measurements to be collected. Diffuse Reflectance Infrared Fourier Transform Spectroscopy (DRIFTS) is a technique that collects and analyzes scattered Infra-red energy. It is often used for measurement of fine particles and powders, as well as for samples that possess rough surfaces. This can include the adsorption of molecules onto the particle surface, which

is useful for the prescreening of gas sensor materials. Very little sample preparation is usually required.
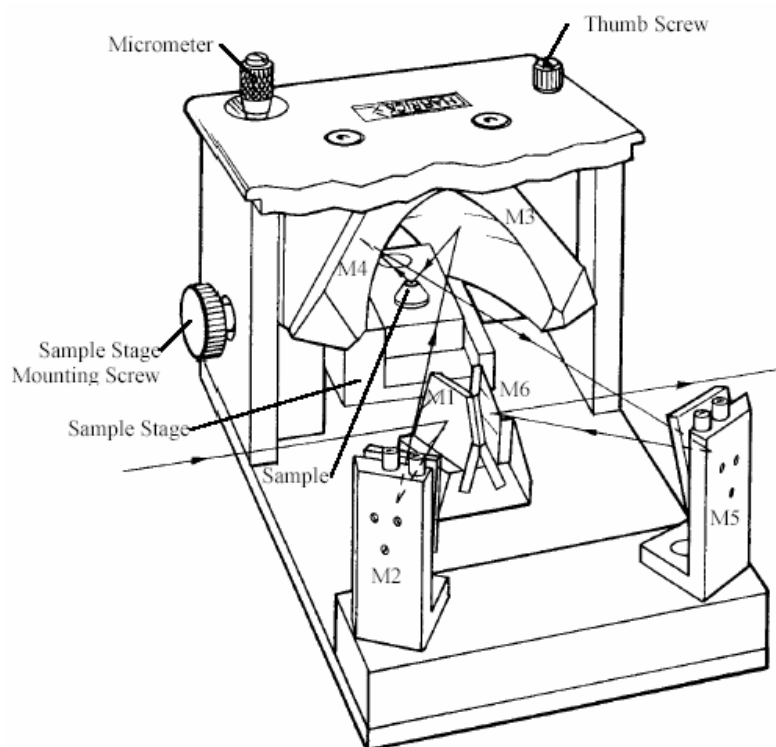
Figure 13: *Sample holder for Praying Mantis accessory*

One of the unique features of the Harrick Praying Mantis accessory is the ability to heat samples being tested. The catalytic cell, as it is sometimes referred to, can heat samples to a testing temperature of 600°C. Another unique feature of the Praying Mantis is the ability to introduce gases to the sample during testing as well as the ability to put the sample being tested under vacuum. These features make the accessory an excellent tool for prescreening of materials for gas sensor applications, since target gases can be directly tested.

Diffuse reflection is defined as the reflection of light from an uneven or granular surface such that an incident ray is reflected at a number of different angles. It is the complement to specular reflection. In specular reflection, a mirror like reflection of the incident light occurs. With use of the Praying Mantis, diffuse reflectance is collected and the accessory minimizes the detection of the specular component. This minimizes the intensity of restrahlen bands caused by the specularly reflected light, making the data collected easier to analyze.

FTIR is a technique often used to investigate optical properties of materials, often absorbance and transmission in the infra-red region. It has been shown that in semiconducting materials, absorbance is due to free carriers in the space charge region. [36] At the time of this finding by N.J. Harrick, in the early 1960's, this was not very technologically significant. At the time, advanced engineering materials were on the order of microns, and today, many still are. The space charge layer of many oxides is only a fraction of the size of the material since it is a phenomenon related to the

surface of a material. The role of the space charge layer is not significant for controlling the conduction of semiconductors on the micron level; bulk conduction of charge carriers is the controlling factor. In nanomaterials the situation is different. The amount of free carriers in the space charge layer of nanomaterials is extremely important, since this controls conduction through the grain of the material. Ability to monitor the changes within the space charge layer with doping, particle shape, morphology, and synthesis conditions while monitoring the materials response to different gases makes FTIR a valuable tool for screening nanomaterials for gas sensor applications. It also helps in better understanding the nanomaterial's chemistry when reacting with different gases.
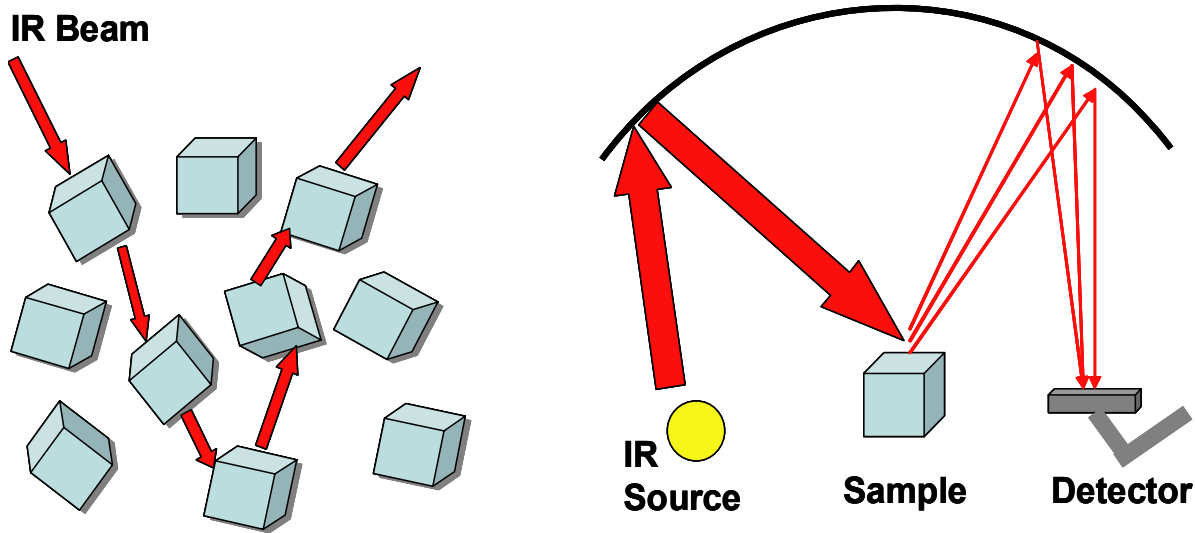
Figure 14: *IR beam interaction in Diffuse Reflection Mode of the FTIR*

When the infra-red beam enters the sample, Figure 14, it can be reflected, transmitted, or absorbed. The infra-red energy reflecting off the surface is typically lost. The infra-red beam that passes through a particle can either reflect off the next particle or be transmitted through the next particle. Scattered infra-red energy is collected by a spherical mirror that is focused onto the detector, Figure 14. These are the basics of how the Diffuse Reflectance mode of the FTIR works.

Diffuse Reflectance mode of the FTIR (DR-FTIR) can be can be successfully used for studying the surface chemistry variation of materials. [35] There have been few studies that have shown that the variation in infra-red absorption of materials can be correlated to their variation in free carrier densities on the material surface [37]. Absorption by free carriers on the surface in the space charge region may differ from that in the bulk and needs to be studied when dealing with adsorption of gas species onto the surface of the material [27]. Beer's Law shows that the absorbance can be directly related to the absorption coefficient using:

$$I = I_0 \exp(-Kx)$$ ………………………………… (4.1)

In Equation (4.1), x is the thickness of the measured sample and K represents the absorption coefficient of the sample. For semiconductors in the infra-red region, data at wavenumbers of unaffected surface species are utilized in calculations. This is typically referred to as the broad background of the sample. Drude-Zener theory was used to

calculate the conductivity as well as the major free carrier concentration using the following relationship:

$$K = \frac{1}{\varepsilon_0 c_0 n} \frac{\sigma^2 q^2}{\omega^2 m^2 \mu^2} = \lambda_0^2 \frac{\sqrt{\mu_0}}{\sqrt{\varepsilon_0}} \frac{N q^3}{4 \pi^2 n m^2 c_0^2 \mu} \quad \text{............. (4.2)}$$

In Equation (4.2), N is the free carrier concentration (m^{-3}), σ is the electrical conductivity (S/m), ω is the angular frequency, m is the carrier effective mass (kg), μ is the carrier mobility (m^2/(Vs)), n is the index of refraction, and λ_o is the wavelength in free space ($1/n = \lambda / \lambda_o$). Equation (7) is valid when $\omega t \gg 1$, and $\sigma_o \ll \omega\varepsilon'$, which holds up in the infra-red region for most semiconducting materials. Drude- Zener theory assumes classical statistics, but quantum effects are important below a critical wavelength at a given temperature. Spitzer *et.al.* [39] have shown that the right hand side of Equation (4.2) for the absorption coefficient needed to be corrected by a factor of:

$$\sqrt{\frac{h\omega}{2\pi k T}} \quad \text{when} \quad h\omega \geqslant 2\pi k T \quad \text{.................. (4.3)}$$

This is an important consequence for nanomaterials in the infra-red region. For low temperatures in the infra-red region this relationship is required. This leads to a $\lambda^{3/2}$ variation with wavelength for the conductivity of oxides in the infra-red region.

Combining Equations (4.2) and (4.3) and then solving for N leads to the following relationship for the free carrier concentration:

$$N = \frac{nKm^2 c_o^2 \mu}{\lambda_o^2 q^3} \sqrt{\frac{32\pi^6 k\varepsilon_o T}{h\omega\mu_o}} \quad \text{………….........................(4.4)}$$

4.2 FTIR Studies

FTIR studies were carried out using a Perkin Elmer FTIR spectrometer with a Harrick Praying Mantis accessory, in order to take Diffuse Reflectance measurements of the samples. The spectral resolution of the instrument was set to 4 cm^{-1}. Samples were mixed in a ratio of 2% sample to 98% KBr (potassium bromide) by weight. Sample powders and KBr were then mixed together and cleaned before testing to remove any irrelevant impurities from the sample surface. This was performed by heating the KBr powders at 120° C for 24 hours in hour to evaporate off any surface contamination and adsorbed water. After heating the KBr by itself it was then mixed with the sample powder and the new mixture was heated at 120° C under vacuum for 15 minutes, again to drive off any surface contamination. The samples were then allowed to cool to room temperature (30°C) before beginning testing.

Figure 15 shows the variation of FTIR absorbance spectra from doped nanocrystalline SnO$_2$ samples. It can be observed from the figure that there is an upward shift in the absorbance spectra after exposure to hydrogen gas. For nanocrystalline SnO$_{2-x}$, when exposed to air, oxygen molecules are physisorbed on the surface and are able to take free electrons from SnO$_{2-x}$. This leads to a subsequent change from O$_2^-{}_{ads}$ or O$^-{}_{ads}$ species. When a reducing gas (such as hydrogen) comes into contact with these nanoparticles, they are oxidized via reaction with the O$_2^-{}_{ads}$ or O$^-{}_{ads}$ species, and subsequently, electrons are reintroduced into the electron depletion layer. These electrons added to the space charge region of an n-type surface will lead to an increase in the absorption (see Figure 15) [40]. These excess electrons have the ability to absorb more energy for conduction, hence the increase in the absorption of the absorption spectra. A decrease in absorption would have been noted if an oxidizing gas that was able to react with the surface of the SnO$_2$ surface would have been introduced to the sample.

Absorbance changes were appreciable within 5 minutes of hydrogen flow for the doped SnO$_2$ samples that were able to sense hydrogen gas when tested at higher temperatures (>100°C). The broad peak around 3450 nm^{-1} is due to physisorbed water bending or surface hydration, Figure 15. [33] This is likely a consequence of the sol-gel synthesis used to obtain SnO2 in nanocrystalline form.
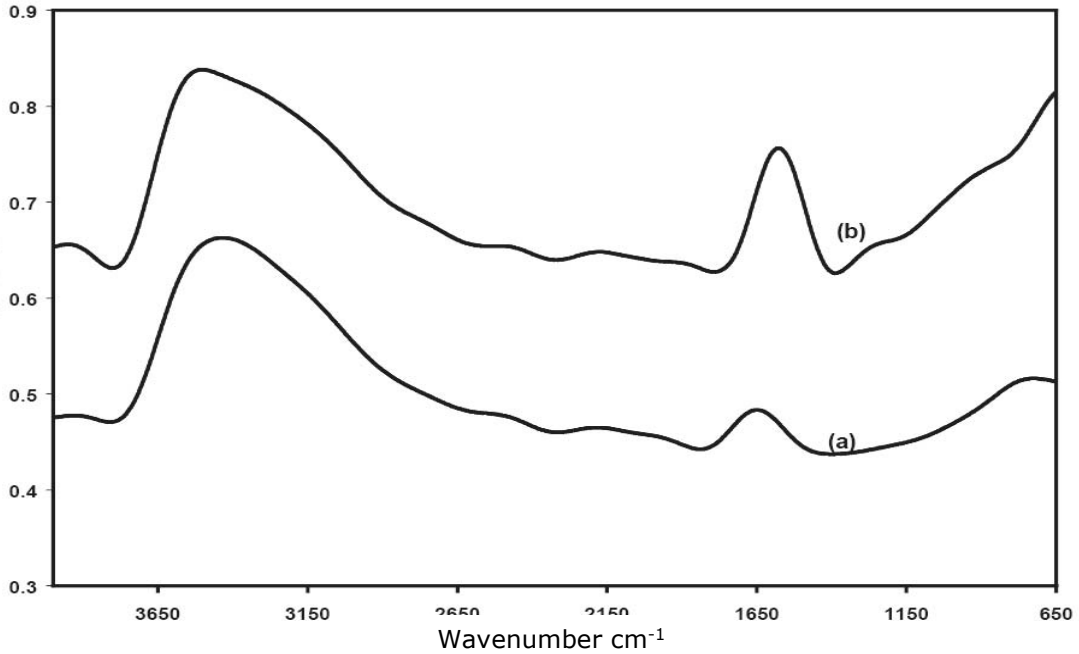
Figure 15: *Absorbance Spectra of Nanocrystalline In-SnO₂ a) before and b) after hydrogen exposure*

With decreasing crystallite size, there was an increase in the sensitivity to hydrogen gas when the doped SnO_2 samples were tested at 200°C, Figure 16. Because not all of the samples responded to hydrogen at the lower testing temperatures, and a relationship between crystallite size and hydrogen sensing was desired, the testing temperature was raised until all of the doped samples responded to hydrogen gas. The trend with decreasing crystallite size goes back to the dependence of the magnitude of the space charge layer being dependant on the crystallite size (D) and the space-charge layer

thickness (L). From Figure 16, it is shown that when D < 2L, the sensitivity of doped nanocrystalline SnO_2 is enhanced drastically.
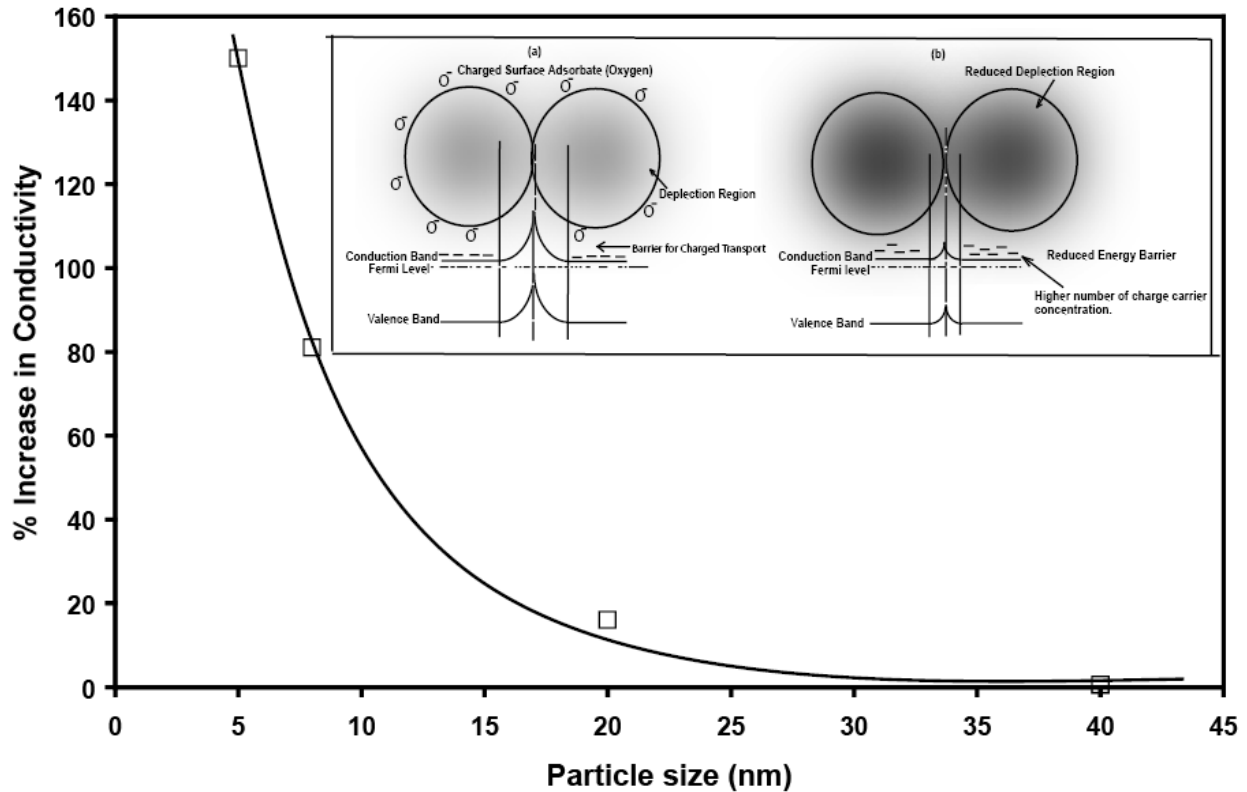
Figure 16: *Increase in sensitivity with decreasing size and schematic of the space charge layer model (inset)*

Impact of sample temperature on the conductivity is shown in Figure 17. The conductivity increased with increasing temperature until a testing temperature of 500˚C where a decrease was observed for all of the 6.5% doped In-SnO_2 samples. This is likely due to the fact that the conduction mechanism around this temperature switches from an extrinsic conduction mechanism to an intrinsic conduction mechanism. The

decrease then would be due to a scattering effect from the two mechanisms, which can be observed from the figure [30]. The first three data points, which were used in order to avoid scattering effects, were used in determination of the activation energy for the lower temperature extrinsic conduction. From the promotion energy, the major charge carrier density was determined for 6.5% In-SnO_2 nanocrystalline samples calcined at 500°C, 600°C, 800°C, and 1000°C. The promotion energies are attributed to the electron transition from the monoionized oxygen vacancies to the conduction band which have been reported to occur between 0.1 and 0.18eV [41]. The calculated energies are 0.129 eV for samples calcined at 500°C, 0.121eV for samples calcined at 600°C, 0.111 eV for samples calcined at 800°C, and 0.094eV for samples calcined at 1000°C. There is a monotonous decrease in the energies as the calcination temperature is increased from 500°C to 1000°C. This is likely due to the location of the bottom of the band gap relative to the shallow donor levels created by the oxygen vacancies. This band bending has been reported by other authors, and is caused by shifts in the Fermi level at different calcination temperatures [6]. It has been suggested that the Fermi level position may also be affected by the presence of uncoordinated surface atoms [10].
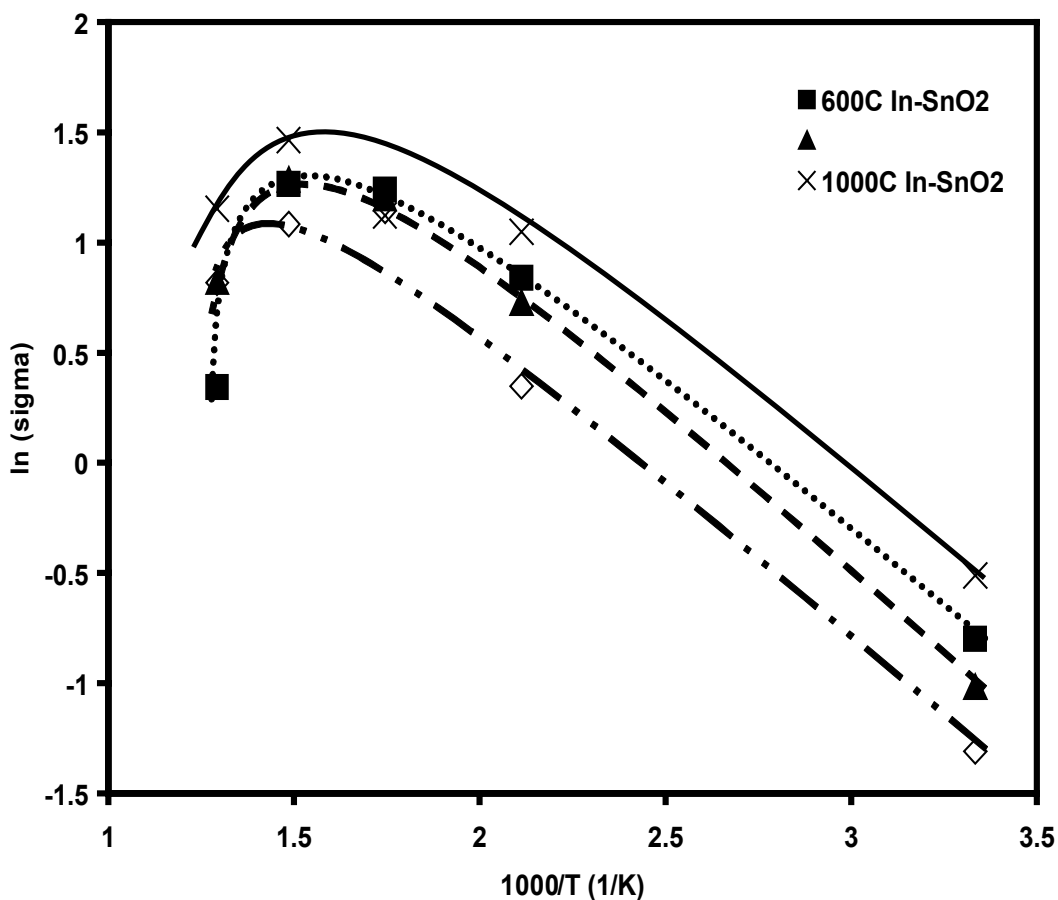
Figure 17: *Conductivity changes with temperature for 6.5% In-SnO₂*

The samples calcined at 500°C (for 3% and 6.5% indium doping) and 600°C (for 6.5% indium doping) showed the largest response to hydrogen gas at room temperature, though both mechanisms between the two different dopings for the sensing of hydrogen gas appears to be different, Figure 18. This result confirms that with decreasing crystallite size, there is an increased sensitivity to hydrogen gas in spite of the bulk conduction mechanism. This increase in response can be explained by the space

charge layer model, Figure 16 (inset). When oxygen molecules are physisorbed onto the surface of nanocrystalline SnO_{2-x}; they receive electrons from SnO_{2-x} and a change occurs to an $O_2^-{}_{ads}$ or $O^-{}_{ads}$ species. Consequently, positive and negative space charge layers can form above and below the surface of SnO_{2-x}. For nanocrystalline SnO_2 particles, a space charge layer of 3nm has been reported [28]. As the grain size, D, approaches twice the depth of the space charge layer, L, sensitivity to hydrogen gas is drastically improved [42]. Twice this space charge layer thickness would correspond to approximately a 6 nm diameter for the maximum desired grain size. This is not far from the 5nm and 9 nm crystallite sizes calculated for the samples calcined at 500°C and 600°C, respectively. It has also been previously calculated that addition of Aluminum (+3) into SnO_2 increases the space charge layer from 3nm to 90 nm. A similar effect may likely also be occurring in this nanocrystalline In-SnO_2 system. In this case, both D and L were modified by controlling the grain size and introducing impurities to modify the surface, as well as the bulk electronic structure, of nanocrystalline SnO_2 [28].
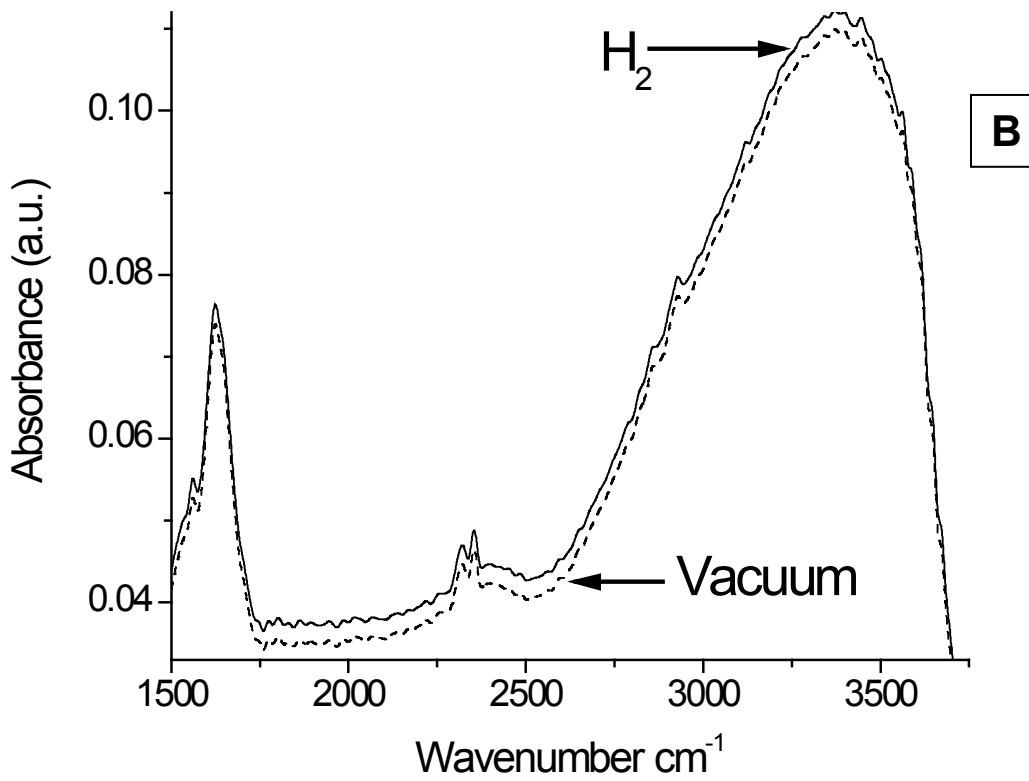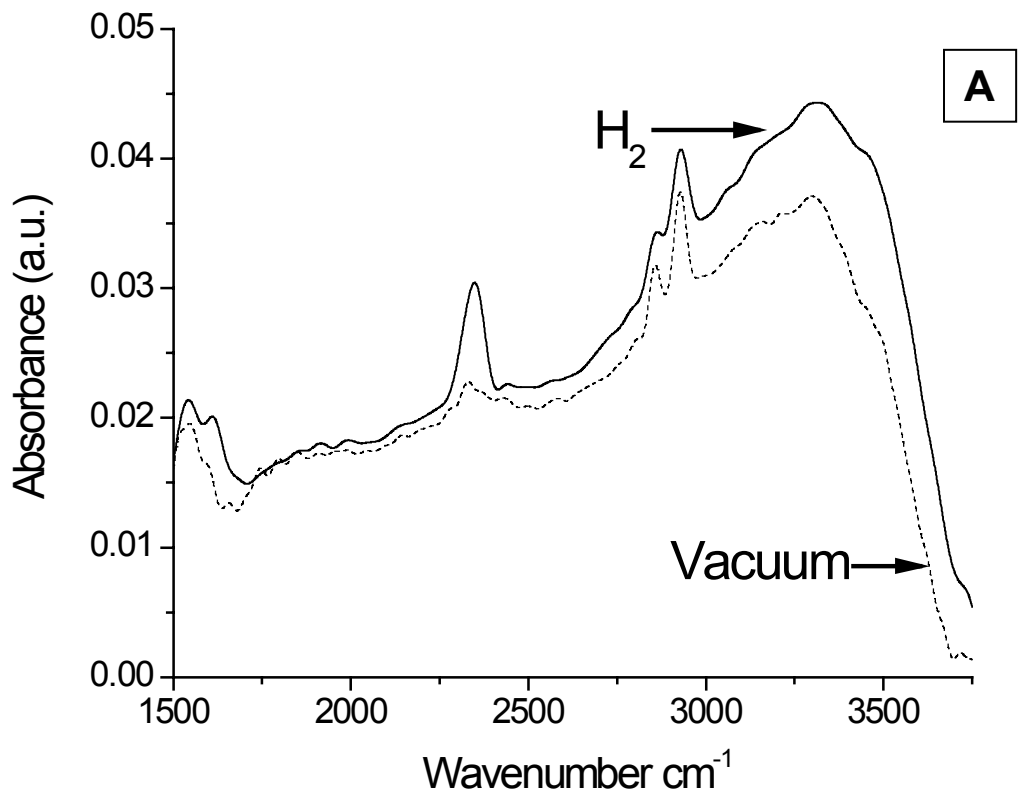
Figure 18: *Absorbance Spectra after hydrogen exposure for A) 3% In-SnO₂ and B) 6.5%In-SnO₂*

By using the relationships given in Equations 6 to 8, major free carrier concentrations were determined for the doped SnO_2 samples. Table 2 shows for the temperatures tested, the In-SnO_2 samples had a relatively constant carrier density of 10^{23} /m^3. It is evident from Table 2 that the magnitude of the carrier density remained fairly constant. This indicates that conduction was indeed extrinsic even at the lower testing temperatures. This is very significant to low temperature gas sensor applications. One of the possible ways to achieve low temperature gas sensing is to have higher oxygen vacancy concentrations retained even at low temperatures. If the actual magnitude of the free carrier density does not reduce drastically with a reduction in temperature, than a non- equilibrium concentration of these oxygen vacancies have been achieved. The term non-equilibrium is used here because normally, the defect concentration would follow an Arrhenius type function with temperature. This means a high oxygen vacancy concentration can be maintained even at lower temperatures with this material system. This makes nanocrystalline In-SnO_2 a strong candidate for room temperature gas sensors.

The calculated free carrier density is slightly lower than what has been reported for nanocrystalline SnO_2. Normally the values are reported in the range of 10^{25}-10^{26}/m^3. Lower carrier density may be due to a grain boundary effect similar to that reported by Gerhardt and Nowick for doped ceria [43]. A likely place for the undoped indium atoms to be located is at the grain boundaries or dispersed around the SnO_2 particles. If this is the scenario, conduction would be more inhibited at the grain boundaries only. Also,

doping may have caused some of the dopants to pair with an oppositely charged oxygen vacancy, hindering the charge movement further. Another likely possibility is that these carrier density numbers reflect a characteristic of the space charge layer or the depleted region. These charge carriers held to a region near the surface by the potential well of a space charge region may have their mobility reduced by surface scattering [44]. This would change the value of the mean free path of the carriers which would explain the discrepancy between the reported values and our calculated data. These charge carriers, even with their reduced mobility, will still be significant at the nano-scale for gas sensor applications.

Table 2: Oxygen Vacancy Concentrations for 6.5% In-SnO$_2$

		Sample Name (ITO)			
Measured Temperature (K)	Calcination T ^{o}C	500 ^{o}C	600 ^{o}C	800 ^{o}C	1000 ^{o}C
473.15		1.64	4.37	3.50	6.64
573.15	Vacancy Concentration 10^{23} (1\m^3)	6.64	8.00	7.44	6.36
673.15		5.01	7.21	7.50	10.8
773.15		9.94	9.94	2.59	5.03

Trivalent indium substitution into the nanocrystalline SnO_2 lattice structure has proven to be an excellent gas sensor material at low operating temperatures. FTIR has shown the ability to calculate both the gas sensitivity and the electronic properties of nanocrystalline In-SnO_2 as a function of temperature. The ability to monitor the impact and the effects of the space charge region with gas sensitivity as well as dopant amounts will allow for better engineering of nanomaterials for low temperature gas sensors. The controlling factors for enhanced gas sensing abilities determined from FTIR at lower temperatures are extrinsic free carrier densities and the nanoparticle size in relation to its Debye length.

All of the doped SnO_2 nanocrystalline samples were also tested for sensitivity to the presence of CO_2 gas. The doped SnO_2 samples were unable to detect the CO_2 gas from the stance of a resistance based sensor. From the absorbance spectra, Figure 19, one is able to identify that CO_2 was in fact present on the surface of the material by observation of the peak at around $2300cm^{-1}$. For all SnO_2 samples, these peaks grew with exposure to CO_2 gas. This indicates that even though the gas was present on the surface of the material, it had no electronic or chemical interactions with the material. This means that in the presence of this gas, nanocrystalline In-SnO_2 based gas sensors will not see a change in resistance.
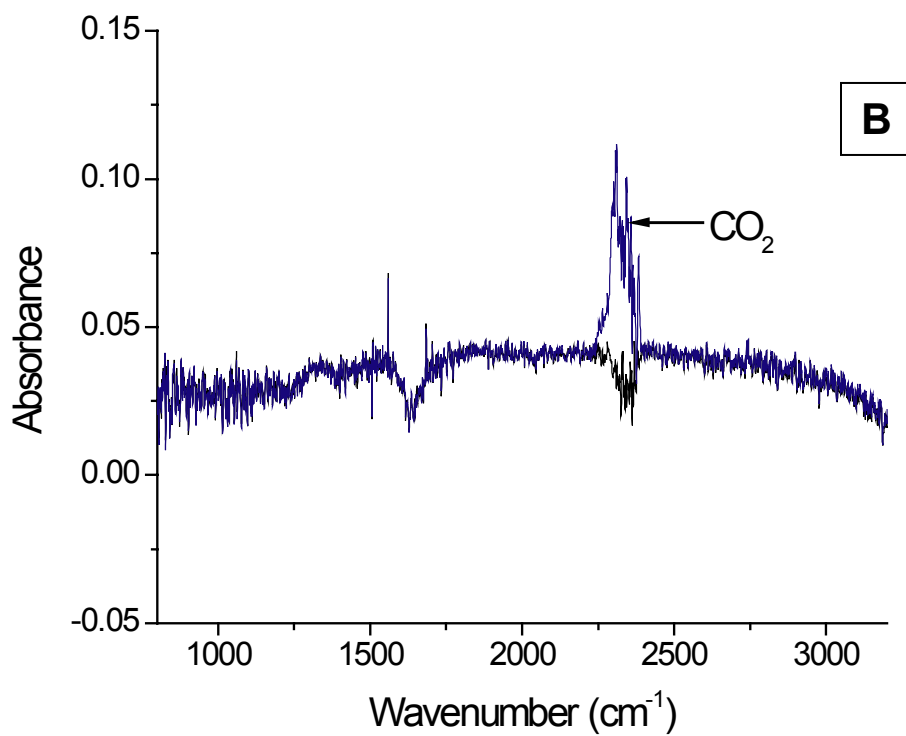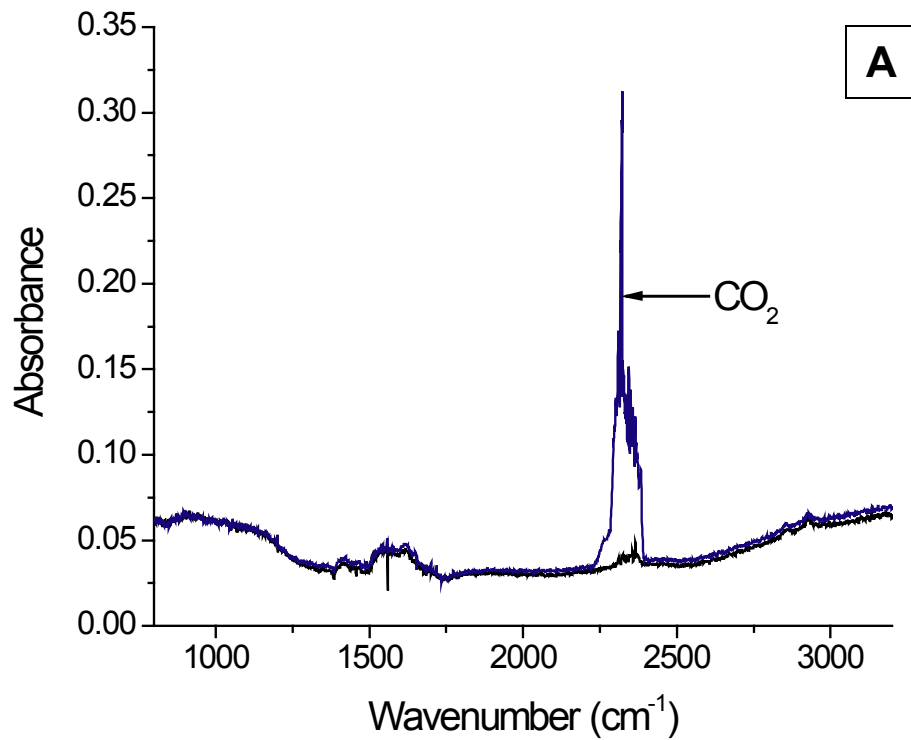
Figure 19: *Absorbance spectra before and after exposure to CO_2 of A) 6.5% In-SnO_2 calcined at 500°C, and B) 6.5% In-SnO_2 calcined at 800°C*

By inspection of the absorbance spectra of the two samples shown in Figure 19, it becomes obvious that the amount of CO_2 adsorbed onto the surface of the two samples is different. The sample calcined at 500°C showed a much stronger absorption peak for CO_2 than did the sample calcined at 800°C. This seems to indicate once again a difference in the nature of the surface oxygen species between the same doped samples (6.5%) calcined at different temperatures. Difference in reconstruction at the surface between surface oxygens and differences in the coordination of the surface oxygen atoms likely are responsible for the differences in this adsorption behavior. This is another useful evaluation that is made possible with the use of FTIR when prescreening materials for gas sensor applications.

4.4 Hydrogen testing of one dimensional SnO_2

Sensitivity to hydrogen gas was also tested on the SnO_2 nanorods obtained by hydrothermal synthesis. Samples were prepared and tested in the same manner as the doped SnO_2 sample for testing in the FTIR. After 30 minutes of exposure to hydrogen gas at room temperature, the SnO_2 nanorods were unable to detect the hydrogen that had been introduced into the chamber. The absorbance spectrum of the nanorods is shown in Figure 20.
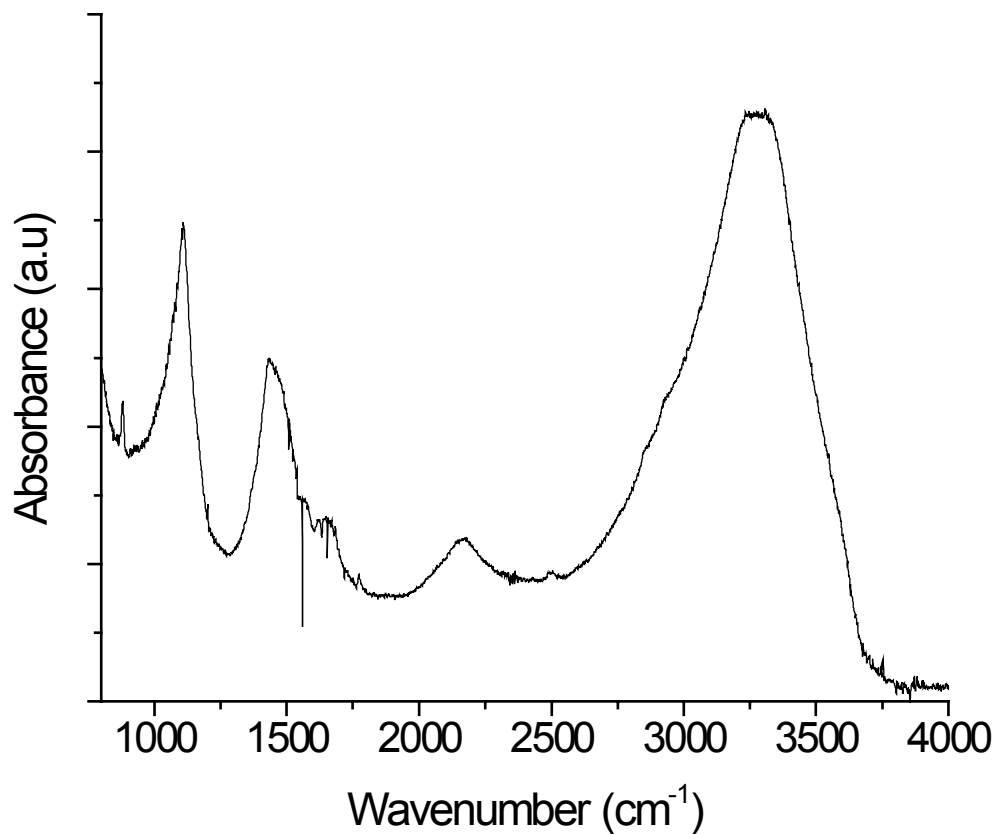
Figure 20: *FTIR absorbance spectra of SnO$_2$ nanorods under vacuum at room temperature*

One interesting aspect about the spectra of these SnO$_2$ nanorods is the fact that many of the same peak features are present that appear for the doped SnO$_2$ samples. Unlike the doped SnO$_2$ samples, the nanorod peaks are much more pronounced and symmetrical. This could be attributed to the higher degree of order on the surface of the SnO$_2$ nanorods compared to that of the nanoparticles. This higher degree of order comes from the preparation methods for the nanorods versus that for the nanoparticles,

as well as by virtue of the nature of the one dimensional structure. The stoichiometry of the nanorods is likely well maintained. This could explain the lack of detection of hydrogen gas by the SnO_2 nanorods. Because room temperature detection of hydrogen gas is desired, a lower activation energy for the surface reaction which recognizes the hydrogen molecules is needed. It is likely that a lack of specific types (in terms of coordination number and reconstruction) of surface oxygen species on the SnO_2 nanorods accounts for its lack in hydrogen detection. Hydrogen detection may become possible with proper doping of the SnO_2 nanorods that maintain the one dimensional nanostructure.

4.5 Recovery with Ceria doping

Ceria, due to its multi-valence abilities, is a good candidate for recovery aspects of the gas sensor material. [45] In a low or oxygen free environment, cerium's ability to go between a +4 and +3 state should allow it to release oxygen to the SnO_2 lattice for quicker recovery after hydrogen removal. This recovery mechanism is driven by the recovery of the sensor material's resistance upon reintroduction of oxygen species into the crystal lattice. The crystal structure of ceria with and without oxygen vacancies is shown in Figure 21.
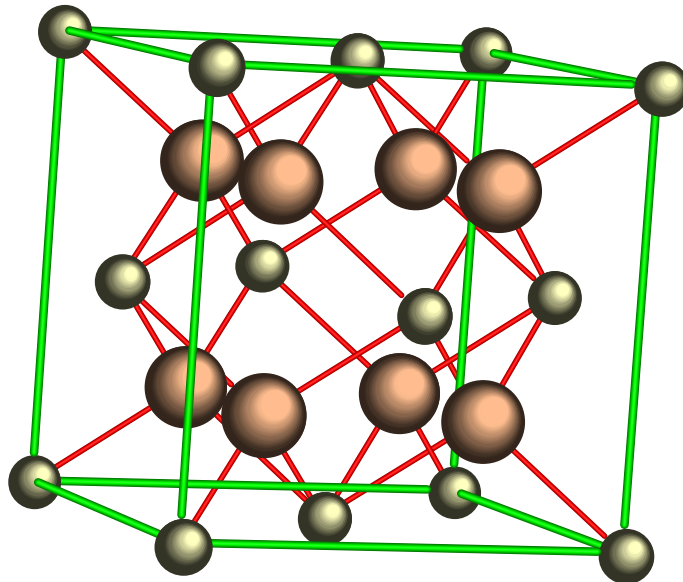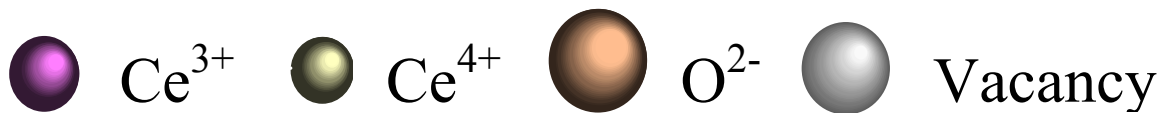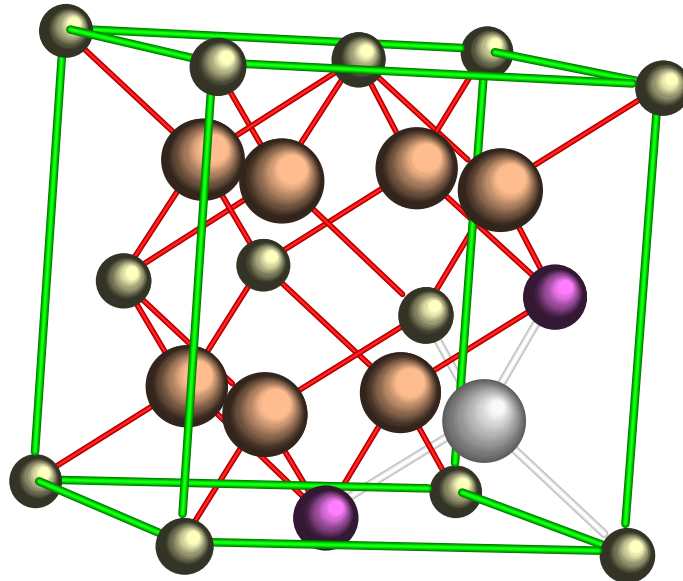
Figure 21: A) *Crystal structure of ceria and B) ceria with oxygen vacant sites due to change of one Ce4+ to Ce 3+*

Cerium nitrate was dried in air and incorporated into the solution for In-SnO_2 before the gelling reaction was allowed to take place. The rest of the synthesis followed as was described in section 2.4. Samples calcined at 500°C, 600°C, and 800°C were tested in air for hydrogen sensitivity and showed no recovery after 30 minutes. Samples calcined at 1000°C were also tested in air for sensitivity to hydrogen and showed a 95% recovery across the broad background within one minute of hydrogen removal, Figure 22a. Non ceria doped In- SnO_2 calcined at the same temperature for one hour showed no recovery even after 30 minutes of hydrogen removal, Figure 22b. In fact, after removal of hydrogen, the absorbance spectra continued to slowly increase. It may be that surface adsorbed hydrogen species continue to dissociate with time, continuing the gas sensor behavior of the material.
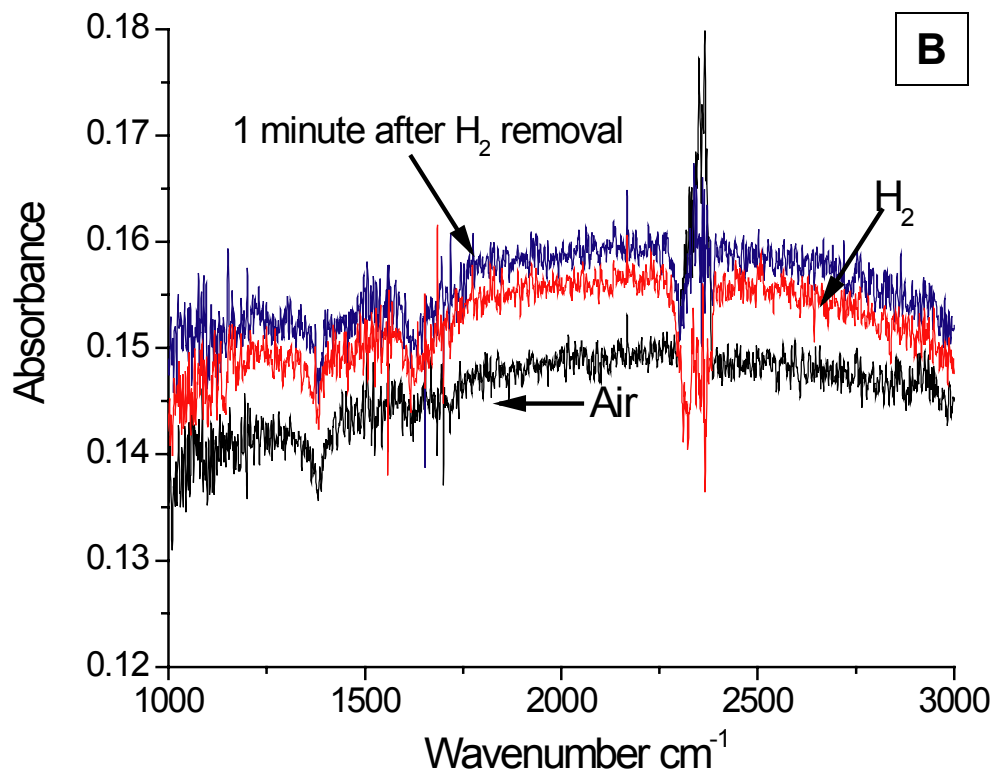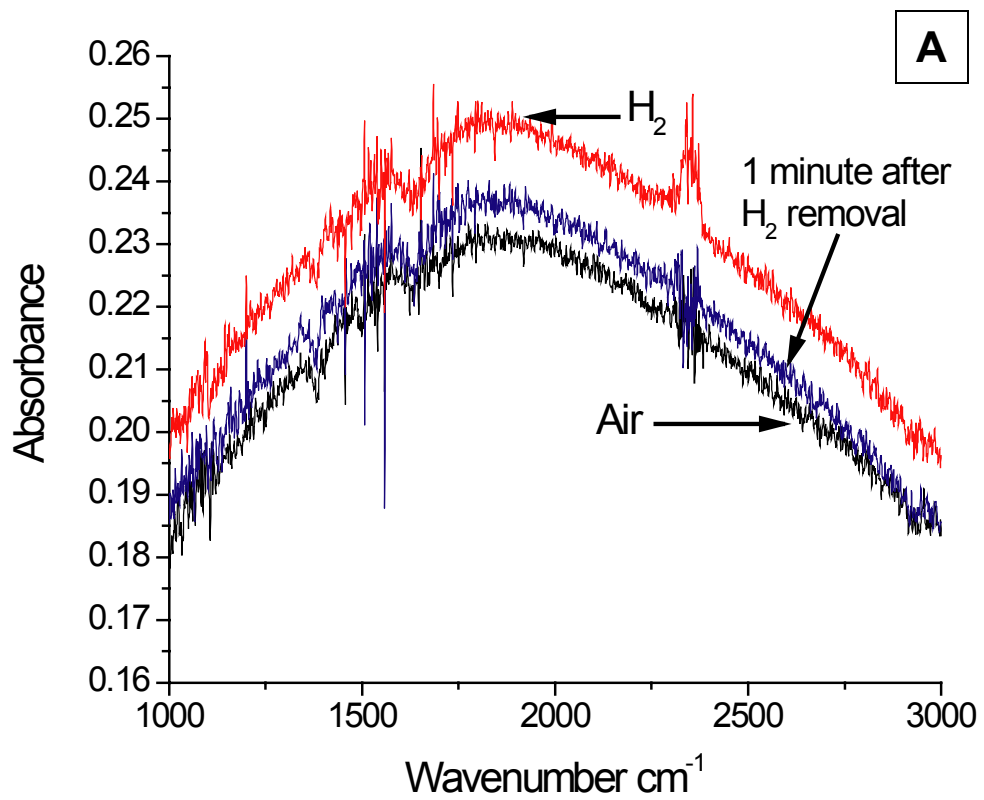
Figure 22: *A) Recovery of Ceria doped In-SnO₂ calcined at 1000°C, tested in air for sensitivity to hydrogen, B) non ceria doped In-SnO₂*

The case for recovery was the same for Ceria doped nanocrystalline In-SnO$_2$ samples tested in vacuum for hydrogen sensitivity and recovery. Only the sample calcined at 1000°C was sensitive to hydrogen under vacuum. Similar samples calcined at the other temperatures showed no response to hydrogen. The sample calcined at 1000°C was also better able to recover from hydrogen exposure after removal of the target gas as it was in the case where the same sample was tested in air, Figure 23.
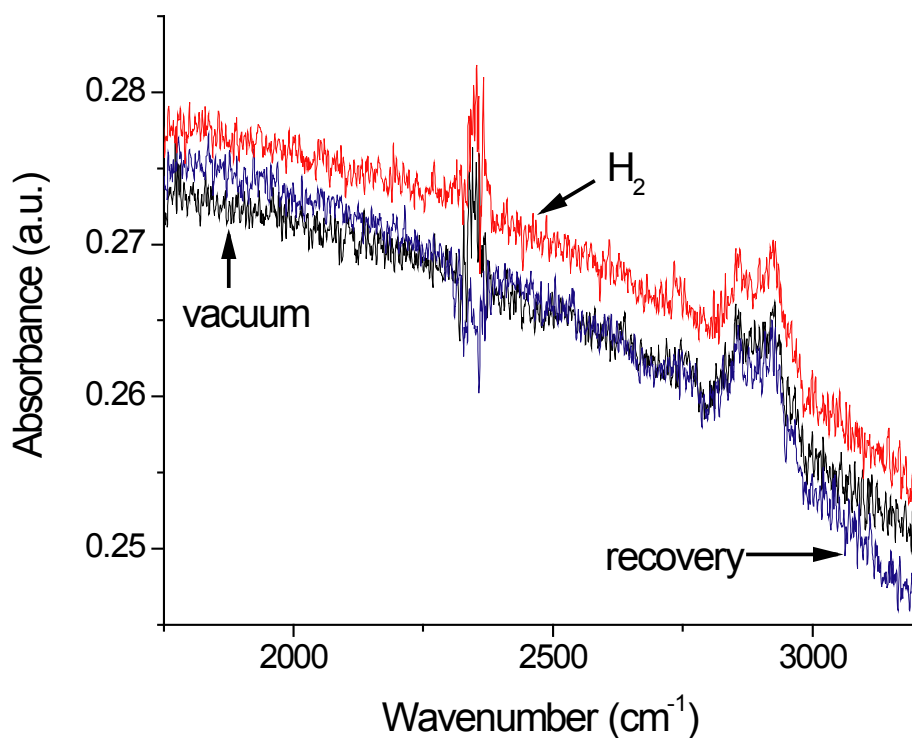
Figure 23: *Recovery of Ce, In-SnO$_2$ (calcined at 1000°C) and tested in vacuum for hydrogen sensitivity*

These recovery findings are of interest since the In-SnO$_2$ samples calcined at 500°C tend to have the better responses to hydrogen gas when no ceria is involved. This discrepancy in recovery between the two different calcination temperatures (500°C versus 1000°C) may be due to the form and bonding cerium takes within or outside of the SnO$_2$ lattice. The XRD graphs between the two samples give strong indication of this. Possibly, a separate phase of ceria is needed in order to take full advantage of the oxygen release abilities. Doping of cerium on a tin site within the lattice may not have the correct effect since those oxygens, though bonded with a cerium atom, are still coordinated by other tin atoms. That would mean that those oxygens, though in close proximity to a cerium atom, would still feel the attractive forces of the other neighboring tin atoms. This would mean that those oxygens near cerium atoms would still feel that they belonged to SnO$_2$. Also, with cerium in the tin oxide matrix, release of an oxygen into the same matrix may not be useful. The concentration of oxygen within the material will not have changed in this scenario.

In Figure 24 it is observed that the same surface species are present on the sample calcined at 500°C as those that are on the 1000°C sample (Figure 23). This would indicate that the lack of hydrogen sensing from the sample is solely due to the incorporation of cerium into the SnO$_2$ lattice. Due to the large size of the cerium atom in comparison to a tin or indium atom, if it is truly doped at the lower calcination temperatures, the cerium atom would strain the crystal lattice. This would make it much more difficult for charged species to move and would hinder low temperature gas sensing of the material.
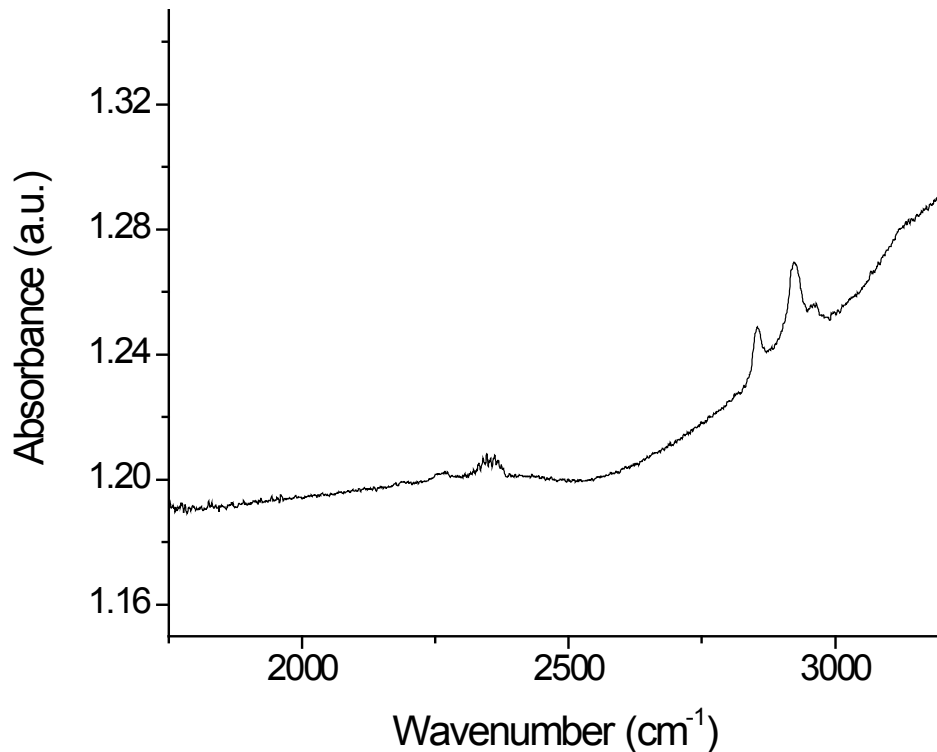
Figure 24: *Ceria doped In-SnO$_2$ calcined at 500°C, tested in vacuum*

A type of nanocomposite may be appropriate in this situation, if ceria is to be incorporated for recovery aspects of a gas sensor. The large difference between the samples calcined at 500°C versus 1000°C is the amount of ceria that may have separated out of the SnO$_2$ structure. In the case of the sample calcined at 1000°C, the ceria is likely on the surface of the grains or particles, but still in good chemical contact with the In-SnO$_2$ particle. The best scenario for improving recovery of nanocrystalline In-SnO$_2$ would be islands or clusters of ceria on the outside of the grains whose lattice is

at least semi-coherent with that of the host matrix. This would improve the pathway for oxygen atoms to move from the ceria on the surface into the bulk of the In- SnO_2 particles but would still leave a sufficient amount of the SnO_2 surface exposed. Care to not introduce stress between the two materials would also be important in order to not hinder the mobility of the oxygen atoms.

CHAPTER FIVE: THERMODYNAMICS OF DOPING NANOCRYSTALLINE SnO$_2$

5.1 Background

In ceramic materials, doping typically occurs by substitution of the host atom in the crystal lattice or by the atom going into interstitial positions in the crystal lattice between the host atoms, Figure 25. Several factors play into which of the two will occur for doping, such as atomic size, atomic charge, and the type of crystal structure the host possesses. Interstitial doping occurs commonly in the case where carbon is doped into the iron matrix in order to harden the material. In this case, carbon is much smaller than iron. Substitutional doping often occurs when the dopant is comparable in size and electronegativity to the host atom. An example is when silicon is doped with phosphorous, a common practice in the semiconductor industry.

Doping can include such changes to the host structure as an increase in strength, changes in fracture toughness, and changes to the electronic structure, which can also affect the optical properties of the material. A strong relationship between the sintering process and the electrical conductivity has been reported in the literature and should always be considered at the nano-scale. [46] This chapter will focus mainly on how doping affects the electrical properties of SnO$_2$ and will make a correlation between these effects and gas sensor applications.
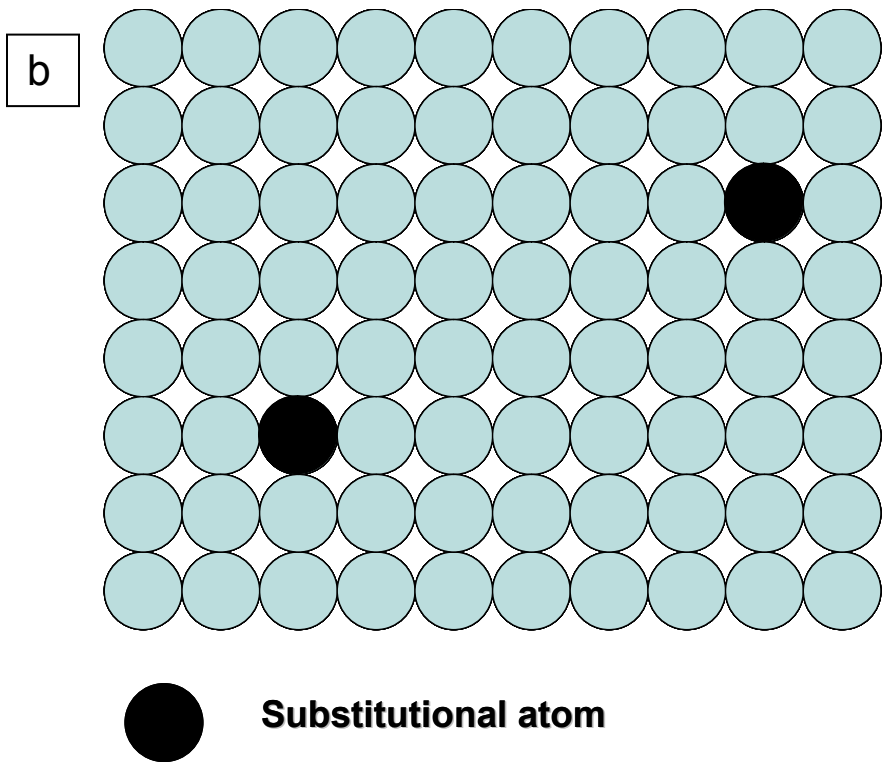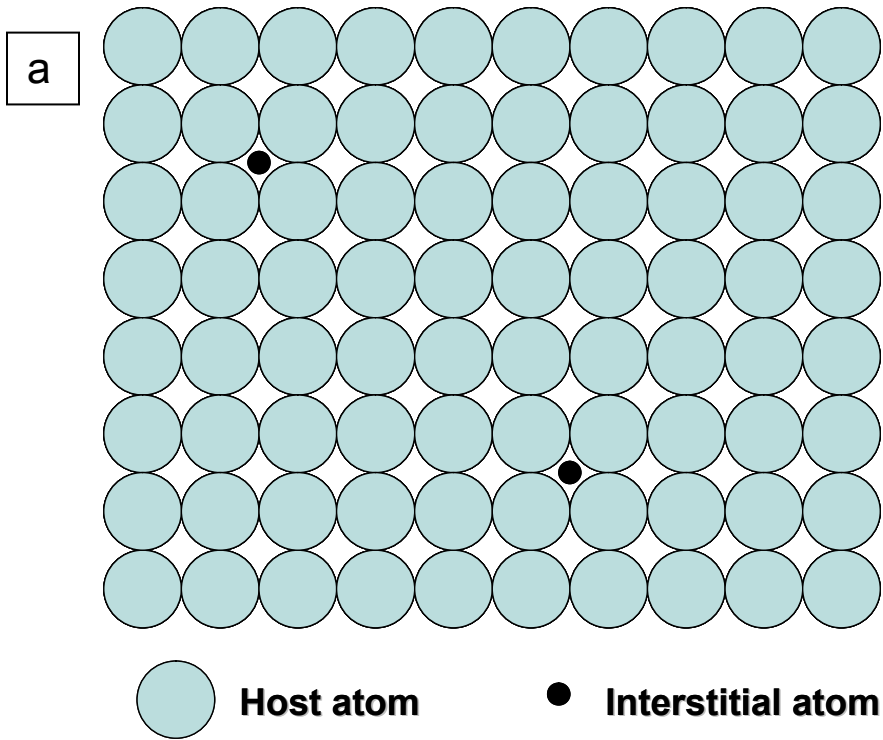
Figure 25: *a) Interstitial and b) substitutional doping in a ceramic*

Doping of ceramics can have formative changes to the structure. These effects show up in the form changes of the activation energy for particle growth and the mechanism(s) by which the material actually forms by. This may make low temperature defect concentrations higher or lower than what would be normally expected, especially in nanomaterials. These changes can be brought about by solute drag, segregation of dopants to the grain boundaries, and local stresses induced by having the dopant present into the crystal lattice.

5.2 Activation Energy for Growth of nanocrystalline In-SnO$_2$

The term *grain growth* describes an increase in the grain size of a single phase solid or in the matrix grain size of a solid containing second phase particles. [47] This growth is usually occurs at high temperatures, depending on the material. The growth of grains is important in Materials Science and even more important when dealing with nanomaterials. This is because the final structure that is present is largely dependant on how the grains came about in the first place. Understanding of the mechanisms at play during the formative stages of a grain will help in shaping the final properties of the material.

An activation energy for growth accompanies grain growth since it is a temperature dependant process. This activation energy generally describes the minimum energy

required to activate and sustain material transport during the growth of the grains. [22] It is therefore useful in understanding the changes in this activation energy upon doping with indium in order to understand the chemical and electronic properties of the final structure.

FTIR was used to help understand the role of doping in nanocrystalline SnO_2 in terms of surface species and impact on hydrogen gas sensing performance. The effect of calcination temperature on the particle size evolution, substitution of the indium atoms into the SnO_2 matrix, corresponding change in free carrier concentration, and variations in the space charge layer of the nanocrystalline SnO_2 were investigated using insitu FTIR.

A plot of ln(D) (where D is the average crystallite size) versus inverse temperature was used to determine the activation energy for particle growth. For plain sol-gel derived SnO_2, an activation energy of 28 kJ/mol was determined, Figure 26a. Santinelli et al. reported an activation energy of 22 kJ/mol for SnO_2 xerogel. [48] This value of 28 kJ/mol is close to other values reported in the literature.

For samples doped with 1% and 3% indium, the activation energies dropped to 19.3 and 20 kJ/mol, respectively (Figure 26b and 26c). This drop in energy may be associated with an increase in oxygen vacancies created upon indium doping into the SnO_2 lattice. Starting materials (pre-calcination) for nanocrystalline materials tend to be extremely structurally disordered. This has been attributed [49] to oxygen vacancies as well as disordered interfaces. It has been suggested [50] that the low activation energy

of nanocrystalline materials may be due to the large percent of highly disordered interfaces. Doping likely increases this disorder, as well as creating more oxygen vacancies for material transport during material synthesis. Though solute drag is usually expected at low doping concentrations, high disorder and oxygen vacancy concentrations likely out weigh this effect at very small grain sizes. This would explain the lower activation energies experienced by samples doped at 1% and 3% indium.

A

$E_a=28.0kJ/mol$
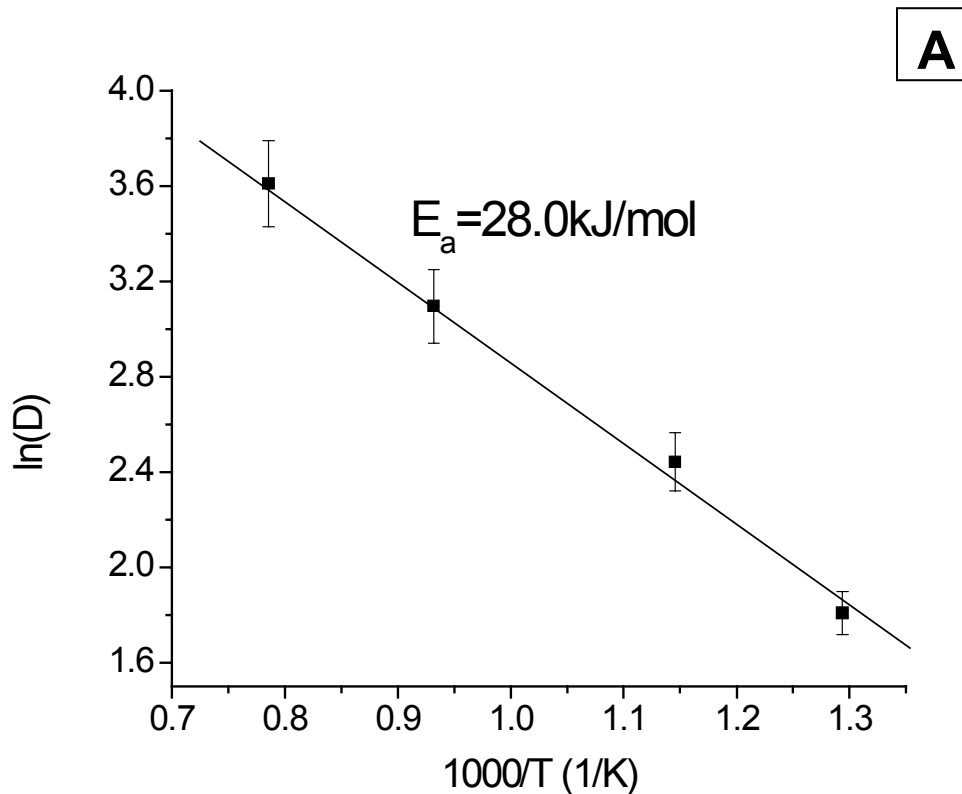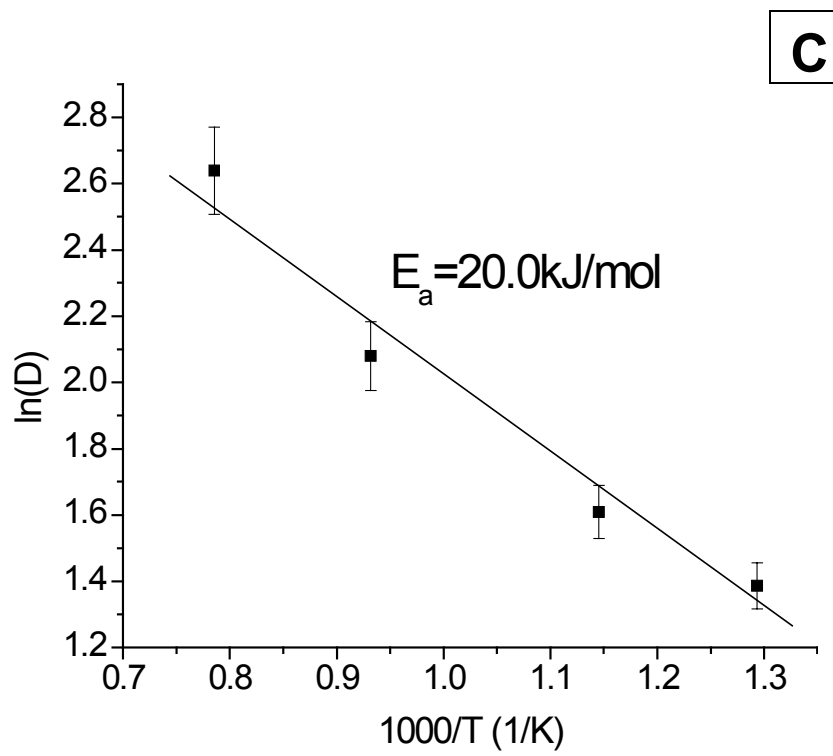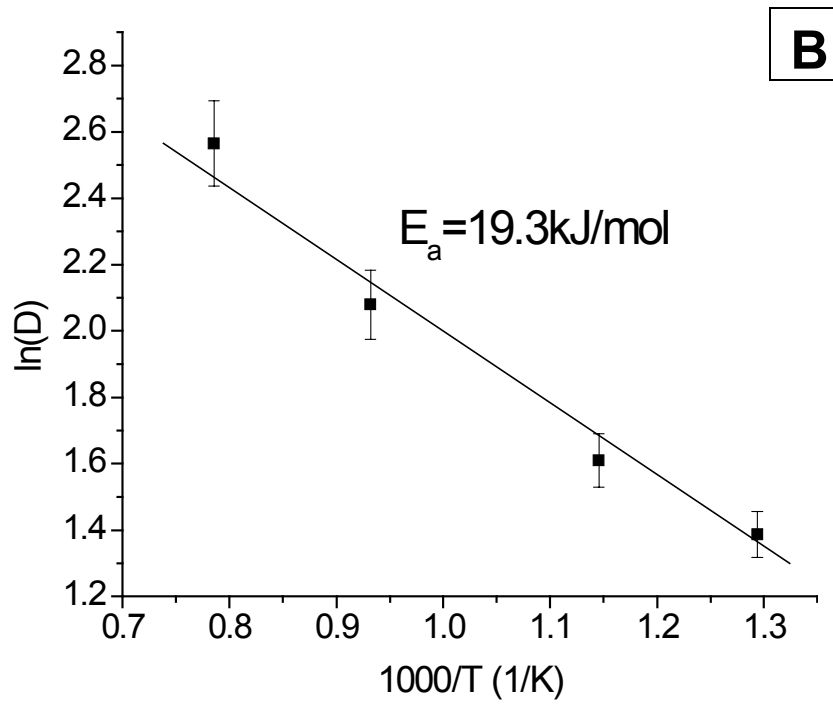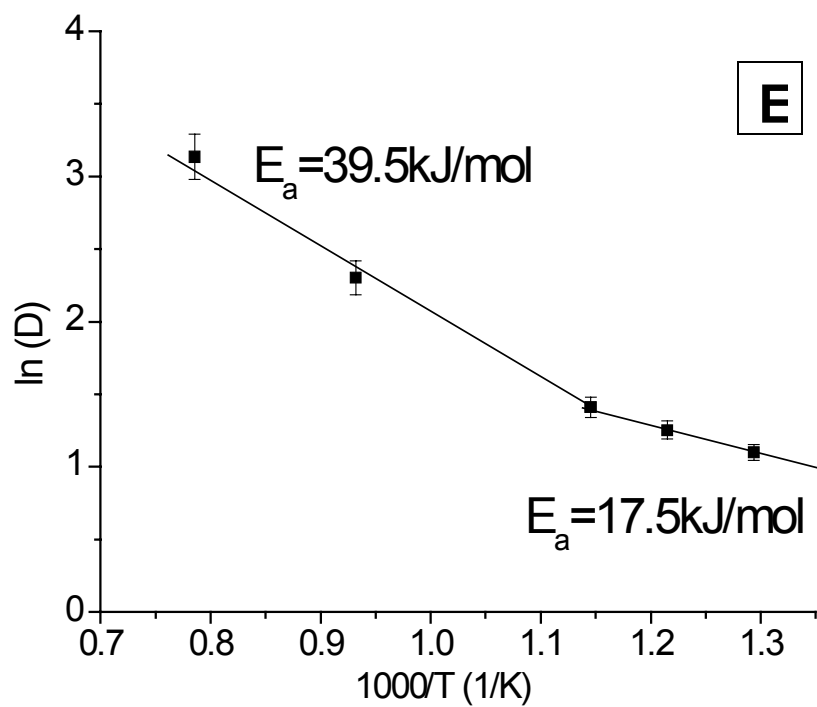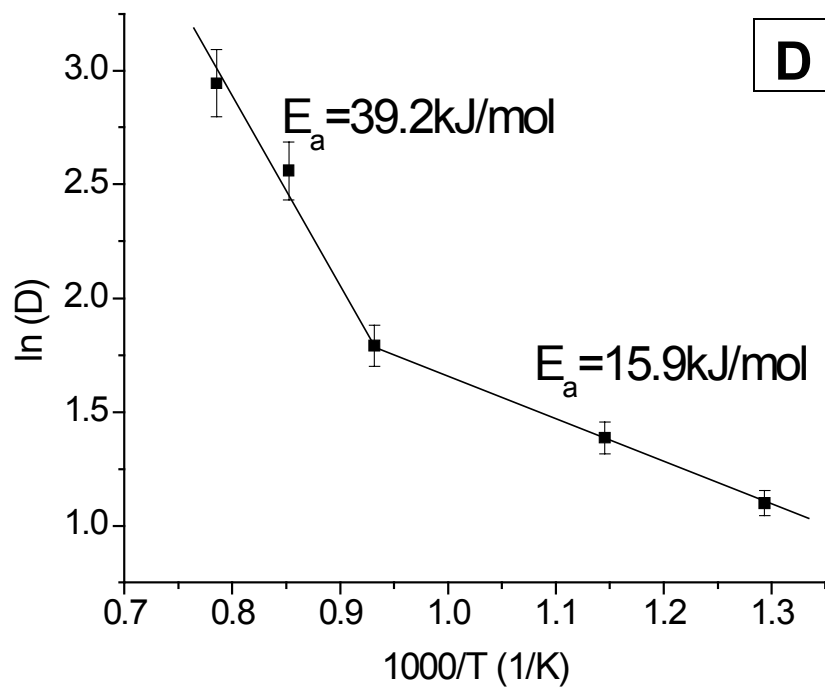
Figure 26: *Plot of Ln (D) versus 1000/T for A) SnO$_2$, B) 1% In-SnO$_2$, C) 3% In-SnO$_2$, D) 6.5 %In-SnO$_2$, E) 9% In-SnO$_2$*

For SnO_2 samples doped at 6.5% and 9%, two different activation energies appear to be present, Figure 26d and 26e. For the 6.5 % doped samples, an activation energy of 15.9 kJ/mol occurs for the lower calcining temperatures, while at higher temperatures, the activation energy increases to 39.2 kJ/mol. This appears again with the 9% doped samples, with a lower activation energy of 17.5 kJ/mol at the lower calcination temperatures and a higher activation energy of 39.5 kJ/mol at higher calcination temperatures. This is likely due to the segregation of indium out of the SnO_2 lattice structure (around a calcining temperature of 800°C) and into the grain boundaries. XRD plots are in agreement (Figure 6) and give evidence of this phenomenon with increasing doping concentration as well as calcination temperature. The lower initial energies may be attributed to the structural disorder caused by the indium doping into the SnO_2 lattice as previously stated. At higher calcination temperatures, higher diffusion rates coupled with desorption of surface species (H_2O, OH^-, and CO_2) may lead to segregation of indium to the grain boundaries and particle surface, consequently leading to the formation of amorphous In_2O_3. This would account for the higher activation energies at the higher calcination temperatures due to a grain boundary barrier inhibiting mass transport, and therefore, increasing the energy required for material movement during particle growth.

5.3 Growth exponents of In-SnO$_2$

Grain growth in polycrystalline solids is a time dependant process and is driven by the surface energies of the grains. A mechanism for material transport must be present in order for there to be any growth of the grains, or even particles. [23] This section deals with the mechanism of grain growth in nanocrystalline In-SnO$_2$ and its effects on the gas sensor behavior of the material.

It has been documented that the mass transport mechanism at temperatures below 1000° C for the SnO$_2$ system is due to surface diffusion during particle or grain growth. [48, 49] Because this mass transport mechanism is sensitive to surface contamination, formation of In$_2$O$_3$ at the surface of grains would account for the change to higher activation energies for growth at the higher calcination temperatures. Leite and coworkers [51] attributed higher growth exponents to surface contamination, or chemical species bonded to the powder surface. A similar scenario is at play for these In-SnO$_2$ nanoparticles.

To give more insight to the mass transport mechanism of the In-SnO$_2$ nanoparticles, samples doped at 6.5% were calcined at 30 minutes, 1, 3, 5, and 7 hours to obtain the grain growth kinetics. Generally, grain growth follows:

$$G^n = G_o^n + Kt \quad \ldots\ldots\ldots\ldots\ldots\ldots\ldots\ldots\ldots\ldots\ldots\ldots\ldots\ldots\ldots\ldots(5.1)$$

In Equation (5.1), G_o is the initial average grain size, G is the average grain size at time t, and K is a constant. The constant K is temperature dependant and is associated with an activation energy component. The grain growth exponent, n, describes the mechanism for grain growth (or the grain growth kinetics). Generally, n lies in the range of 2 to 4, and in many ceramics, n equal to 3 have been observed. [46] In nanocrystalline materials, many different values of n have been reported. Large grain growth exponents and low activation energies are commonly reported for nanocrystalline ceramic materials.

A plot of ln(G) versus ln(t) was analyzed to solve for the growth exponent n, Figure 27. It can be seen that with increasing calcination temperature, the curves shift up, with the 500° C samples at the bottom and the 1000° C samples at the top of the figure. The samples calcined at 600°, 800°, and 1000° C have similar slopes while the 500° C samples had a slightly different slope. The calculated values of the growth exponent were n = 2.6 for the 500° C samples, n = 4.2 for the 600° C samples, n = 4.7 for the 800° C samples, and n = 4.4 for the samples calcined at 1000° C.
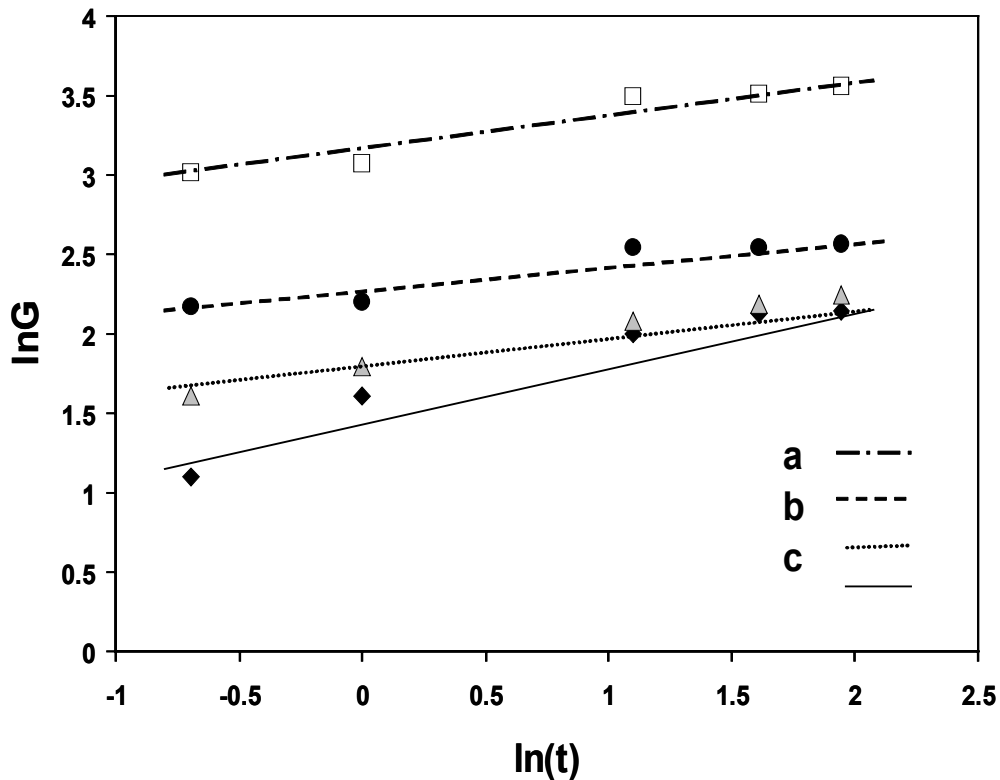
Figure 27: *Growth exponents from plots of lnG vs ln(t)*

Growth exponents in nanocrystalline systems are often reported at 4 or higher, especially in the SnO_2 system. [49, 50] The 600°, 800°, and 1000° C samples seem to follow this trend and grow by the same mechanism. For the samples calcined at 500° C, the value of n = 2.6 seems to indicate a mixed mechanism. For n = 2, normal grain growth is occurring in a pure, single phase system. For n = 3, grain growth is occurring in the presence of solutes. [50] This could be the case for the samples calcined at 500° C, solutes hindering growth in a single phase system. For the other 3 calcination temperatures, the growth mechanism can be attributed to growth in the presence of

75

solutes. [52] This would explain, from XRD, the changes in activation energy with increasing calcination temperature. As calcination temperature was increased at the higher doping amounts of 6.5 and 9%, the activation energy for growth was increased. This would align with indium segregating to the surface or grain boundaries by a surface diffusing mechanism. Combined, the different activation energies and growth exponents lead to explanations of the different gas sensing behavior between the different dopings and different calcination temperatures. The variation in gas sensing will be impacted by the surface structure of the SnO_2 grains based on synthesis of the material. By changing the amount of doping in the SnO_2 system, changes in the way the grains form and subsequently grow will affect the type of final surface structure achieved. This allows for engineering of the surface more precisely to gas sensor and other specific applications.

5.4 Impact of Doping on H_2 sensing behavior

All indium doped SnO_2 nanocrystalline samples were tested for sensitivity to hydrogen gas at room temperature (30° C) using the Praying Mantis accessory and the diffuse reflectance mode of the FTIR. It can be observed that there is an upward shift in the absorbance spectra after exposure to hydrogen gas if the material is able to detect the gas.

When exposed to air, oxygen molecules are physisorbed onto the surface of nanocrystalline SnO_{2-x} and take free electrons from SnO_{2-x}. A change then occurs to $O_2^-{}_{ads}$ or $O^-{}_{ads}$ species on the surface. When a reducing gas (such as hydrogen) comes into contact with these nanoparticles, it is oxidized via reaction with the $O_2^-{}_{ads}$ or $O^-{}_{ads}$ surface species. Subsequently, electrons are reintroduced into the electron depletion layer. The following equations show the surface reactions upon introduction of hydrogen to the SnO_{2-x} surface [6]:

$$H_2 \rightarrow 2H_{(ads)}^+ + 2e^- \dots\dots\dots\dots\dots\dots\dots\dots\dots\dots\dots\dots\dots\dots(5.2)$$

$$O_{(ads)} + e^- \rightarrow O_{(ads)}^- \dots\dots\dots\dots\dots\dots\dots\dots\dots\dots\dots\dots\dots(5.3)$$

$$H_2 + O_{(ads)}^- \rightarrow H_2O_{(ads)} + e^- \dots\dots\dots\dots\dots\dots\dots\dots\dots\dots(5.4)$$
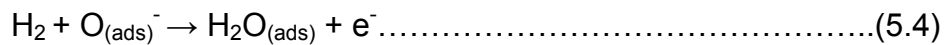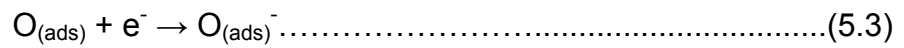
Electrons added to the space charge region of an n-type semiconductor surface will lead to an increase in absorption [53] affecting the broad background of its FTIR spectra. These excess electrons from hydrogen are able to absorb more energy (from the infra-red) for conduction, increasing the amount of absorption. The changes in oxygen vacancy concentration with doping concentration are shown in Figure 28.
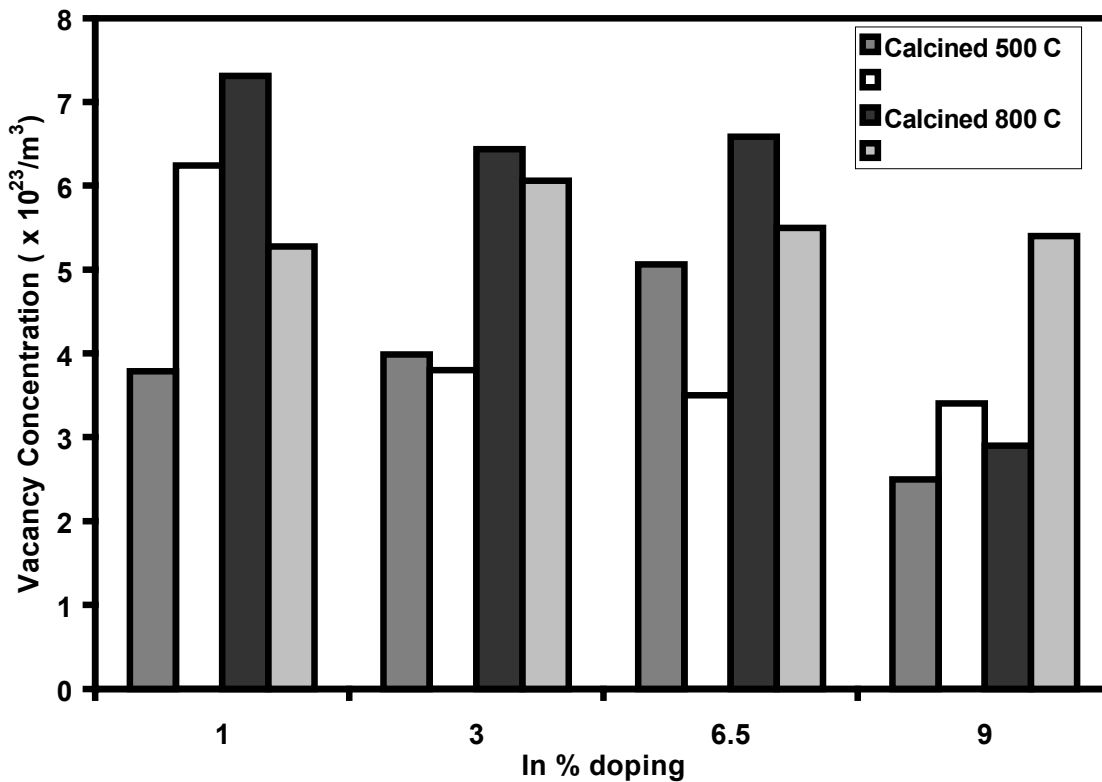
Figure 28: *Changes in oxygen vacancy concentration with indium doping*

All of the nanocrystalline In-SnO$_2$ samples at different dopings were tested for sensitivity to hydrogen gas. Only 3 of the samples showed any appreciable response to H$_2$ gas exposure at room temperature without the help of a catalyst. These were the 6.5 % In-SnO$_2$ samples calcined at 500° and 600° C, as well as the 3% In-SnO$_2$ sample calcined at 500° C. The greatest response to hydrogen gas was from the 3% and 6.5% In- SnO$_2$ samples calcined at 500° C, but by what appears to be by slightly different surface mechanisms, Figures 19a and 19b (page 50). For both samples, an increase in free

carriers, and therefore conductivity, can be seen by the increase in absorbance for the broad background. These are areas where surface vibrations are not affected even after introduction of a detectable gas. Only shifts up and down will be seen for the broad background. For the 3% In-SnO$_2$, the broad peak around 3450 cm^{-1} (due to physisorbed water bending or surface hydration) [54] is altered after H$_2$ exposure; where on the 6.5 % sample surface, water groups are little impacted. Surface CO$_2$ (~2300 cm^{-1}) [55] on the 3% In-SnO$_2$ samples also appear affected after hydrogen exposure while the same surface group on the 6.5% sample goes unaltered. So even though both samples responded to the hydrogen gas with an increase in absorption, it appears that the 3% In-SnO$_2$ sample utilizes surface CO$_2$ and water groups to dissociate, or participate in the dissociation of, adsorbed hydrogen gas. Note that both samples possess the two surface groups, but that the 3% sample appears to have a slightly greater percentage of surface coverage by these species after exposure to hydrogen gas. The approximate area under the curve for these peaks is higher for the 3% sample than for the 6.5% sample. The gas sensing mechanism for the 6.5 % In-SnO$_2$ samples may be due to surface species which are difficult to distinguish using DR-FTIR due to the type of vibrations they posses.

It may be deduced that due to the lower surface coverage of CO$_2$ and adsorbed water, surface oxygens and vacant oxygen positions may be the mechanisms behind the sensing ability of the 6.5% sample calcined at 500°C. Both the 3% and 6.5% samples appear to have been fully doped with indium. It is likely that the substituted tin atoms made their way to the surface of the nanoparticles, but without complete bonding to the

oxygen species. This would have left behind surface oxygen vacancies in the crystal lattice. The vibrations associated with these surface species occur at very low wavenumbers of the FTIR and are associated with an appreciable amount of noise, making it difficult to correctly analyze changes in absorbance. This surface information is useful in the engineering of gas sensor materials to specific applications and environments which may desorb certain surface species required for sensing of a particular gas.

It has been previously reported that the maximum doping of indium into the SnO_2 system is around 3%. [35] In this study, a change in growth activation energy is also observed when comparing 3% and 6.5% indium doped SnO_2 samples. A comparison of the free carrier density in the space charge region versus indium doping at a calcination temperature of 500° C is shown in Figure 29. The 6.5% doped sample calcined at 500° C has the highest free carrier density with the smallest crystallite/grain size. Though this free carrier density is for the space charge region of the material, due to its very small size, it can be assumed that this space charge region occupies most of the grain. Even though thermodynamically, 3% is the solid solution limit of indium into the SnO_2 system, it is possible that at higher doping amounts, certain over dopings can be achieved at relatively short calcination times. This may be due to the high degree of disorder already present in the nanomaterial prior to high temperature calcination. This initial disorder in starting materials for nanocrystalline SnO_2 when synthesizing using a bottom-up approach may allow for higher doping amounts than a more atomically ordered crystal lattice would. At short calcination times, since the growth mechanism is reportedly

dominated by surface diffusion, the structural disorder within the grains remain, allowing for over dopings from the thermodynamically predicted amounts in this nanocrystalline system.
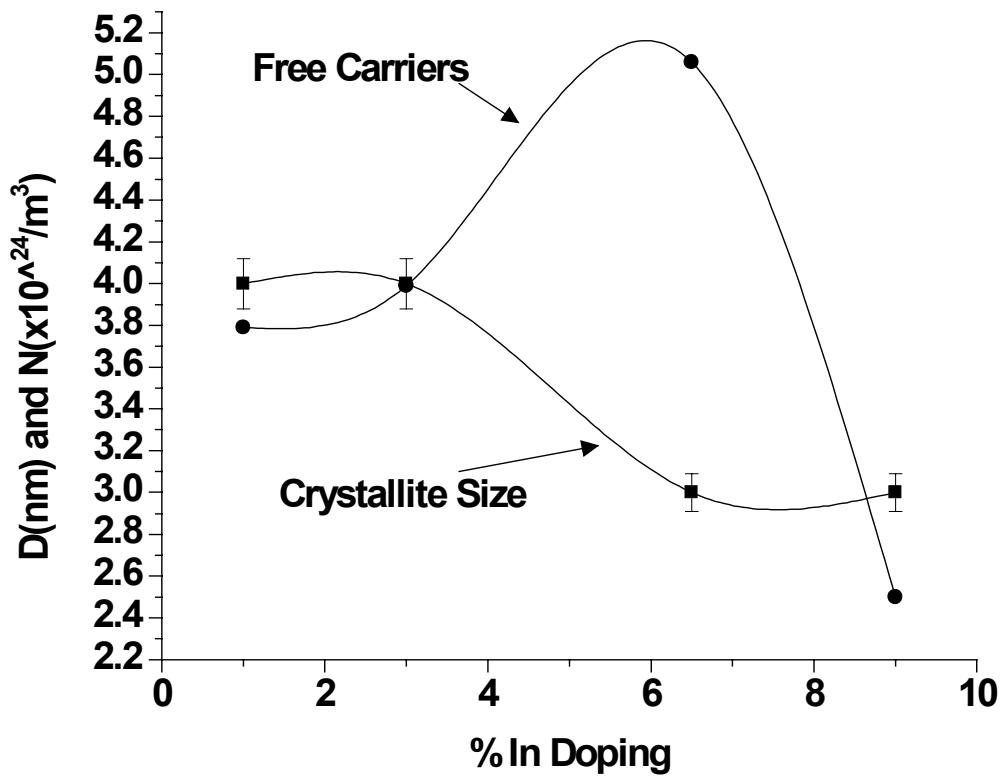
Figure 29: *Free carrier concentration and crystallite size versus indium doping at 500°C calcinations*

These over doping amounts may have the greatest impact on the space charge region of nano-oxides for gas sensor applications where the grains are comparable to the

Debye length of the material. This is due to the creation of, and ability to retain defects above what would be expected for thermodynamically predicted maximum doping amounts for a system in equilibrium. Creation of a larger amount of oxygen vacancies, the charge carriers in the case of nanocrystalline SnO_2, will impact two things. One, the number of surface oxygen vacancies may increase, creating more opportunities for the target gas (in this case hydrogen) to interact with the material. Second, it creates more charge carriers within the material. This gives injected electrons from the surface reaction with hydrogen more opportunities to move about the material. In the case of hydrogen gas sensing at room temperature, maximizing the number of free carriers in the space charge region leads to better sensing of hydrogen gas upon dissociation on the surface.

CHAPTER SIX: ELECTRONIC MODIFICATIONS IN NANOCRYSTALLINE SnO$_2$

6.1 Background

Nanocrystalline SnO$_2$ is an important transparent electronic material. One of the most interesting aspects of SnO$_2$ is that in spite of its wide band gap and transparency, it still possesses good electronic properties. [56] Doping of the SnO$_2$ system has been a point of interest due to the ability to tailor its electrical and microstructural properties. [17, 54, 55-58] In the area of sensors and other electronic applications, tailoring of the electronic structure in nanocrystalline materials has become pivotal. [13, 61, 62]

The ability to change the band gap can come about in certain instances. For example, in nanocrystalline SnO$_2$, at very small sizes (~3nm), increases in the band gap have been reported. [63] Shifts to direct band gap values as high as 4.1 eV have been reported. These changes in the band gap are especially prevalent amongst one dimensional nanostructures. Changes in crystal bonding and lattice constants can also bring about changes since the band gap is dependant on these two factors. [24]

Interband optical absorption is associated with direct transitions if the conduction band minimum and valence band maximum occur at the same wave vector, Figure 30. [64] The absorption coefficient is important in understanding band transitions since it is

related to the transition probability between different states. It can therefore be used to help gather information on the direct optical band gap of a material.
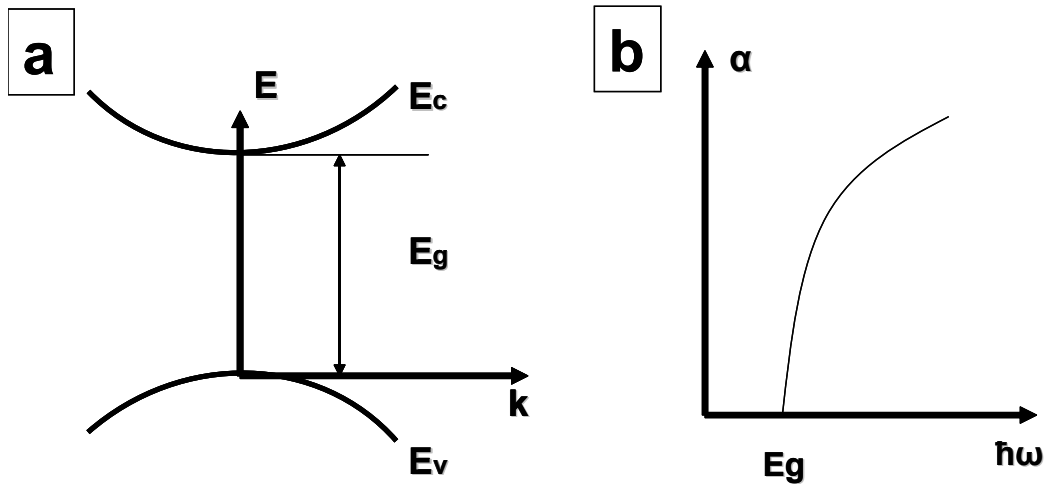
Figure 30: *a) Schematic of energy bands and b) absorption coefficient at band to band transitions [62]*

In some semiconductors, interband transitions do not occur between the band extrema. [24] In this case, there may be an indirect transition between the valence and conduction band. These indirect transitions are much weaker than direct transitions since they are second order processes. [64] Indirect transitions appear when the conduction and valence bands have their extrema points localized in different directions in k space. In an indirect gap, two transitions take place, Figure 31. The first is a vertical

transition due to the electron-radiation interaction. The second is a non-vertical transaction due to the electron phonon interaction.
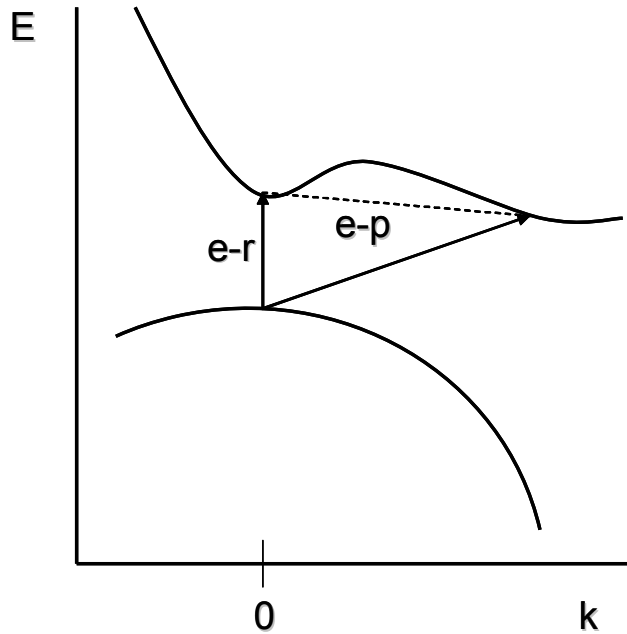
Figure 31: *Vertical and nonvertical transitions in crossing an indirect gap [22]*

6.2 Band gap determinations for nanocrystalline SnO$_2$

SnO$_2$ is a wide band gap semiconductor with a band gap reported at 3.6 eV and higher at 300K. [14, 15, 65-68] The space charge layer control of nanostructures, including nanocrystalline SnO$_2$, makes them particularly interesting since conduction can change

drastically with expansion and contraction of the layer in the presence of different gases. [5, 8] The energy required for electrons or other charged species from adsorbed gas molecules to conduct through the material can be greatly impacted by the magnitude of the band gap and whether or not any energy levels exist within the forbidden energy gap. This chapter will focus on changes in the direct optical band gap of nanocrystalline SnO_2 doped with trivalent indium substitution that deviate from what is largely reported in the literature at the nanoscale.

Ultraviolet-Visible (UV-Vis) measurements were carried out on a Cary 1 UV-Vis spectrophotometer from Varian Incorporated. Doped SnO_2 nanocrystalline powders were compressed and scanned in the range of 200 to 800 nm using a Labsphere integrating sphere, Figure 32. The inside of the integrating sphere is coated with Spectralon (Polytetraflouroethylene, PTFE) and can perform both transmittance and reflectance measurements. Problems with scattering, light distortion, and refraction can become problems when using thick samples or powders. The integrating sphere performs a diffuse transmittance measurement which alleviates many of these problems.

Figure 32: *Labsphere Integrating Sphere*

For crystalline SnO_2, optical transitions have been shown to be direct. [69] The variation in the absorption coefficient as a function of photon energy for allowed direct transitions is given by:
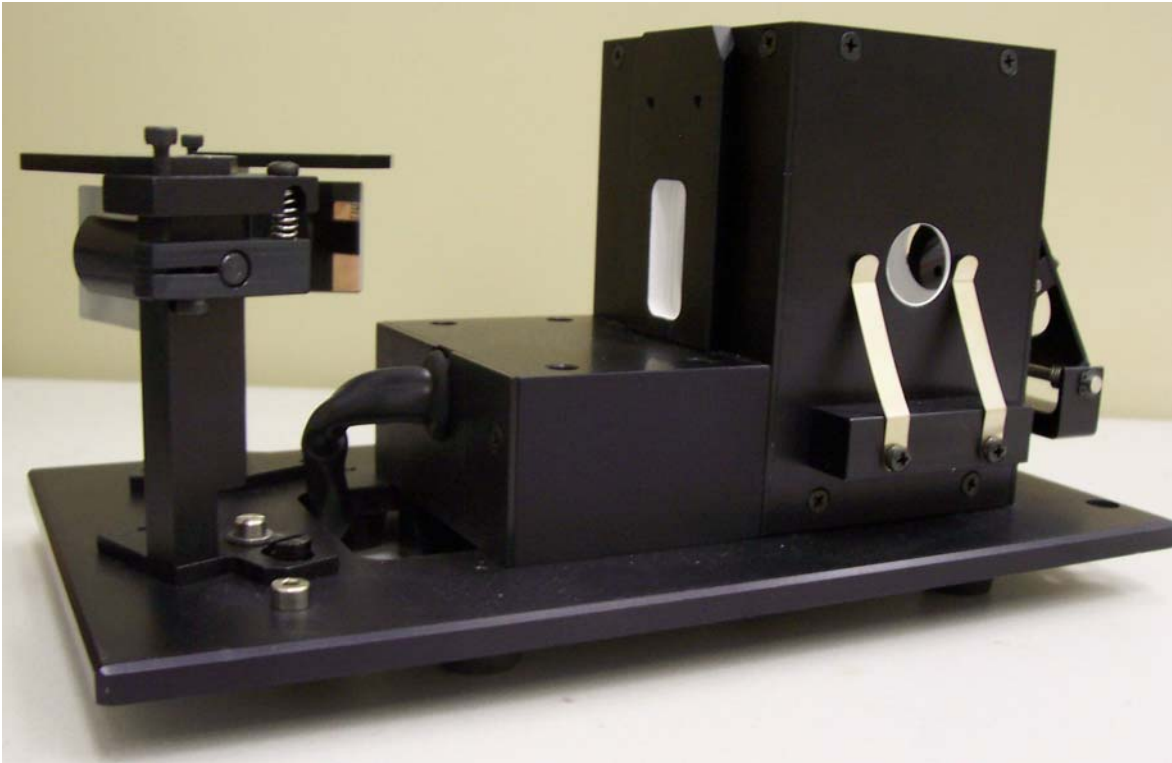
$$\alpha = A(hv - E_g)^{1/2}$$ ....(6.1)

In Equation (6.1), α is the absorption coefficient, A is a constant, h is Planck's constant, v is the frequency, and E_g is the band gap energy. The absorption coefficient, α, is obtained from Beer's law

$$I = I_o \exp(-\alpha x)$$ ....(6.2)

In the above equation, x is the thickness of the measured sample. A plot of α^2 versus photon energy was used to obtain the value of the direct band gap by extrapolating the linear portion of the curves to zero absorption.

Direct band gap values were determined for undoped nanocrystalline SnO_2 samples calcined at 500°C, 600°C, 800°C, and 1000°C in air. Figure 33 shows the determination of these values. The lowest band gap value is obtained for the sample calcined at 500°C with a value of 3.22eV. The values increase with calcination at 600°C and 800°C, with values of 3.75eV and 3.88eV respectively. At a calcination temperature of 1000°C, the band gap value decreases to 3.68eV. With the exception of the 500°C sample, the other 3 samples are within published values of the band gap for SnO_2. [14, 15, 65-68] The lower band gap value at a calcination temperature of 500°C is likely due to band bending effects. This would be caused by both the very small crystallite and grain sizes of the material as well as surface species (such as hydroxyl groups) not fully driven off at this calcination temperature. The value of 3.68eV reported for the highest calcination temperature is close to the widely published value of 3.6eV. This is possibly due to the

larger crystallite and grain sizes of this material that could possibly negate space charge effects as the major characteristic of the material.

$E_g=3.22eV$

$E_g=3.75eV$
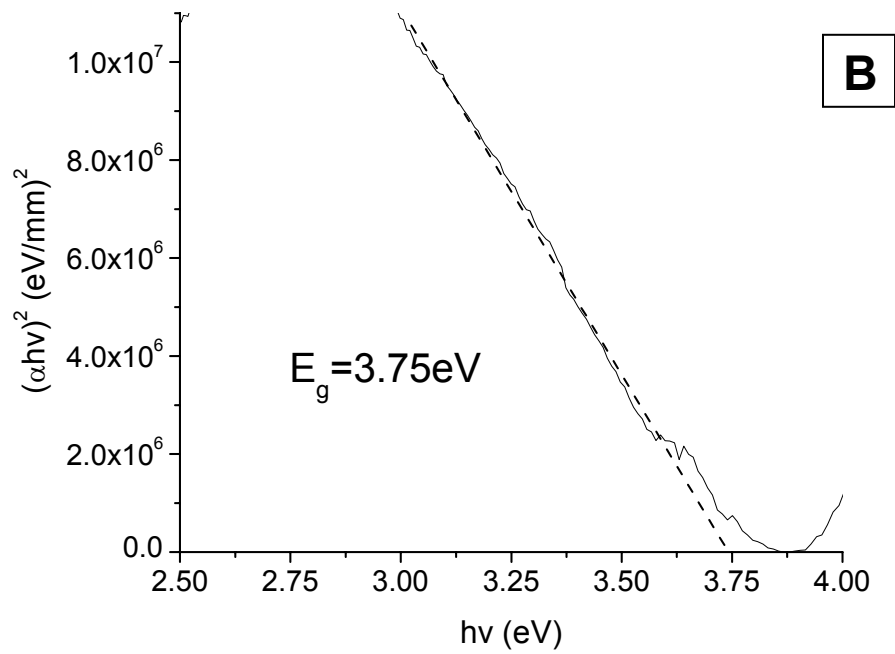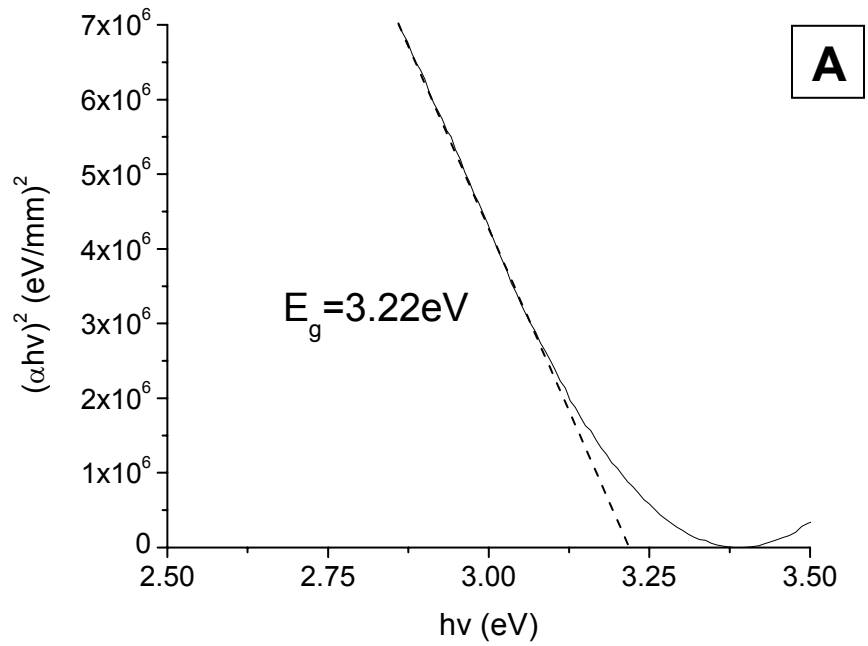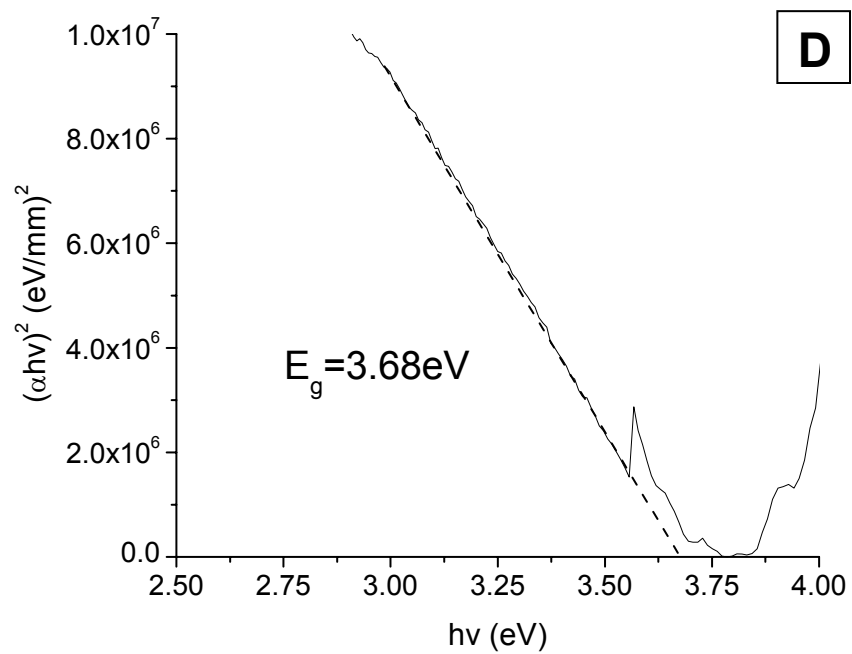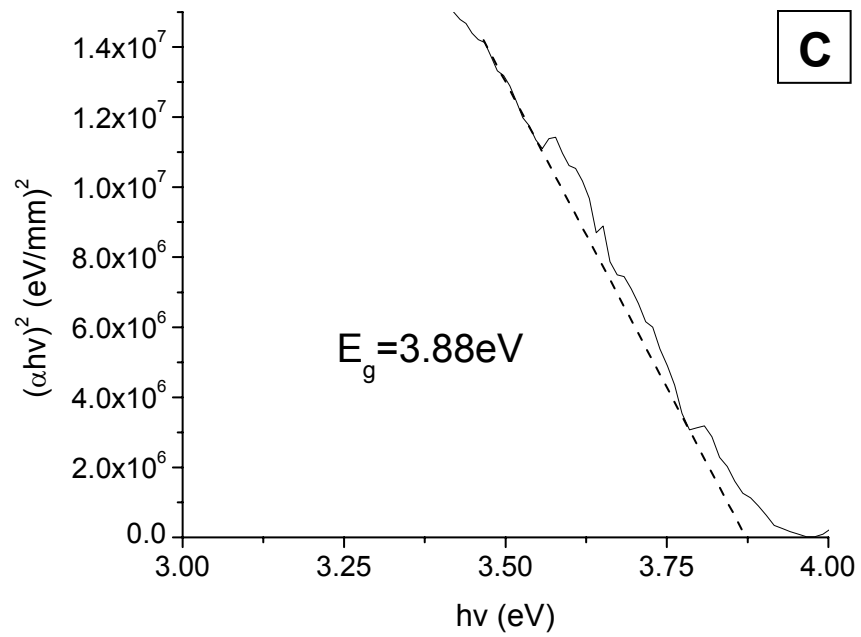
Figure 33: *Band gap determinations for A) 500°C, B) 600°C, C) 800°C, and D) 1000°C calcination temperatures of SnO$_2$*

The overall values obtained for all dopings and calcination temperatures are lower than the reported values for SnO$_2$, usually reported around 3.6 eV. Plots to obtain band gap values for 1% In doped samples are shown in Figure 34a. The highest band gap value was obtained for the sample calcined at 500° C at 3.1 eV. The band gap values decreased until a calcination temperature of 1000° C, where it slightly increased from the 800° C sample, 2.52 eV to 2.65 eV. For the 3% doped samples, Figure 34b, the same trend is followed as that of the 1% doped samples. The highest value for the 3% samples is for the one calcined at 500° C with a value of 3.05eV. The values again decrease until a calcination temperature of 1000° C, where the value slightly increases to 2.5 eV. For the 6.5% doped samples, a similar trend is noted, with a decrease in the band gap values with increasing calcination temperature until 1000° C, where the value increases, Figure 34c. Unlike the 1% and 3% doped samples, the highest value of the band gap is obtained at a calcination temperature of 1000° C at 3.43 eV. For the 9% doped samples, the trend is different from the other dopings, Figure 34d. Between 500° C and 600° C, the band gap decreases (from 3.14 to 2.62 eV) but then increases at 800° C to 3.16 eV. At 1000° C the band gap decreases.

B

C

1

$(\alpha h\nu)^2$

E_g= 3.1eV

2.5   2.8   3.0   3.3   3.5

hv

2

$(\alpha h\nu)^2$

E_g= 3.04eV

2.4   2.6   2.8   3.0   3.2   3.4

hv

3

$(\alpha h\nu)^2$

E_g= 2.75 eV

2.4   2.6   2.8   3.0

hv

4

$(\alpha h\nu)^2$

E_g = 3.43eV

2.5   2.8   3.0   3.3   3.5   3.8

hv
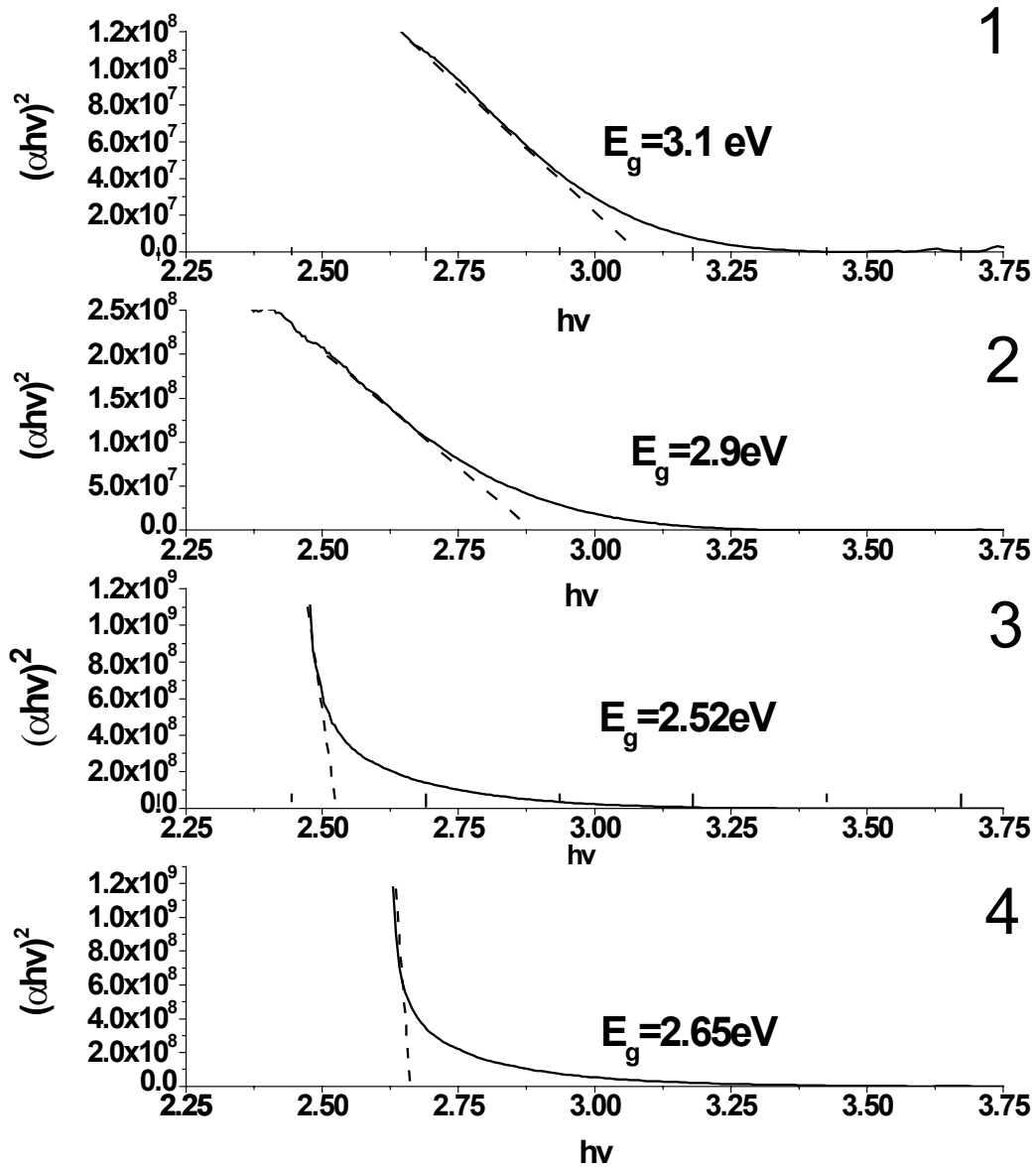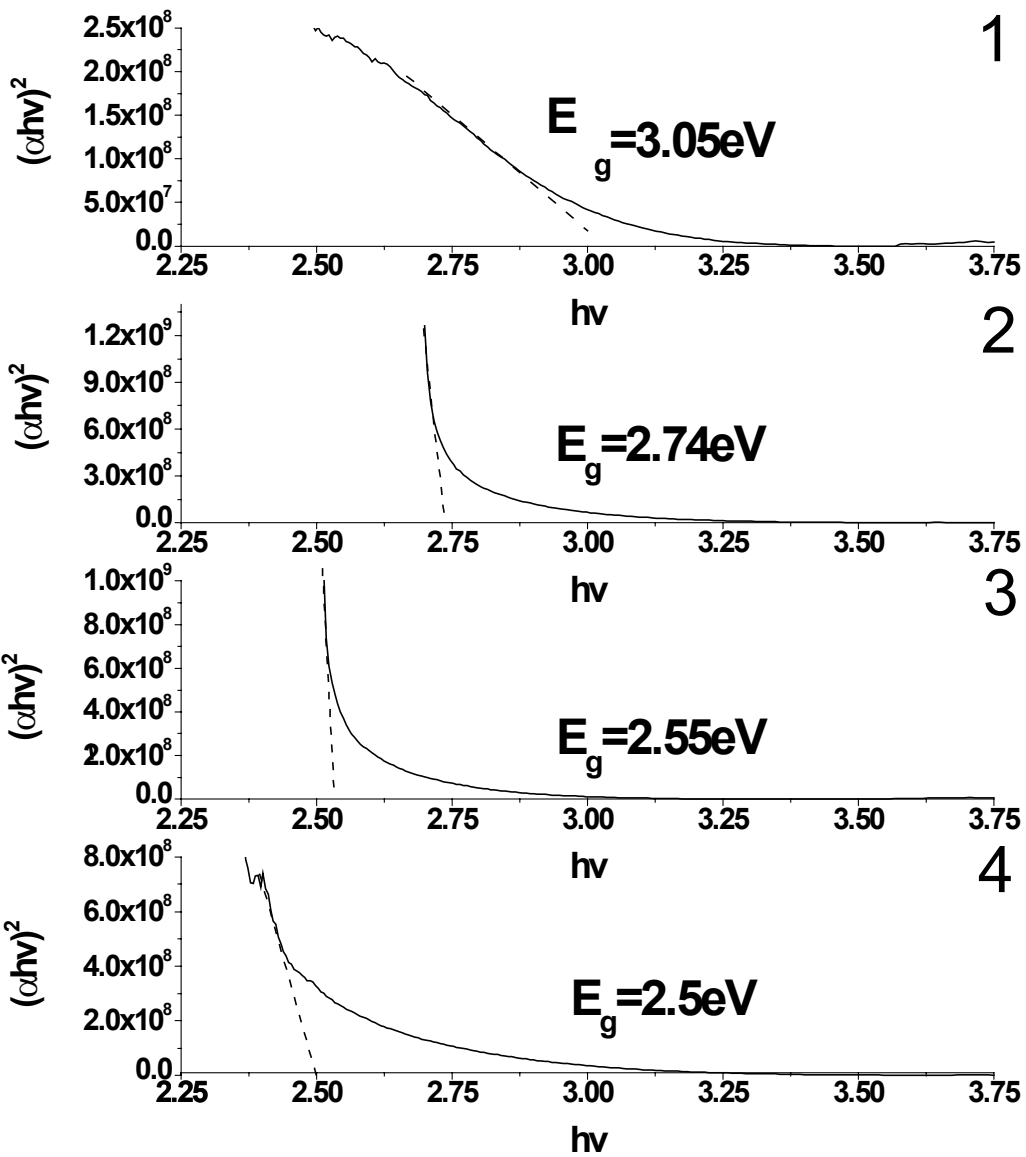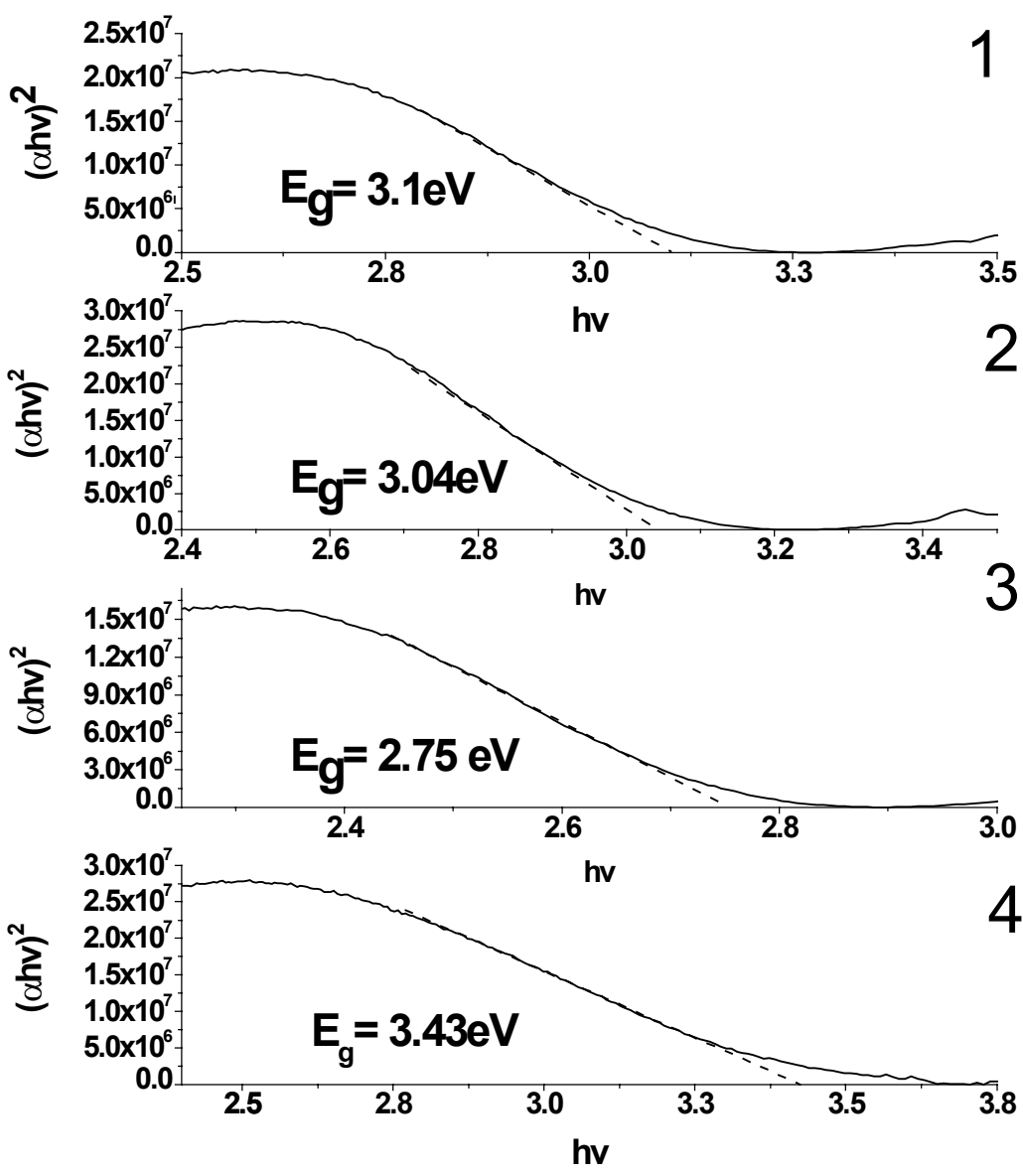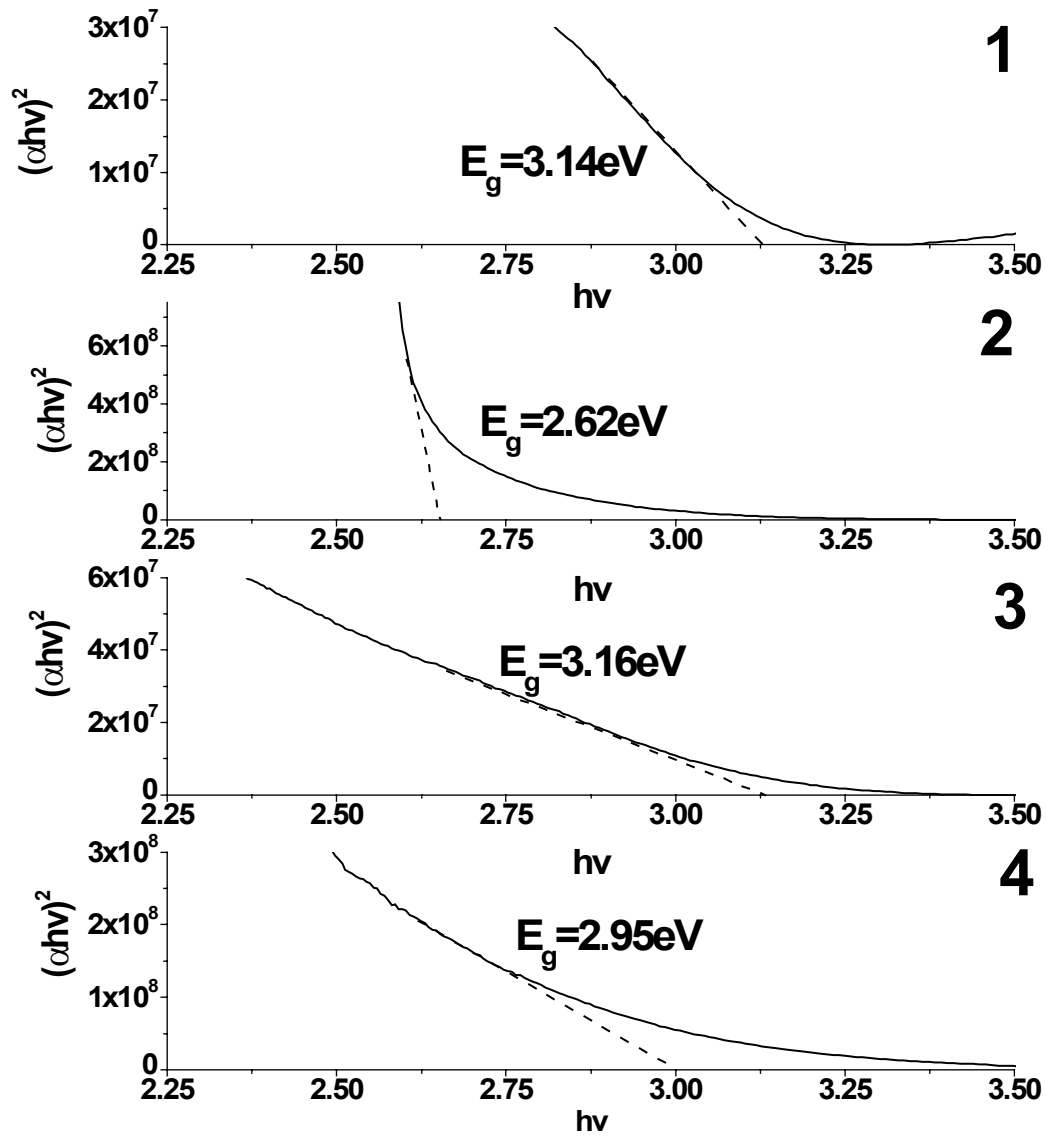
Figure 34: *Band gap extrapolations for A) 1% In-SnO$_2$, B) 3% In-SnO$_2$, C) 6.5% In-SnO$_2$, andD) 9% In-SnO$_2$ calcined at 1) 1000°C, 2) 800°C, 3) 600°C, and 4) 500°C*

In the case of In doped SnO_2 samples, the band gap drops with initial increase in doping amount (1% to 3%) and then increases at 6.5%, Figure 35. A similar trend was reported in cobalt doped SnO_2. [70] These decreases in the optical band gap for SnO_2 have been reported for SnO_2 doped with very small amounts of cobalt. For the Co doped SnO_2, a decrease was shown in the band gap at 1% followed by a steady increase in the band gap value with increasing doping amount.
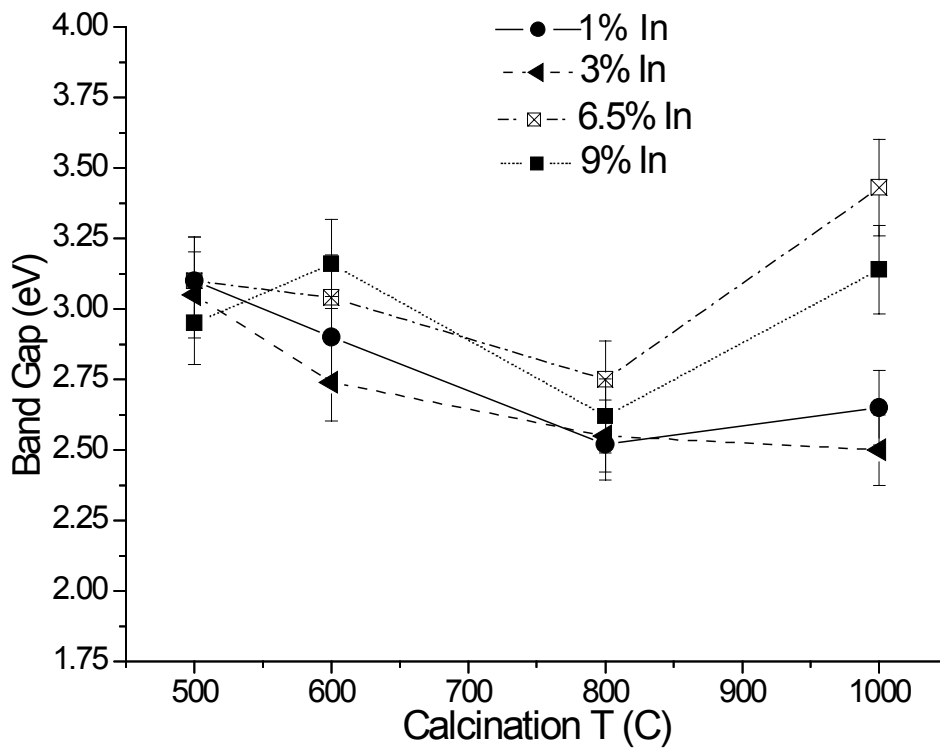
Figure 35: *Changes in the band gap with Calcination Temperature*

Full doping of SnO$_2$ with Indium will lead to substitution of In^{3+} onto a Sn^{4+} site and the creation of oxygen vacancies to retain charge neutrality within the cassiterite structure. In *Kroger-Vink* notation, charge modification upon doping occurs as

$$O_0^x \rightarrow \frac{1}{2}O_{2(g)} + V_O^{00} + 2e^- \quad \dots\dots\dots\dots\dots\dots\dots\dots\dots\dots\dots\dots\dots\dots(6.3)$$

$$2In^{3+} + 2Sn_{Sn}^x + O_O^x \rightarrow 2In_{Sn} + V_O^{00} + Sn_{Surface} \dots\dots\dots\dots\dots\dots\dots\dots\dots\dots(6.4)$$
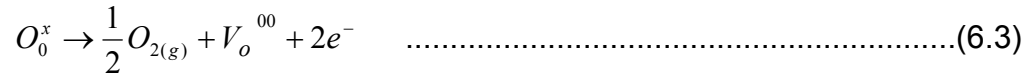
For 1% and 3% dopings, if complete doping were to occur, a large amount of oxygen vacancies would be created in the crystal lattice. The thermodynamic solution limit for Indium in the SnO$_2$ system has been reported to occur around 3%. [35] This lowering of the optical band gap gives an indication of the stoichiometric deviation (as well as possible degeneracy) of the doped SnO$_2$ material. It also indicates the increase in oxygen vacancies within the lattice. It has been previously shown that at low temperatures (as low as room temperature), a non-equilibrium amount of oxygen vacancies are maintained. [71] At room temperature, oxygen vacancy concentrations of 10^{23}/m^3 have been observed for these nanocrystalline In-SnO$_2$ samples, Table 3, section 5.3.

Direct band gap values for nanocrystalline Ce, In-SnO$_2$ samples were analyzed as well. Like the indium doped SnO$_2$ samples, these also showed a decrease in their band gap, Figure 36. Because these samples were doped at 6.5% In and 3.5% Ce, it shared a common trend with the 6.5% In-SnO$_2$ samples.   These samples saw a decrease in the optical band gap from 2.95 eV down to 2.82 eV with increasing calcination temperature

until a calcination temperature of 1000°C, where the highest band gap is achieved at 3.1eV.
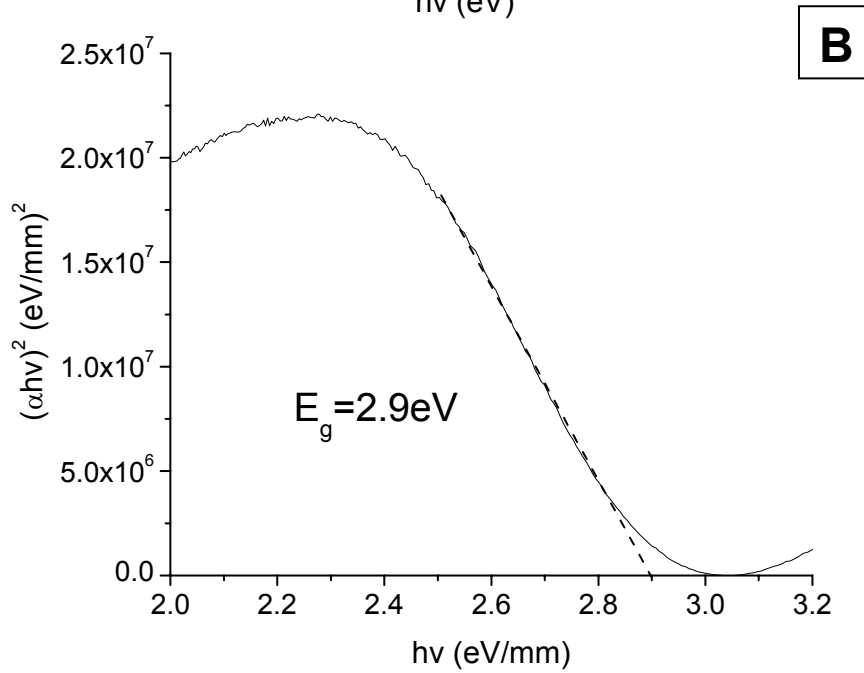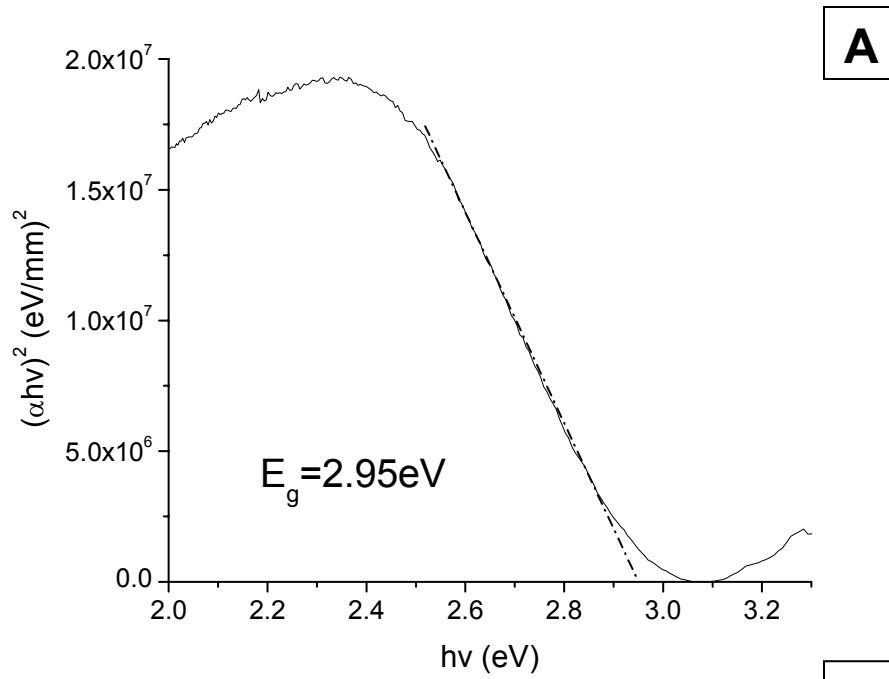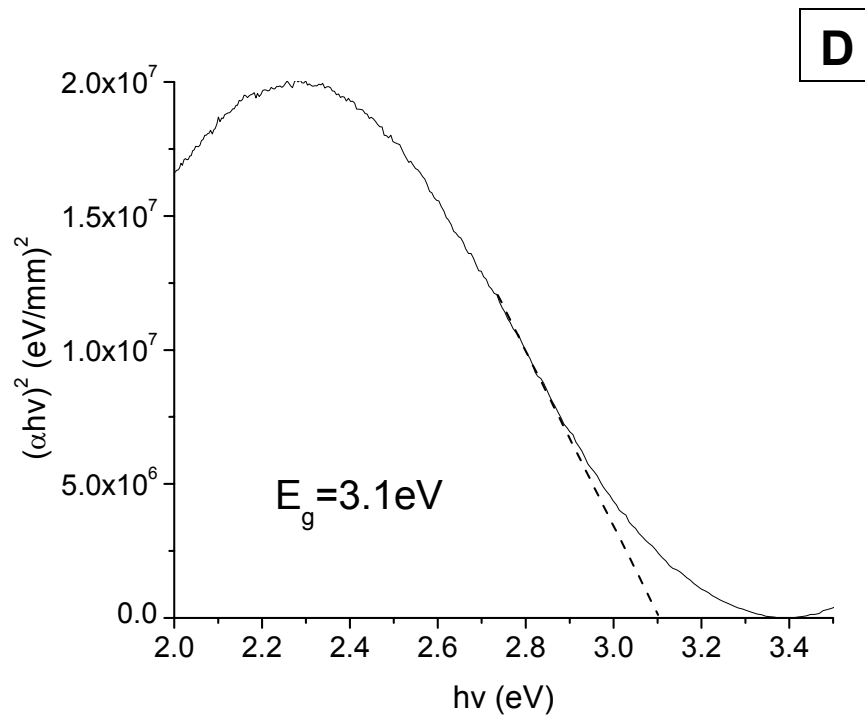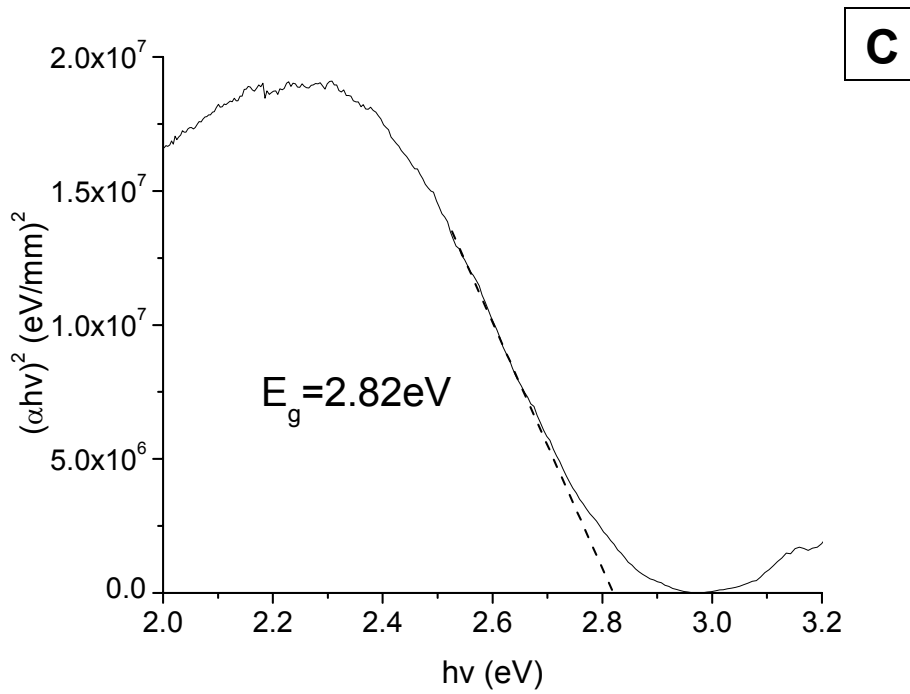
Figure 36: *Band gap values from absorption data of A) 500°C Ce, In-SnO$_2$, B) 600°C Ce, In-SnO$_2$, C) 800°C Ce, In-SnO$_2$, and D) 1000°C Ce, In-SnO$_2$*

Though the trend for changes in the band gap between 6.5% In-SnO_2 and 3.5% Ce, 6.5% In- SnO_2 are similar, there is a noticeable drop in the overall optical band gap values of the latter. This is likely due to the great amount of disorder caused in the early stages of forming the nanoparticles upon attempting doping of the system at 10% total between Ce and In. Also changes to the surface of the grains with migration of the Ce atoms to the surface would also have changes to the amount and degree of band bending in the structure. Changes to the surface charge due to the multi-valency of the Ce atom may be responsible for this lowering of the band gap.

In order for band bending of the conduction band to occur towards the valence band in a semiconductor, a negative space charge must develop. This usually occurs by an excess of electrons or negative charge. In order to develop this negative charge with excess oxygen vacancies, surface species must adsorb onto the surface of the material and donate electrons. These donated electrons can then associate themselves with positively charged oxygen vacancies. In fact, it has been previously observed by the author's group that the major free carriers in sol-gel derived nanocrystalline In-SnO_2 are in fact monoionized oxygen vacancies. [71] Due to the fact that these nanoparticles are small and comparable in size to their Debye length, the space charge region will completely occupy the material and control the band structure. [10] At the nanoscale, this surface induced band bending then characterizes the band structure of the entire material.

Another explanation for the ability of a material to decrease its band gap energy is that the density of surface states induced by chemisorbed oxygen species decreases with decreasing particle size, which would lead to a lesser degree of Fermi pinning. [72] This would allow the surface barrier to undergo larger changes and controls the ability of charged species to move through the material. This decrease in density of surface states is directly caused by the curvature of the nanoparticles. It has been shown using Scanning Tunnelling Spectroscopy, for nanoparticles (10 and 30 nm) that a surface band gap of around 2.5 eV exists. [72] It is likely that for the In-SnO_2 nanoparticles (sizes ranging from 3 to 23 nm), a combination of the decrease in the density of surface states and the large amount of oxygen vacancies retained in the material explain the departure in the band gap values from what has been reported.

These changes in the band gap also partially explain the enhanced ability for nanocrystalline In-SnO_2 to be used in gas sensor applications at room temperature. Since the potential barrier required for charge to move between grains is now reduced with a lower band gap energy, conduction at room temperature is more easily achieved. The author's group [73] has recently shown that In doped SnO_2 coated MEMS device used at room temperature has a response time of 20 seconds for 900 ppm of hydrogen gas.

The question arises as to why the 6.5% and 9% In-SnO_2 samples exhibited slightly different behavior than the 1% and 3% doped samples. First, both the 6.5% and 9% are above the thermodynamically predicted Indium doping amount in SnO_2 of 3%. [30] For

the 6.5% In-SnO$_2$ nanocrystalline samples, it has been shown that using sol gel techniques and at low calcination temperatures, doping amounts above what is thermodynamically predicted can occur. [74] From previous FTIR studies, it has been demonstrated that, when exposed to H$_2$ gas, the 6.5% samples do not respond to hydrogen gas in the same manner that the 3% doped samples respond. In the case of 3% In-SnO$_2$, surface species such as CO$_2$ and hydroxyl groups changed with regard to the magnitude of their peaks after exposure to H$_2$. Contrary, the 6.5% In-SnO$_2$ sample after exposure to hydrogen showed little impact on these surface species. This indicates a difference in the nature of the same adsorbed surface species on the surface of these two different dopings of SnO$_2$. Because of this, surface effects such as band bending and surface density of states would be different, and it would be expected that these two materials would have different electronic behavior at the nanoscale. This helps to explain the enhanced gas sensing behavior of 6.5% In doped SnO$_2$ at low temperatures over other dopings in the same material systems. The 6.5% In doped sample likely has the best trade off between surface species retained after synthesis (in order to participate in hydrogen sensing) and band bending effects (which lowers the activation energy required for charge movement at room temperature).

As gas sensor applications move towards lower working temperatures, knowledge of what can be utilized at the nano-scale becomes very important. Ability to understand the effect of doping and its impact on the surface of nanomaterials is paramount as the surface dominates many features at the nanoscale. For room temperature applications, reduction of the activation energy required for the gas sensing reaction is just as

important as the surface reaction. By changing the band gap values, the energy barrier required for species to move through the space charge region can be modified making room temperature applications more of a reality. This can have even wider implications as Material Science moves towards better understanding at the nanoscale, fine tuning materials better to specific applications.

For nanocrystalline chemically synthesized In doped SnO_2, it has been shown that the optical band gap values for direct transitions are much lower than the expected values reported. The lowest value of the band gap was achieved in the 3% doped sample calcined at 800° C, while the highest value of the band gap was achieved at in the 6.5% doped sample calcined at 1000° C. It was also shown that achieving the lowest band gap does not necessarily ensure enhanced room temperature gas sensing but is critical in the tuning of a nanomaterial to lower working temperatures. Because of this reduction in the band gap, room temperature gas sensing is possible with a reduction in the potential barrier required for charge movement in nanocrystalline (3% and 6.5% doped) In-SnO_2 calcined at 500° C, when exposed to a reducing gas.

CHAPTER SEVEN: CONCLUSIONS

Nanocrystalline indium doped SnO_2 has proven itself as an excellent material for use in room temperature gas sensor applications. At room temperature, without help from a catalyst such as platinum, it has shown the ability to detect hydrogen gas. The ability for nanocrystalline $In-SnO_2$ to achieve this detection ability is due to phenomena that occur at the nanoscale. These include changes in the electronic structure from band bending and the space charge layer. It also includes other nano-scale effects such as high surface to volume ratio, retained oxygen vacancy concentrations at low temperatures, and changes in the surface density of states.

Doping with Indium (3+) into the SnO_2 system has shown itself as an excellent way in which to change different properties of the material system. Changes in the growth of the nanocrystals were observed depending on amount of dopant incorporated into the material. The maximum amount of indium that could be doped into nanocrystalline SnO_2 was also shown to be higher than what has been reported in the literature. It appears that dopings over the thermodynamically predicted amount are possible when the sol-gel method is used to obtain nanocrystalline SnO_2.

Diffuse Reflectance mode of the FTIR was shown to be very useful in the prescreening of these potential nanomaterials for gas sensor applications. The ability to screen several permutations of a material system is useful in the fine tuning of potential

materials to target gases. For SnO_2, in the presence of hydrogen gas, an upwards shift in the absorbance spectra was noted if the material was able to detect the hydrogen gas. This upwards shift in the absorbance was due to an increase in the amount of free carriers in the space charge layer of the nanomaterial upon chemical detection of the gas.

The FTIR proved to be useful beyond just qualitative prescreening of potential gas sensor materials. Using Beer's law and Drude-Zener theory, calculations of the free carrier concentration and conductivity of the materials could also be determined. From this information, it was found that oxygen vacancies were the major charge carrier for nanocrystalline In-SnO_2. It was also found that at room temperature; these oxygen vacancy concentrations remained relatively constant, explaining some of the enhanced ability for this material to detect hydrogen gas at room temperature.

Light was shed on the role of doping at the nanoscale and its impact on the gas sensor behavior of nanocrystalline SnO_2 with use of the FTIR. It was shown that depending on the amount of indium doping, there was a difference in the surface species which participated in the reaction which identifies hydrogen gas. The ability to monitor changes in surface species upon introduction of gases (such as CO_2) not detected by the sensor material was also shown. These are important when it comes to the fine tuning of sensor materials to specific gases as well as to specific environments. This information also helps in engineering a sensor material to be selective to a target gas over other gases.

The role of recovery of nanocrystalline In-SnO$_2$ was also investigated with the incorporation of multivalent ceria. Because of ceria's multivalent abilities, it has the possibility to hold and release oxygen species. It was found through XRD and FTIR studies that a separate phase of ceria is required for this recovery to take full affect. Doping of Ce into In-SnO$_2$ was not effective in either detection of hydrogen gas or for the recovery of the material. It was shown from FTIR and XRD that when a separate phase of ceria is present with the nanocrystalline In-SnO$_2$ that detection of hydrogen gas is possible and that the amount of recovery was greatly increased and the time shortened for the sensor material.

Band gap changes for nanocrystalline In-SnO$_2$ were also investigated. This was done by finding the optical band gap from the absorption edge determined from UV-vis measurements. These results showed a lowering of the direct band gap in nanocrystalline In-SnO$_2$, below the published values reported around 3.6 eV. These lower values help to explain the lower room temperature gas sensor behavior of the nanomaterial. Because the controlling mechanism for conduction of nanocrystalline In-SnO$_2$ is contraction and expansion of the space charge layer, the width, and therefore potential barrier height, for charge carriers to pass through, is affected by the magnitude of the band gap for the material. This essentially changes the activation energy required for charge carriers to move through the material.

To achieve room temperature gas detection of hydrogen for nano-oxides, the following are needed:

1. Non-equilibrium amount of oxygen vacancies retained at room temperature,

2. Crystallite sizes comparable to the Debye length of the material,

3. Lowering of the band gap, in order to lower the potential barrier height for room temperature conduction,

4. Surface species to identify the target gas.

Though this is not an exhaustive list, these are many of the major contributing factors to the enhanced room temperature gas sensor abilities of nanocrystalline In-SnO$_2$. This study has been systematic in approaching the gas sensor behavior of In-SnO$_2$ by considering all of the material parameters that would actually have an impact on its gas detection abilities. In this way, the best material from this material system, in this study 6.5% In-SnO$_2$ calcined at 500°C, was identified for the application chosen. The broader impact of this research is that these principles can viably be applied to other nano-oxide systems in order to engineer the nanomaterials to specific applications.

Future studies that would be fruitful in further understanding the role of nano-oxides for low temperature applications are needed. These include incorporation of the recovery aspects achieved from incorporation of ceria onto the surface of a nano-oxide being used to detect a reducing gas. How to correctly synthesize and fabricate the nanocomposite would be beneficial. Further studies into the differences in what appear

to be similar surface species on the surface of nanocrystalline In-SnO$_2$ would also be beneficial to gas sensor research, as well as several other applications. Growth simulations and reconstructions of the different surface species under different synthesis conditions would give rise to even more specific engineering of nanomaterials then what is currently known to the world of research within nanotechnology.

REFERENCES

1. Associated Press, CNN, July 25, 1999

2. Mark Carreau, The Houston Chronicle, April 5, 2002

3. S. Shukla and S. Seal; *Encyclopedia of Nanoscience and Nanotechnology*, Volume X (2004), pp. 1-16

4. S. Seal and S. Shukla; Journal of Materials (2002), pp. 35-38

5. A. Puzder, A.J. Wiliiamson, F.A. Reboredo, and G. Galli; Physical Review B, 91 (2003) 15

6. S. Shukla, S. Seal, L. Ludwig, and C. Parish, Sensors and Actuators B, 97, 256 (2004)

7. 2. S. Shukla, S. Patil, S. C. Kuiry, Z. Rahman, T. Du, L. Ludwig, C. Parish and S. Seal, Sensors and Actuators B, 96, 343 (2003)

8. T.G Maffeis G. Owen, M. Penny, T. Starke, S. Clark, H. Ferkel, and S, Wilks, Surface Science, 520, 29 (2002)

9. N. Dharmaraj et al, Spectrophimica Acta Part A 2005

10. N. Yamazoe; *Sensors and Actuators B*, 5 (1991), pp. 7-19

11. A. E. Rakhshani, Y. Makdisi, and H. A. Ramazaniyan; J. Appl. Phys, 83 (1998) 1049

12. Z. Nabi, A. Kellou, S. Mecabih, A. Khalfi, N. Benosman; Materials Science and Engineering B98 (2003) 104/115

13. G. Sanon, R. Rup, A. Mansingh; Phys. Rev. B, 44 (1991) 11

14. H. Kim and A. Pique; Appl. Phys. Lett, 84 (2004) 2

15. J. H. Chung, Y. S. Choe, and D.S. Kim; Thin Solid Films, 349 (1999) 126-129

16. F. Gu, S. F. Wang, M. K. Lu, G. J. Zhou, D. Xu, D. R. Yuan; Journal of Physical Chemistry B, 108 (2004) 8119-8123

17. H. Yang, X. Song, X. Zhang, W. Ao, G. Qiu; Materials Letters, 57 (2003) 3124-3127

18. J. Fayat, M.S. Castro; Journal of the European Ceramic Society, 23 (2003) 1585-1591

19. A. R. Phani, S. Manorama, V.J. Rao; Materials Chemistry and Physics, 58 (1999) 101-108

20. D. D. Vuong, G. Sakai, K. Shimanoe, and N. Yamazoe; Sensors and Actuators B, 103 (2004) 386-391

21. M. Batzill and U. Diebold; Progress in Surface Science, 79 (2005) 47-154

22. M. A. Mäki-Jaskari and T. T. Rantala, Physical Review B 65 (2002) 245428

23. M. Batzill, A. M. Chaka, and U. Diebold, Europhys.Letters 65 (2004) 61

24. W. Bergermayer and I. Tanaka, Applied Physics Letters, 84 (2004) 909

25. Richerson; *Modern Ceramic Engineering*, 2nd edition

26. M. Balkanski and R.F. Wallis: Semiconductor Physics and Applications; Oxford University Press Inc., 2000

27. K.S. Yoo et al, Sensors and Actuators B 24-25 (1995) 474-477

28. S. O. Kucheyev, T. F. Baumann, P. A. Sterne, Y. M. Wang, T. van Buuren, A. V. Hamza, L. J. Terminello, and T. M. Willey; Physical Review B, 72, 035404 (2005)

29. W. Liu, X. Cao, Y. Zhu, and L. Cao; *Sensors and Actuators B,* 66 (2000), 219-221

30. A. R. West, "Basic Solid State Chemistry", John Wiley and Sons, LTD; West Sussex, England, 1999

31. Y.J. Chen, X.Y. Xue, Y.G. Wang, and T.H. Wang; Applied Physics Letters, 87, 233503 (2005)

32. C. Richard Brundle, Charles A. Evans Jr., Shaun Wilson: "Encyclopedia of Materials Characterization"; Manning Publications Co. 1992

33. F. R. Sensato, R. Custodio, M. Calatayud, A. Beltran, J. Andres, J. Sambrano, and E. Longo, Surface Science*,* 511, 408 (2002)

34. N. L.V. Carreño, H.V. Fajardo, A.P. Maciel, A. Valentini, F.M. Pontes, L.F.D. Probst, E.R. Leite, and E. Longo; Journal of Molecular Catalysis A: Chemical 207 (2004) 89–94

35. J. Werner, G. Behr, W. Bieger, G. Krabbes, Journal of Crystal Growth 165 (1996) 258-267)

36. N. J. Harrick, Physical Review, 125(1962) 1165-1170

37. M.I. Baraton and L. Merhari; Journal of the European Ceramic Society, 24 (2004) 1399

38. N. J. Harrick; Physical Review, 103 (1956) 1173

39. Spitzer, Collin, and Fan*;* Physical Review*,* 98, (1955) 1536

40. G. Martinelli and M. Carotta; Sensors and Actuators B, 23**,** 157 (1995)

41. G. Ghiotti, A. Chiorino, and F. Prinetto, Sensors and Actuators B, 24-25, 564 (1995)

42. H. Ogawa. M. Nishikawa and A. Abe, Journal of Applied Physics, 53, 4448 (1982)

43. R. Gerhardt and A. Nowick; Journal of the American Ceramic Society, 69, 641 (1986)

44. J. R. Schrieffer; *Physical Review*, 97 (1955) 641-646

45. K. Nakano, T. Masui, G. Adachi; *Journal of Alloys and Compounds*, 344 (2002), pp. 342-346

46. M. S. Dutraive, R. lalauze, and C. Pijolat; Sensors and Actuators B, 26-27 (1995) 38-44

47. M. N. Rahaman, "Ceramic Processing and Sintering", Marcel Dekker, Inc; New York, 1995

48. C.V. Santinelli, S.H. Pulcinelli, and A.F. Craievich; Physical Review B, 51 (1995) 8801-8809

49. K. N. Yu, Y. Xiong, Y. Ciu, C. Xiong, Physical Review B 55 4 (1997) 2666–2671

50. C. H. Shek, J.K.L. Lai, and G.M. Lin: NanoStructured Materials; Vol 11, No7 (1999) 887-993

51. E. R. Leite, J.A. Cerii, E. Longo, J.A. Varela, C.A. Paskocima: Journ. European Ceramic Society; 21 (2001) 669-775

52. J. K. L. Lai, C.H. Shek , G.M. Lin, Scripta Materialia 49 (2003) 441–446

53. M. I. Baraton and L. Merhari; Scripta Materialia, 44 (2001) 1643-1648

54. O. Wurzinger and G. Reinhardt; Sensors and Actuators B; 103 (2004) 104-110

55. D. Amalric-Popecu and F. Bozon-Verduraz: Catalysis Letters 64 (2000) 125-128

56. C. Kilic and A. Zunger; Physical Review Letters, 88 (2002) 9

57. A. Maciel, P. Lisboa-Filho, E. Leite, C. Paiva-Santos, W. Schreiner, Y. Maniette, and E. Longo; Journal of the European Ceramic Society; 23 (2003) 707

58. H. Yang, S. Han, L. Wang, I. Kim, and Y. Son: Material Chemistry Physics; 56 (1998) 153

59. H. Ahn, H. Choi, K. Park, S. Kim, and Y. Sung: Journal of Physical Chemistry B; 108 (2004) 9815-9820

60. G. Xu, Y. Zhang, X. Sun, C. Xu, C. Yan: Journal of Physical Chemistry B; 109 (2005) 3269-3278

61. P. Singh, A.K. Chawla, D. Kaur, and R. Chandra; Materials Letters xx (2006) xxx-xxx

62. Y. Ma, F. Zhou, L. Lu, and Z. Zhang: Solid State Communications 130 (2004) 313–316

63. S. Shanthi, C. Subramanian, and P. Ramasamy; Crystal Res. Technology, 34 (1999) 8, 1037-1046

64. D. Dragoman and M. Dragoman; "Optical Characterization of Solids", Springer, Verlag Berlin Heidelberg New York, 2002

65. Z. Nabi, A. Kellou, S. Mecabih, A. Khalfi, and N. Benosman: Materials Science and Engineering; B98 (2003) 104/115

66.   S. Shanthi, C. Subramanian, and P. Ramasamy; Crystal Res. Technology, 34 (1999) 8 1037–1046

67.   A. E.Taverner, C. Rayden, S. Warren, A. Gulino, P.A. Cox, and R.G. Egdell; Physical Review B; 51 (1995) 11

68.   J. Kang, S. Tsunekawa, and A. Kasuya: Applied Surface Science; 174 (2001) 306-309

69.   J. Robertson, Journal of Physical Chemistry: Solid State Physics, Vol. 12 (1979)

70.   J. Hays, A. Punnoose, R. Baldner, M.H. Engelhard, J. Peloquin, and K.M. Reddy; Physical Review B 72, 075203 (2005)

71.   C. Drake, S. Deshpande, and S. Seal; Applied Physics Letters; 89 1 (2006)

72.   T.G.G Maffeis, G.T. Owen, C. Malagu, G. Martinelli, M.K. Kennedy, F.E. Kruis, and S.P. Wilks; Surface Science; 550 (2004) 21-25

73.   S. Deshpande, P.Zhang, N. Posey, J. Cho and S. Seal; Applied Physics Letters, In press

74.   C. Drake, A.Amalu, J.Bernard, and S.Seal: *Enhancing the low temperature hydrogen sensitivity of nanocrystalline SnO_2 as a function of trivalent dopants*, Journal of Applied Physics, Accepted for Publication